THESIS FOR THE DEGREE OF DOCTOR OF PHILOSOPHY

Beyond average crystal structures: understanding extended and local environments in proton-conducting Sc-substituted $BaTiO_3$ perovskites

Nico Torino

CHALMERS
UNIVERSITY OF TECHNOLOGY

Department of Chemistry and Chemical Engineering

CHALMERS UNIVERISTY OF TECHNOLOGY

Gothenburg, Sweden 2019

Beyond average crystal structures: understanding extended and local environments in proton-conducting Sc-substituted $BaTiO_3$ perovskites

Nico Torino

ISBN 978-91-7905-181-5

Doktorsavhandlingar vid Chalmers Tekniska Högskola
Ny serie 4648
ISSN 0346-718X

Department of Chemistry and Chemical Engineering
CHALMERS UNIVERSITY OF TECHNOLOGY
SE-412 96 Gothenburg
Sweden
Telephone +46 (0)31-772 1000

Cover: 2ϑ dependence of the scattered intensity for $BaSc_{0.2}Ti_{0.8}O_{2.9}$, BTS20, as recorded by the D2B neutron diffractometer at the Institut Laue-Langevin in Grenoble (France).

Printed by Chalmers Reproservice

Gothenburg, Sweden 2019

Dedicated to the memory of Prof. Sten G. Eriksson

Beyond average crystal structures: understanding extended and local environments in proton-conducting Sc-substituted $BaTiO_3$ perovskites

Nico Torino
Department of Chemistry and Chemical Engineering
CHALMERS UNIVERSITY OF TECHNOLOGY

Abstract

Proton conducting ceramics are very promising for applications concerned with energy sourcing with cleaner, safer, more abundant and cheaper alternatives to fossil fuels. These materials are still in development and advances in the field depend on a better understanding of the role of defects, their identification and location in the host framework, and the assessment of their short- and long-range dynamics and kinetics. With that aim, the work included in this thesis focussed on investigations of the effect of Sc substitution on the long- and short-range structure, oxygen vacancies and protons distribution, and their link to proton conductivity, in $BaTiO_3$ materials. The system $BaTi_{1-x}Sc_xO_{3-x/2}$ with x = ⅙, 20, 50 and 70 was studied with a combination of thermogravimetric, scattering, spectroscopic and computational methods.

Neutron powder diffraction (NPD) provided the first representations of hexagonal and cubic members of the solid solution $BaTiO_3$-Sc_2O_3. They revealed the different ordering of oxygen vacancies, protons and transition metal ions in the two structural types as a function of the Sc concentration and justified the large improvement in proton conductivity from hexagonal to cubic structures, due to the localised nature of protonic defects in the former. The combination of thermogravimetric and NPD methods applied simultaneously to study the dehydration of cubic members of the series suggested that vacancy-vacancy interactions are attenuated by higher Sc levels where the size difference between oxygen vacancy and protonic defect is larger. The Reverse Monte Carlo method revealed the local ordering of Ti in cubic types, a local symmetry-breaking effect that has repercussions on the physical properties of these materials, causing anomalously small volume changes upon hydration in low-Sc phases. Computer simulations, and spectroscopic methods employing radiation (IR, Raman) and neutrons (Inelastic Neutron Scattering) provided further insight into the structural features and offered a detailed characterisation of the proton sites and their dynamics, suggesting that higher Sc levels are associated to weaker hydrogen bonding and to configurations more favourable for proton transport.

The present work contributed further understanding of the factors influencing proton transport in highly defective perovskite-structured materials. It was found that high Sc concentrations in the cubic host lattice of $BaTiO_3$ yield highly stable phases where transport of protonic defects is favoured by a crystal site of high symmetry and multiplicity. Alongside the study of the peculiarities of the BTS system, recommendations for candidate systems identification and doping strategy were provided.

Keywords: *perovskite, $BaTiO_3$, proton conducting oxide, ordering, neutron scattering, thermogravimetry, Reverse Monte Carlo, Raman, IR*

Publications included in this thesis

I **The influence of cation ordering, oxygen vacancy distribution and proton siting on observed properties in ceramic electrolytes: the case of scandium substituted barium titanate**

Nico Torino, Paul F. Henry, Christopher S. Knee, Tor Svendsen Bjørheim, Seikh M. H. Rahman, Emma Suard, Carlotta Giacobbe and Sten G. Eriksson

Dalton Transactions **46** 8387-8398 (2017)

Syntheses, data collection for XRD, TG. NPD experiments were performed at the ILL (France), together with Paul F. Henry and Seikh M. H. Rahman. The author and Paul F. Henry did the data analysis. Tor Svendsen Bjørheim was responsible for DFT calculations. The author wrote the first draft and was the main author together with Paul F. Henry.

II **Insight into the dehydration behaviour of scandium-substituted barium titanate perovskites via simultaneous in situ neutron powder thermodiffractometry and thermogravimetric analysis**

Nico Torino, Paul F. Henry, Christopher S. Knee, Samantha K. Callear, Ronald I. Smith, Seikh M. H. Rahman and Sten G. Eriksson

Solid State Ionics **324** 233-240 (2018)

Syntheses, data collection for XRD, *ex situ* TG. *In situ* experiments were performed at ISIS (UK), together with Paul F. Henry. The author did the data analysis, wrote the first draft and was the main author.

III **Reverse Monte Carlo modelling reveals the local ordering in hexagonal and cubic scandium-substituted $BaTiO_3$ proton-conducting perovskites**

Nico Torino, Wojciech A. Sławiński, Christopher S. Knee, Paul F. Henry and Sten G. Eriksson

In manuscript

Syntheses, XRD data collection, Rietveld analyses, TG. Total scattering experiments were performed at ISIS (UK), together with Paul F. Henry. Wojciech Sławiński contributed the Reverse Monte Carlo (RMC) analysis from which pair distribution functions were obtained. The author wrote the first draft and was the main author.

IV **Proton sites in hexagonal and cubic Sc-doped $BaTiO_3$ proton-conducting oxides**

Adrien Perrichon, Nico Torino, Erik Jedvik Granhed, Yuan-Chih Lin, Stewart F. Parker, Mónica Jiménez-Ruiz, Maths Karlsson and Paul F. Henry

In manuscript

Syntheses, XRD and IR data collection, Rietveld analyses, TG. Neutron spectroscopy experiments were performed at ISIS (UK) together with Adrien Perrichon, responsible for the analysis of spectroscopic data together with Yuan-Chih Lin, who collected Raman spectra. Erik Jedvik Granhed contributed DFT calculations. The author contributed to the first draft.

Contents

List of figures

List of tables

Glossary

Abbreviations

ADP	Atomic Displacement Parameter
CN	Coordination Number
CPS	Counts Per Second
DFT	Density Functional Theory
EDX	Energy Dispersive X-ray Spectroscopy
EMF	Electromotive Force
fcc	face centred cubic
INS	Inelastic Neutron Scattering
IR	Infrared
M	Metal dopant
MIEC	Mixed Ionic Electronic Conductor
NMR	Nuclear Magnetic Resonance
NPD	Neutron Powder Diffraction
PCFC	Proton Conducting Fuel Cell / Protonic Ceramic Fuel Cell
PDF	Pair Distribution Function
RMC	Reverse Monte Carlo
RT	Room Temperature
SEM	Scanning Electron Microscope
SOF	Site Occupancy Factor
SOFC	Solid Oxide Fuel Cell
TG	Thermogravimetry
ToF	Time of Flight
XPS	X-ray Photoelectron Spectroscopy
XRD	X-ray Diffraction

Symbols

δ(OH), ν(OH)	O–H bend, O–H stretch
BCY	Y-doped $BaCeO_3$ materials
BSFC	(Ba, Sr)(Co, Fe)$O_{3-\delta}$ materials
BTS	Sc-substituted $BaTiO_3$ materials
BZY	Y-doped $BaZrO_3$ materials
YSZ	Yttria Stabilised Zirconia, (Zr, Y)$O_{2-\delta}$ materials

❝ *Do it the hard way and it's easy sailing...* ❞
Hart/Rodgers (1940)

Chapter 1
Introduction

1.1 Historical notes, context and motivation of this research project

The study of proton conduction in oxides found its roots at the beginning of the second half of the 20th century, when technological advances had allowed refinement of the industrial manufacture of steel and glass by close investigation of the chemistry and physics involved. The study of the role of water vapour in steelmaking slags, as a means to determine the hydrogen content of the metal[1], provided the first observation that hydrogen can be incorporated as a result of the reaction of an oxide system with water vapour. Later, the solubility of water vapour and hydrogen in crystalline oxides was discussed in terms of interstitial defects for several transition metal oxides, such as Cu_2O, CoO, NiO[2], TiO_2 (rutile)[3], while Shores *et al.*[4] showed protonic conductivity in acceptor-doped ThO_2, and Pope *et al.*[5] proposed mobile protons in $BaTiO_3$.

As awareness and a more comprehensive understanding of the anthropic impact on the biosphere arose among intellectuals and inside western think tanks[6], the issue of diversifying energy sources became a strong drive for the study of such a property in crystalline solids. Since the 1970s, in fact, in the first reviews of the field compiled by Bruinink[7] and Glasser[8], proton migration in solids was acknowledged as a desirable property for the development of more advanced fuel cell devices. During the 1980s the study of proton conducting ceramics acquired a stronger impulse, when Iwahara and co-workers[9–11] demonstrated high-temperature proton conductivity in Ce-based perovskites with alkaline-earth elements in wet conditions *via* hydrogen generation by steam electrolysis. Until then, reported conductivities in protonic conductors were well below 10^{-4} S/cm, whereas these perovskite systems showed an increased performance by several orders of magnitude. It was a surprise that proton migration was faster in such structures, with large cations and long O–O distances, while the best barriers displayed a very close packing of the oxygens, like in α-Al_2O_3. This was explained in the 1990s when it was found that the dynamics of the oxygen ion sublattice assist the proton in breaking the O–H bond and that a momentary shortening of the OH···O distance helps the jump of the proton to the neighbour oxygen[12].

During the late 1980s and the following years, the field of solid state protonics grew up. Those years saw the first international conferences on Solid State Protonic Conductors, held in Europe, which constituted the basis for the nucleation of a community. In the last two decades, the number of publications in the field of proton

conducting oxides has steadily increased (*fig. 1.1*), which shows not only the growing interest in this new field, but also witnesses the effort that the scientific community has put into understanding what attributes make a good protonic conductor. Research has extended our knowledge, with new families of proton conducting ceramics, and innovative synthetic routes paving the way for potential marketable applications[13].

The work included in this thesis focusses on a perovskite-structured proton conducting system alternative to the most known zirconate and cerate ones. The observation of high levels of proton conductivity (> 10^{-3} S/cm) in heavily Sc-substituted $BaTiO_3$[14,15] opened new avenues of research into materials design and proton transport since oxygen vacancies distribution in these highly defective phases adds new insights into the current understanding of defects interaction. The first strategy for attaining enhanced proton conductivity, in fact, relied on acceptor-dopants as key to the introduction of *more* protonic defects through creation of *more* oxygen vacancies. Conductivity measurements on zirconate and cerate systems have shown, though, that most acceptor-dopants are only effective up to 30 mol% *ca.*[16] because of solubility limits and since vacancies association and clustering hinders proton transport by making those new vacancies inaccessible. The novelty in cubic heavily Sc-substituted $BaTiO_3$ is that Sc, Ti and the oxygen sublattice interact differently and high levels of oxygen deficiency in dry phases coexist with significant proton conductivities in the hydrated ones. The peculiarities of the Sc_2O_3-$BaTiO_3$ solid solution are here reported with regard to the structural features in the extended and local environments, the dehydration behaviour, and the characteristics of the proton sites.

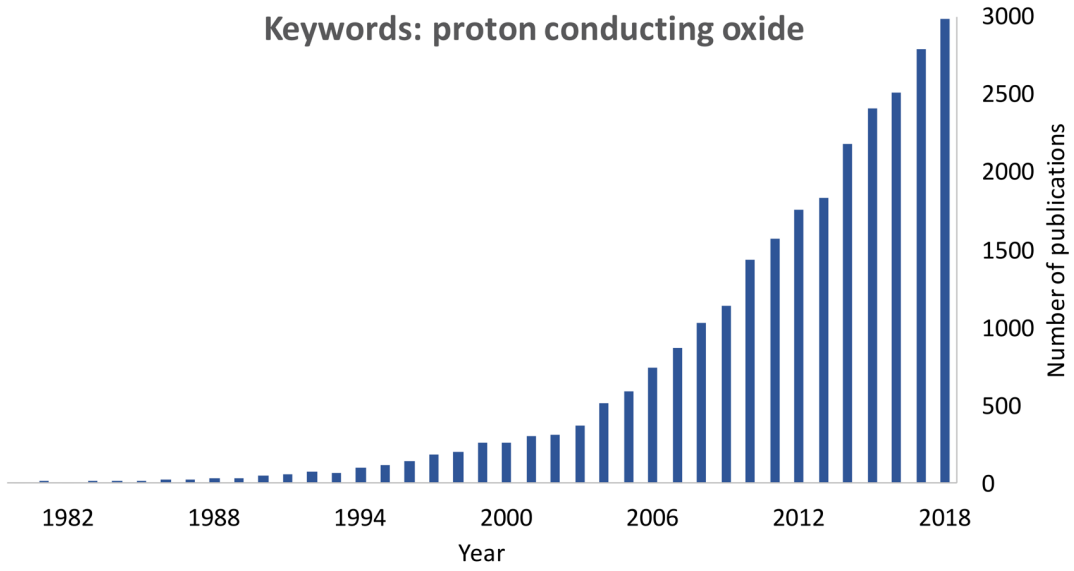

Fig. 1.1 Summary of the results of the search query "proton conducting oxide", including all fields, according to the Scopus database. The large majority of all documents, the 99%, includes scientific articles (78%), reviews (10%), conference papers (6%), book chapters (4%) and books (1%).

Chapter 2
Protons in condensed matter

2.1 Introduction

Protons are part of a sub-division of matter called subatomic particles and are characterised by a charge equal to that of the electron, *e*, but of opposite sign. Slightly lighter than neutrons, protons are thousands of times heavier than electrons (1.67×10^{-27} kg *vs*. 9.11×10^{-31} kg). As positively charged hydrogen ions, they are a peculiar chemical species, one without an electron shell. For this reason, we usually find them within the spatial extension of the electron density of another species.

Hydrogen dissolves in oxides in equilibrium with a source gas, like H_2 or water vapour. Being a donor, the protonic defect is positively charged, and its concentration is enhanced by acceptor-doping the host phase. These are, in general, oxides where the acceptors are compensated by oxygen vacancies in the dry state. When in equilibrium with water vapour, the oxide dissolves the protons and fills the vacancies, according to the reaction expressed in the Kröger-Vink notation:

$$H_2O\ (g) + \ v_O^{\bullet\bullet} + O_O^{\times} \ \rightleftarrows \ 2\ OH_O^{\bullet} \qquad (2.1)$$

The transport of protons is explained according to two limiting cases models, the vehicle mechanism, and the Grotthuß mechanism. The vehicle mechanism involves the diffusion of a proton along with a molecular species, such as H_3O^+ and NH_4^+, whereas the counter diffusion of the unprotonated vehicle allows the net transport of protons. This kind of diffusion is dominant in concentrated aqueous solutions of acids, in solids with open structures, and explains protonic diffusion in hydrated acidic polymers.

In oxides, the proton, found bonded to an oxide ion, moves from an oxide ion to a neighbouring one within hydrogen bonds, with the subsequent reorganisation of its environment. That is the principle of the structure diffusion, and it bears similarities to the so-called Grotthuß mechanism describing proton motion in water.

To date, proton transport is found in a number of different systems, and solid-state protonic conductors are classified in different ways, according to their chemical structure or composition, preparative method, conduction mechanism, and so on. A practical way of classifying proton conducting materials is the approach based on the operative temperature range:

– low temperature, below 150 °C, for hydrated sulfonated polymers, such as Nafion (a sulfonated fluorocarbon), and heteropolyacid hydrates, such as $H_3PMo_{12}O_{40}\cdot29H_2O$;

– intermediate temperature, between 150 and 350 °C, for oxide hydrates, such as $Sb_2O_5 \cdot 4H_2O$ and $SnO_2 \cdot nH_2O$;
– high temperature, above 400 °C, for crystalline mixed oxides, such as perovskite, brownmillerite, and pyrochlore systems.

An exhaustive treatment of all systems is beyond the scope of this text; examples of technical applications will be given, before introducing the materials that are the object of this study, ceramic protonic conductors and, in particular, those based on perovskite systems.

2.2 Technical applications of proton conducting ceramic materials

Despite the fact that the development of a benchmark material for fuel cell applications is still ongoing, proton conducting ceramics demonstrate marketable materials. An example is provided by In-doped $CaZrO_3$, used as conducting material in hydrogen sensors for monitoring the degassing process of molten aluminium before casting[17,18] and for the continuous casting of copper wire[19,20]. A promising application for the same system is found in the chemical control of coolants in nuclear reactors[21]. Along with this success story, a number of potential applications are being studied, most notably separation membranes in fuel cells, briefly reported in the following paragraphs.

High temperature ceramic fuel cell devices and their market

A ceramic fuel cell is an electrochemical cell, consisting of a gas-tight dense polycrystalline membrane (the electrolyte) separating the anode and cathode compartments; it transforms chemical energy (Gibbs free energy) into a direct electric current. This technology could allow a dramatic change in the way electricity is produced. The chemical energy, in fact, is provided by a hydrogen source and, by means of a redox reaction with oxygen (or another oxidising agent), water is formed as the by-product, while electrons are harnessed and forced to flow through a circuit to power electrical appliances. Along with fuel flexibility, these characteristics make the operation of the device advantageous over classic combustion engines because it is virtually pollutant-free and with the cogeneration of electricity and heat efficiencies above 80% are attainable[22].

Among ceramic fuel cells a distinction is made according to the nature of charge carriers in the electrolyte membrane. In a Solid Oxide Fuel Cell (SOFC), the electrolyte allows the transport of oxide ions from an electrode to the other. Oxygen, O_2, is reduced to O^{2-} at the cathode side and combines with protons at the anode. Classically, these separators are made of yttria-stabilised zirconia, YSZ, the most widely used material for this application. Most of the common cells based on oxide ion conducting ceramics operate at temperatures above 600 °C[23] and involve the use of expensive materials to withstand the harsh operating conditions, which in turn raise the operating cost and their price on the market, limiting their presence to small-scale development to pilot-scale test and demonstration.

In a fuel cell that features a proton conducting ceramic as electrolyte material, a Proton Conducting Fuel Cell or Protonic Ceramic Fuel Cell (PCFC), charge carriers are protons. Oxidised at the anode side, hydrogen combines with oxygen at the cathode. This provides an intrinsic advantage over SOFC because this design avoids the dilution of the fuel at the hydrogen electrode. Further, the smaller size of the proton with respect to a O^{2-} ion yields higher mobility of the species in the dense ceramics, and allows the operating temperature of the cell to be reduced (migration energies are in the range 0.4-0.6 eV[24] for protons in perovskite systems and 0.8-1 eV[25] for oxide ions in YSZ). However, operating temperatures above 500 °C[26], lattice matching of the components around the electrolyte membrane and densification procedures still hinder the commercialisation. Notably though, the discovery in 2004 of solid-state reactive sintering[13] has demonstrated sintering methods suited for commercial production and hence given a strong impulse to research (see *fig. 1.1*). *Fig. 2.1* shows a schematic representation of the two ceramic-based cells, SOFC and PCFC.

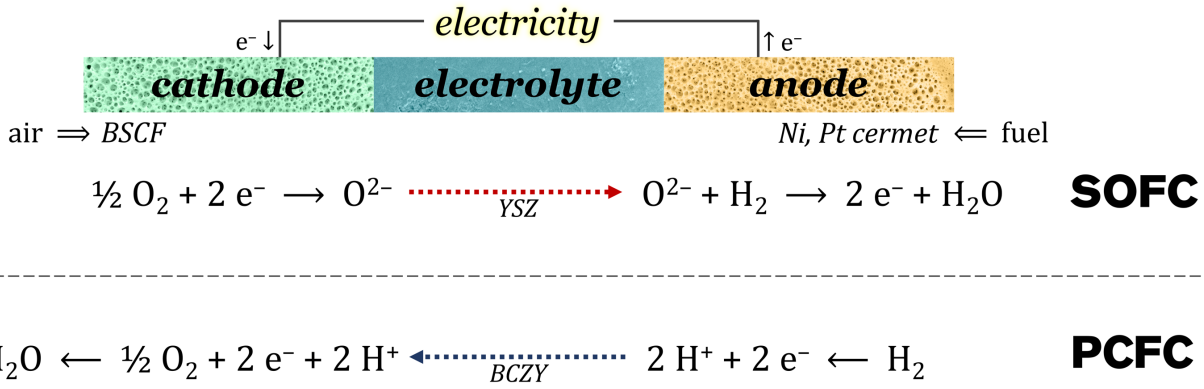

Fig. 2.1 Schematic representations of a fuel cell device based on an oxide ion conducting (SOFC) or a proton conducting (PCFC) ceramic membrane. State of the art cell elements materials are Ni or Pt cermets for the anode, (Ba, Sr)(Co, Fe)$O_{3-\delta}$ perovskites for the cathode, (Zr, Y)$O_{2-\delta}$ fluorites as electrolyte in SOFC, Ba(Ce, Zr, Y)$O_{3-\delta}$ perovskites as PCFC electrolyte.

Hydrogen sensors

As mentioned, protonic conductors are used as the electrolyte in hydrogen concentration cells for detecting H_2 gas. In such an electrochemical cell (*fig. 2.2*), the electromotive force (EMF) is directly related to the ratio of the hydrogen partial pressures at the two sides; if one of the two is known, the other can be determined from EMF measurements. If the cell is used as a steam concentration cell, water vapour in air can be detected, and, with modifications, hydrogen-containing compounds like alcohols and hydrocarbons. In the metallurgical industry, this technology is already put to use, allowing to monitor the hydrogen concentration in molten metals, by using sensors containing proton conducting ceramics.

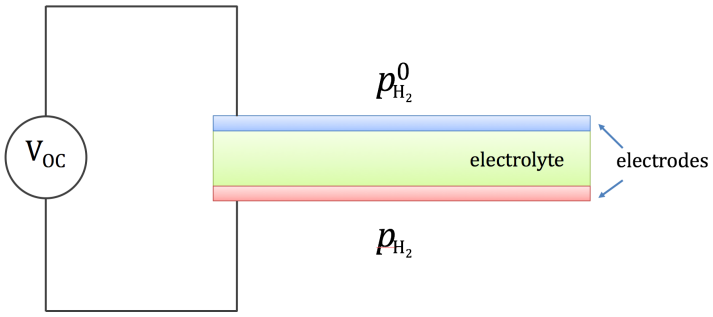

Fig. 2.2 Schematic representation of a hydrogen sensing device.

Membranes for hydrogen separation

Proton conductors are also used for the separation of hydrogen from a gas mixture. The separation can be carried out by electrochemically pumping hydrogen, that is by applying a direct current to a cell, or *via* hydrogen permeation by means of a proton-electron mixed conductor. For this latter case, no external electric power supply is necessary, and a simple hydrogen separator can be constructed, where the membrane uses the hydrogen potential gradient as the driving force for the hydrogen transport.

Steam electrolyser

Steam electrolysis works on the principle of reversing the operation of a fuel cell. Water is introduced into the anode side as steam, and it is split into oxygen molecules and protons. Electrons flow through a circuit, reducing protons to hydrogen gas at the cathode side. Oxide ion conducting electrolytes are also used for steam electrolysers, but the use of a proton conducting one suppresses the need for the separation of hydrogen from water (*fig. 2.3*).

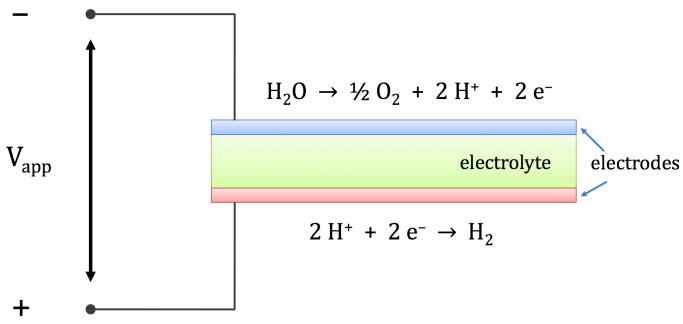

Fig. 2.3 Schematic representation of a steam electrolyser.

Another important aspect deals with the operation temperature: *fig. 2.4* compares the conductivity of YSZ, $Zr_{0.92}Y_{0.08}O_{1.96}$, with that of BCY, $BaCe_{0.9}Y_{0.1}O_{3-\delta}$, one of the best proton conductors. While at high temperatures the conductivities of the two systems are comparable, at 600 °C BCY displays a better performance, bringing advantages to the application of the material in steam electrolysis, when it comes to material cost and heat management.

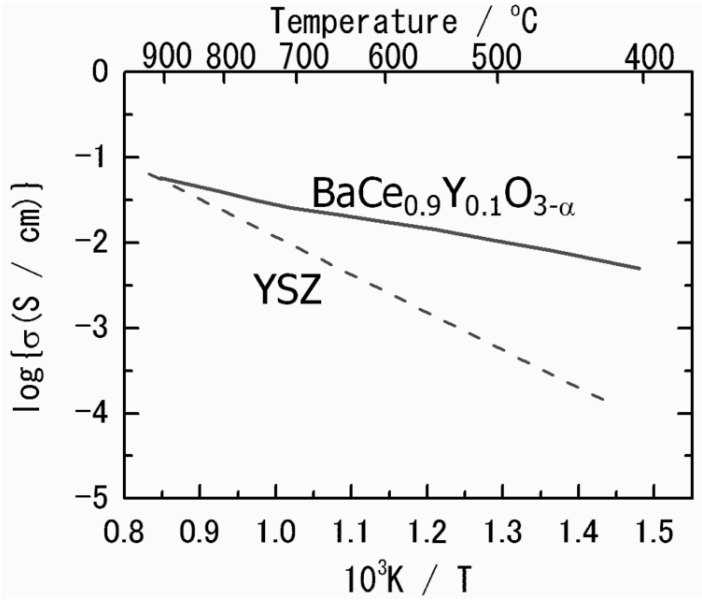

Fig. 2.4 Comparison of the electrical conductivities of YSZ and BCY[19].

Membrane reactors

Proton conducting ceramics are also used as catalytic membrane reactors, to improve selectivity and yield of hydrogenation/dehydrogenation reactions for the production of a large variety of commodity chemicals, energy carriers and synthetic fuels[27]. Studies of a number of industrially relevant reactions show promising results: the dehydrogenation of alkanes to alkenes and H_2[28], the dehydrogenative coupling of methane to obtain C_2 hydrocarbons[29], the selective elimination of hydrogen from the reacting mixture in the water gas shift reaction[30], the synthesis of ammonia from steam and nitrogen at atmospheric pressure[31], the direct conversion of methane to aromatics[32], and the production of compressed hydrogen from methane[33].

Chapter 3
Review of ceramic protonic conductors

3.1 Introduction

Since the pioneering work of Iwahara and co-authors[9–11], that demonstrated the conduction of protons in perovskite-structured oxide systems and laid the foundations of the field of solid-state protonics, many important advances have been made. The problem of proton conductivity in condensed matter was tackled from the phenomenological point of view, distinguishing so the kind of materials for which proton conductivity was observed on the basis of the mechanism of proton transport, vehicle or Grotthuß mechanism, from which the first systematisation of the structural and chemical features of proton conducting materials was derived[34–36].

In ceramic materials, where the Grotthuß mechanism is the accepted one, the study of the dynamics of the oxygen ion sublattice in assisting the proton migration[12,37–39] allowed the identification of the two main steps for proton transport in perovskite systems[37,39–45]: the reorientation of the protonic defect around its oxide ion, and the jump it makes to move forward to the neighbouring oxide ion. The study of the energies involved indicated that the jump is the rate-limiting step[24,46]. The identification of the main properties required for a successful ceramic proton conductor was therefore possible[24,46,47], and that led to the individuation of Y-doped $BaZrO_3$-based materials as the best proton conductors[44]. Despite the remarkable conduction properties, in these phases the grain boundaries tend to be relatively resistive and the conductivity increases by orders of magnitude on going from the small-grained material to the single crystal[24].

In a visually powerful way, Norby[48] individuated the presence of a "gap" in the plot of proton conductivities of different materials as a function of temperature and urged that an improved understanding of protons and proton transport is crucial for the advancement of the field. Attention was then directed at multiple aspects. The determination of the proton crystal sites and of the precursors to the elementary processes of proton transport, with the study of the local environment[49–54] and the vibrational motions of protons in perovskite-structured systems[55–57], to give a more accurate representation of the reality of the materials. The study of the oxygen vacancies[58–60], their ordering[61–65] and their effect on the structure with their filling[63,66–68], as a source for the understanding of the lattice dynamics that proton

transport underlines. Alongside, the research on new classes of complex oxide materials[69–77] for which proton transport is appreciable defines the boundaries of the field and allows a more complete systematisation.

In the following paragraphs, ceramic proton conducting systems are reviewed with regard to their structural features, the defects chemistry, the incorporation and mobility of protonic defects, the charged species that contribute to the electrical conductivity.

3.2 Perovskites

Perovskites are a class of compounds whose structures relate to that of the mineral form of $CaTiO_3$, discovered in the Urals in 1839, and named *Perovskite*. Nowadays, we refer to this family of compounds with the use of the general formula ABX_3. The ideal crystal structure was first described by Goldschmidt in 1926[78], while the first XRD work on $BaTiO_3$ was published in 1945[79]. These materials have been intensively studied since the middle of the 20th century because of their useful properties: initially dielectric, piezoelectric and ferroelectric, with the study of the properties of $BaTiO_3$. To date, a number of physical properties has been studied and exploited, ranging from magnetic, to multiferroic, electronic conductivity, superconductivity and thermal and optical properties[80].

These phases also show a wide range of chemical attributes. They are used as electrode materials for solid oxide fuel cells where materials with high oxide ion conductivity, electronic conductivity and mixed ionic/electronic conductivity are required. Many perovskite phases show useful catalytic and redox behaviour, often dependent upon the presence of chemical defects in the phase. This complexity results from two main characteristics of this family of compounds: it displays a huge variety of crystal structures sub-types, from the simple cubic, to modular phases; in addition, both the chemical and physical properties can be conveniently tuned by substitution into all or some of the A-, B- and X-sites. This wide-ranging flexibility includes the formation of perovskites in which the A cation is replaced by an organic molecule, like in methylammonium lead iodide[81], now intensely studied as the core of high efficiency, perovskite photovoltaic cells[82]. These features provide us with an invaluable toolkit for designing ceramic materials.

3.2.1 Structural features

Perovskite phases are referred to with the general formula ABX_3, where A is usually a large cation, B represents a medium to small sized cation, and X is an anion. The idealised structure is cubic, as shown in *fig. 3.1*. The standard crystallographic description choses the A cation as origin of the unit cell; nonetheless, it is common to find representations that adopt the B cation as origin, especially when the polyhedral arrangements of the anions coordinating B are highlighted. In this case, it is convenient to think of the structure as built-up from an array of vertex sharing BX_6 octahedra.

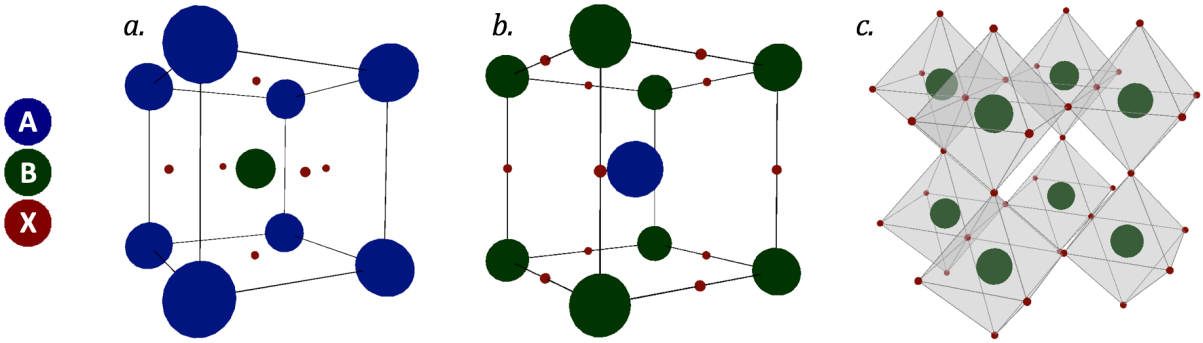

Fig. 3.1 Three representations of the cubic perovskite structure.
(*a.*) the largest cation A is at the origin of the unit cell, the *1a* crystal site at (0, 0, 0), while the smaller cation B is in the *1b* site at (½, ½, ½).
(*b.*) a usual way of depicting perovskites, has the positions of the cations inverted.
(*c.*) the vertex sharing octahedral arrangement of the anions X coordinating B is highlighted, and the cation A erased for clarity.

Goldschmidt suggested a mathematical relationship to be used as a predictive tool for the formation of a perovskite-structured phase, starting from a pair of cations:

$$t = \frac{(r_A + r_X)}{\sqrt{2}\,(r_B + r_X)} \tag{3.1}$$

where r_i is the radius of the i-th ion in its coordination environment.

The tolerance factor, t, was proposed at a time when few crystal structures had been determined; to date, many perovskite structures have been described and it is usual now to utilise the observed tolerance factor, t_{obs}:

$$t_{obs} = \frac{(A-X)}{\sqrt{2}\,(B-X)} \tag{3.2}$$

where (A–X) is the average of the measured bond lengths between the A cation and its surrounding 12 anions, and (B–X) is the average of the measured bond lengths between the B cation and its surrounding six anions.

Empirically, if t lies in the approximate range 0.9-1.0, a cubic perovskite structure is a reasonable possibility. If $t > 1$, that is large A and small B, a hexagonal packing of the AX_3 layers is preferred, and hexagonal phases form. When t ranges between 0.71 and 0.9, the structure, and particularly the octahedral framework, distorts and crystal symmetry is lowered. Lower values of t, when the A and B cations are of similar size, are associated with the ilmenite, $FeTiO_3$, structural type.

This concept can also be extended to more complex perovskites, like A-site substituted phases $A_{1-x}A'_xBX_3$, or B-site substitution $AB_{1-x}B'_xX_3$, respectively:

$$t = \frac{[(1-x)\, r_A + x\, r_A + r_X)]}{\sqrt{2}\,(r_B + r_X)} \tag{3.3}$$

$$t = \frac{(r_A + r_X)}{\sqrt{2}\,[(1-x)r_B + x\, r_B + r_X)]} \tag{3.4}$$

and

$$t_{obs} = \frac{< A-X >}{\sqrt{2} < B-X >} \tag{3.5}$$

where <A–X> and <B–X> represent the average bond lengths for the links A–X, A′–X, and the links B–X, B′–X, respectively. Both equations can also be generalised to more complex structures (A, A′, A″…) (B, B′, B″…) $(X, X', X''\ldots)_3$.

3.2.1.1 Perovskite-related structures

3.2.1.1.1 Double perovskites

When more ionic species are present, in which the ionic sizes or the charges differ enough, the lattice energy can be reduced by ordering some or all of the ions over the available crystallographic sites. The most widely encountered ordering pattern is that found in the double perovskites with a formula $A_2(BB')O_6$, in which there is a B-site cation substitution. The most common ordering pattern corresponds to the two different cations, B and B′, arranged in a chessboard pattern, often called rock-salt ordering (*fig. 3.2*). As distinct from B, B′ ordering, ordering of A, A′ cations frequently takes the form of layers …A, A′, A, A′… . These structures tend to occur in non-stoichiometric oxygen-deficient phases and are especially associated with the perovskite-related layered structures.

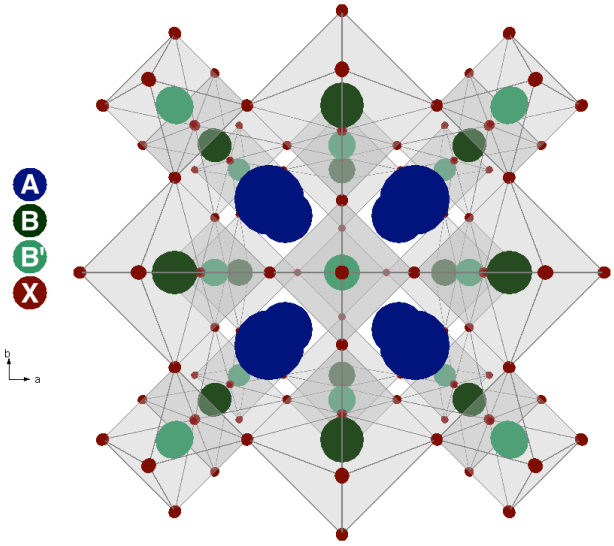

Fig. 3.2 Representation of the structure of a cubic ABB'X_6 double perovskite.

3.2.1.1.2 Ruddlesden-Popper phases

The perovskite structure can be modified by introducing one or more additional layers of different structures between perovskite blocks. When the layers have a rock-salt type of arrangement, the so-called Ruddlesden-Popper phases are formed, with the general formula $A_{n+1}B_nO_{3n+1}$. The simplest member of the series, with $n = 1$, adopts the K_2NiF_4 kind of structure and is described as a stacking of single slabs of perovskite (*fig. 3.3*). Increasing the perovskite slab thickness, while keeping the inter-slab structure the same, generates the phases with $n = 2$, $n = 3$, and so on, up until $n = \infty$, that exemplifies the simple perovskite structure. The thickness of the individual layers and the charge distribution between them can be tailored in order to control physical and chemical properties of such phases. Some of these can topotactically intercalate water into their structure, even at room temperature[83].

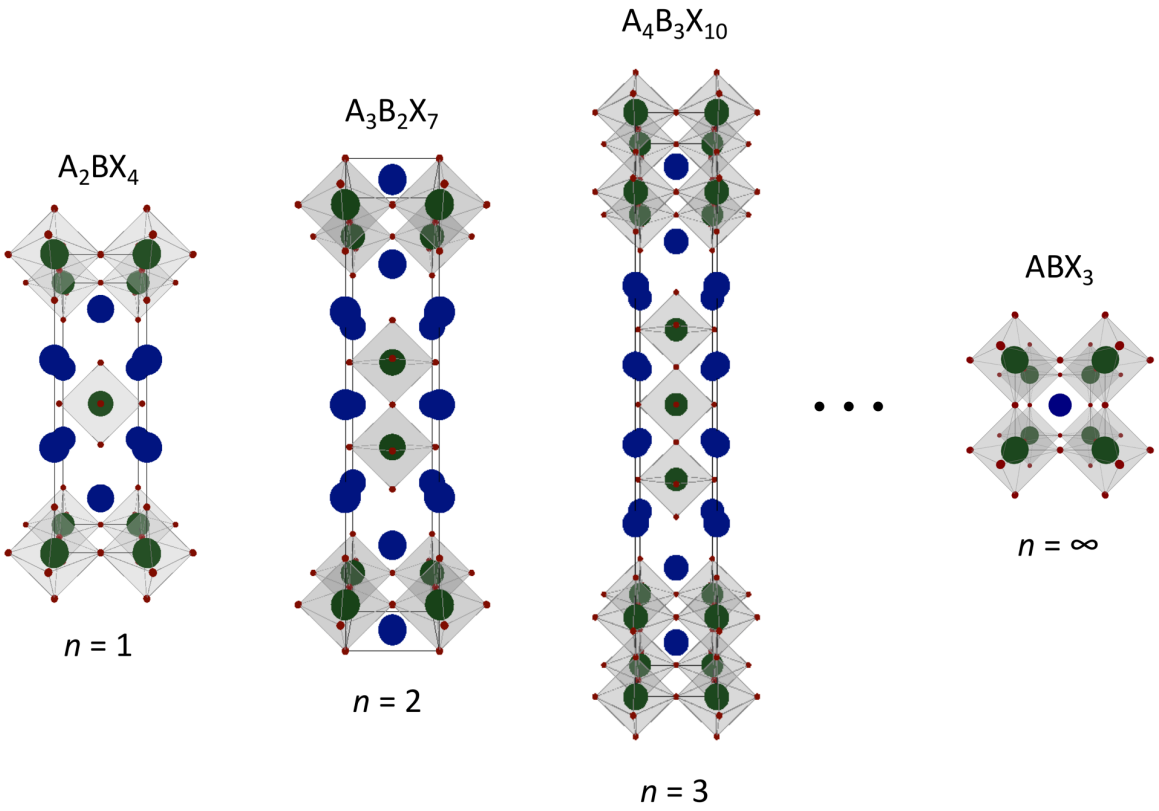

Fig. 3.3 Representations of the crystal structures of the ideal Ruddlesden-Popper series with general formula $A_{n+1}B_nX_{3n+1}$.

3.2.2 Protonic defects: formation, stability, mobility

Protonic conduction in oxides (in this text, with particular regard to perovskite and perovskite-like materials) is achieved by exploiting the defect chemistry of crystalline phases. While perfect crystals may exist, it is generally common to come across imperfect ones, crystals that contain defects that are generated during the growth (*fig. 3.4*). In this case, we talk about defects in stoichiometric compounds, which is when the composition

does not change with the formation of the defect. Schottky defects are formed when a missing ion produces the absence of its counter-ion, in order to maintain electroneutrality. When a species is displaced from its expected lattice site and occupies a site expected to be empty (for example an interstitial site), a Frenkel defect is formed. These are called *intrinsic* defects, meaning that they are not artificially created, but arise in the native compound from the thermodynamics of their synthesis history.

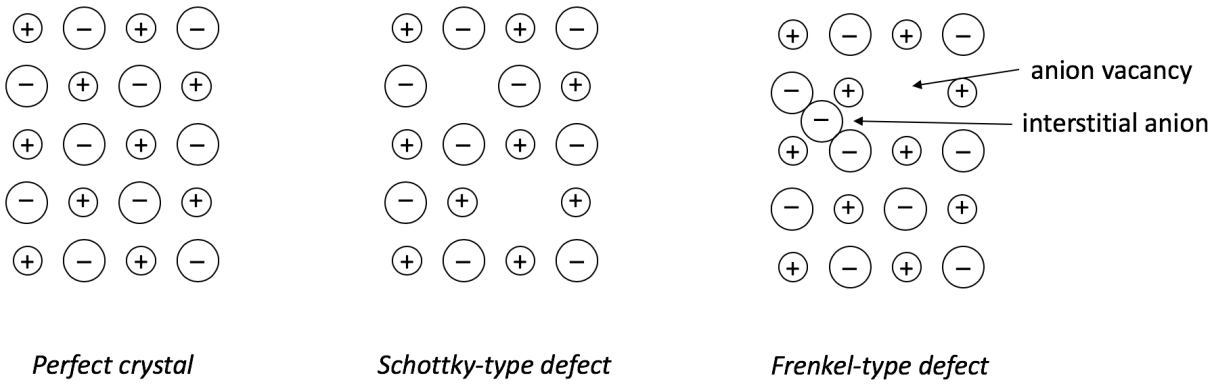

Fig. 3.4 Types of point defects in ionic crystals.

When, instead, defects are deliberately introduced, non-stoichiometric compositions are formed as a result of impurities or doping agents; these defects are called *extrinsic*. Using a doping species is the most common way of introducing extrinsic defects in an original compound, where the dopant can either occupy an interstitial site or replace a species in its crystal site. A dopant can be either a donor or an acceptor species, each yielding different results in order to restore charge balance, and the corresponding resulting materials are referred to as *extrinsic semiconductors* (*fig. 3.5*). A donor will contribute to the formation of cationic vacancies, or electronic states near the conduction band, E_D (*n*-type semiconductor); an acceptor will typically produce oxygen vacancies, or electronic holes, that is acceptor levels above the valence band, E_A (*p*-type semiconductor)[84].

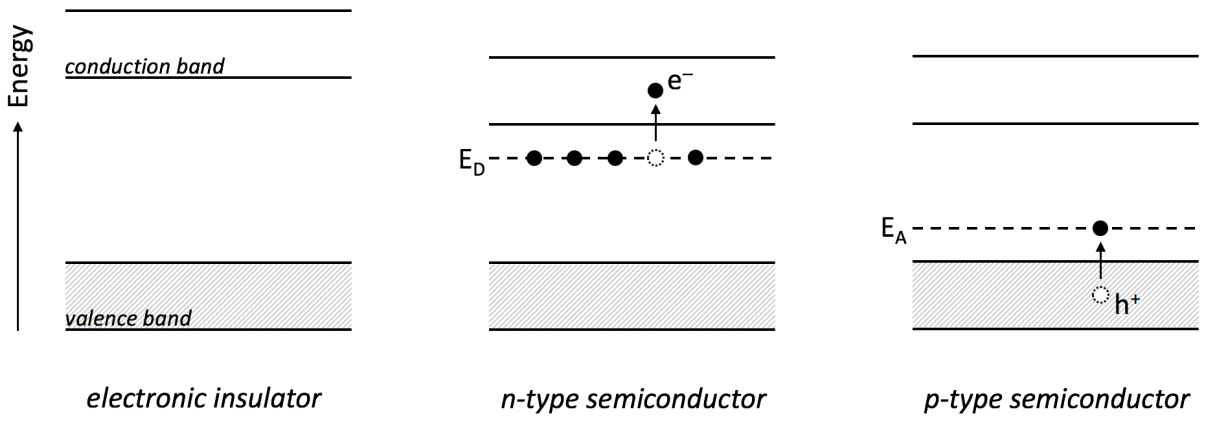

Fig. 3.5 Schematic of the band structure of an electronic insulator and of *n*- and *p*-type semiconductors.

The technical importance of defect chemistry in crystals was understood very early, hence Kröger and Vink[85] in the 1950s proposed a set of symbols to describe defects in a crystal. The Kröger-Vink notation is still in use and summarised in *table .31*.

Tab. 3.1 Kröger-Vink's defects notation.

Defect type	***notation***
Metal vacancy at metal (M) site	v_M
Non-metal vacancy at non-metal (Y) site	v_Y
Impurity metal (A) at metal (M) site	A_M
Impurity non-metal (Z) at non-metal (Y) site	Z_Y
Interstitial metal (M)	M_i
Interstitial non-metal (Y)	Y_i
Neutral metal (M) vacancy	$v_M^\times$
Neutral non-metal (Y) vacancy	$v_Y^\times$
Metal (M) vacancy with negative effective charge	v_M'
Non-metal (Y) vacancy with positive effective charge	$v_Y^\bullet$
Interstitial metal (M) with *n* positive effective charges	$M_i^{n\bullet}$
Interstitial non-metal (Y) with *n* negative effective charges	$Y_i^{n\prime}$
Free electron	e'
Free hole	$h^\bullet$
Neutral associated defects (vacancy pair)	$(v_M v_Y)$
Associated defects with positive effective charge	$(v_M v_Y)^\bullet$

In the general case of an acceptor species, *A*, substituting the metal, *M*, in a binary oxide, oxygen vacancies in the dry state are formed as charge-compensating defects:

$$MO + A_2O \rightleftarrows 2\,A_M' + M_M^\times + 2\,O_O^\times + v_O^{\bullet\bullet} \qquad (3.6)$$

Once the vacancies formed, protons can be introduced into the structure as point defects by interaction between them and water vapour as in *equilibrium 2.1* (*fig. 3.6*). A proton defect, according to the Kröger-Vink notation would be indicated as $OH_O^\bullet$, a hydroxyl at oxide site bearing one positive charge. So far, the literature of high-temperature protonic conductors is dominated by acceptor-doped systems: among these, the highest proton conductivities are observed for acceptor-doped $BaCeO_3$ and $BaZrO_3$.

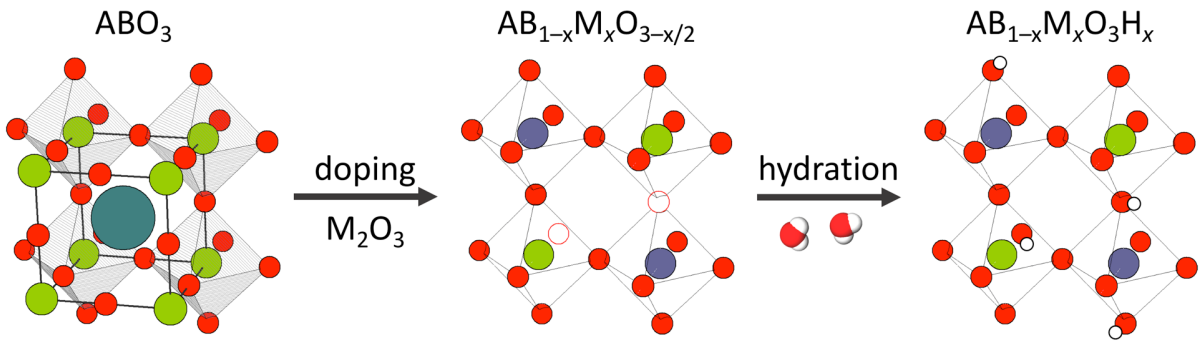

Fig. 3.6 Schematic representation of the formation of extrinsic protonic defects. In the II-IV perovskite host phase of this example, vacancies are procured *via* acceptor-doping with the trivalent metal in the oxide M_2O_3, and water is incorporated in a following step, this way introducing protons inside the structure.

In principle, the number of protonic defects at saturation equals that of the dopant and when the material is hydrated their concentration is constant at room temperature. The concentration of protonic defects diminishes with increasing temperature because of the exothermic nature of the hydration reaction (*equilibrium 2.1*): the material starts to dehydrate above a given temperature, which decreases with increasing enthalpy and/or decreasing entropy. Also, the hydration reaction becomes more exothermic with decreasing electronegativity of the cations interacting with the lattice oxygen; the most exothermic ΔH_{hyd} have been found when A- and B-site cations have similar electronegativities. The equilibrium constant of the hydration reaction decreases, instead, with increasing electronegativity of the B-site cation: for Ba-based perovskite systems, the equilibrium constant decreases in the order cerate > zirconate > titanate. Kreuer[44] suggested that basicity is a crucial parameter for perovskites, expressing their affinity for protons: the lower the electronegativity of the B-site cation, the more basic the oxygen and higher the ability to react with water vapour to give a proton defect. On the other hand, a higher basicity will make the phase unstable towards acidic gases, such as CO_2 and SO_2. Therefore, the stability against the formation of carbonates and hydroxides increases in the order cerate < zirconate < titanate.

The reduction of the crystal symmetry is another important factor for the stability of protonic defects. $BaCeO_3$ and $SrCeO_3$ are equally stable towards the formation of carbonate, but protons are less stable in the latter, which displays a stronger orthorhombic distortion. This suggests that the regularity of the oxide ion framework plays an important role for the stabilization of protonic defects and that the choice of the acceptor-dopant is crucial because of potential local symmetry effects. Norby *et al.*[86] collected data on hydration thermodynamics for more than forty perovskite systems, but nothing conclusive could be said about the correlation between entropy and the material properties. ΔH_{hyd} does correlate to the Goldschmidt tolerance factor, becoming more exothermic as *t* decreases below unity; in other words, the stability of protonic defects is affected by deviations from cubic symmetry[87].

In the same way, the mobility of the protonic defects is decisively related to the dynamics of the oxygen network. The transport mechanism is characterised by a two steps process: a rotational diffusion of the protonic defect around its oxide ion and a jump towards a neighbouring one[12,44] (*fig. 3.7*).

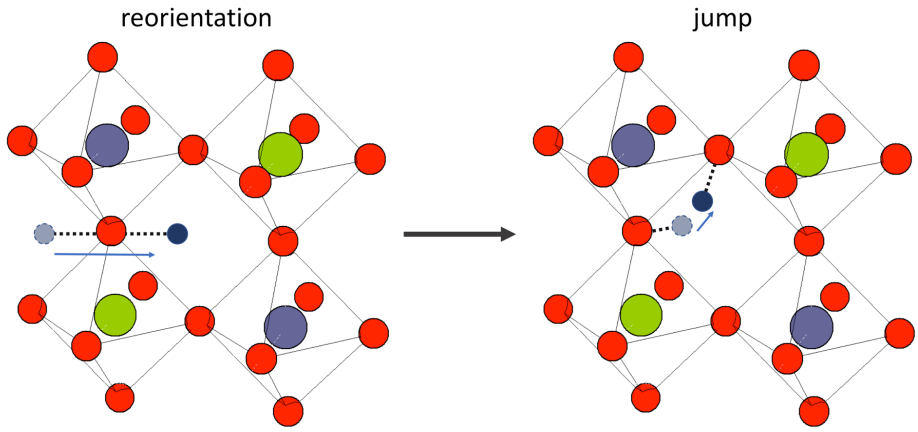

Fig. 3.7 Schematic illustration of the Grotthuß transport mechanism of protonic defects in the perovskite phase. The proton conveniently positions itself for the jump, then completes its *passage* by ending on a neighbour oxygen.

The last step is the rate-limiting one, with activation energies spanning from 0.4 to 0.6 eV[24]; rotation, or reorientation, is fast and characterised by a small activation energy, < 0.1 eV[46]. Molecular Dynamics simulations have helped to build a conceptual understanding of the mechanism of transport. Since an OH bond will be broken to complete the process, it has been found that the jump is assisted by an instantaneous distortion of the oxygen network, with the OH···O distance becoming smaller (*fig. 3.8*). On the other hand, structural distortions, lowering the symmetry of perovskites away from the ideal cubic case, impact negatively on proton transport, leading to higher activation energies[47,88]. The B-site cation also influences the mobility of protons because of the repulsion that it exerts on the proton itself. In cubic perovskites with pentavalent B-site cations (I–V perovskites), in fact, the activation enthalpies of proton mobility is significantly higher than in perovskites with tetravalent B-site cations (II–IV perovskites)[46].

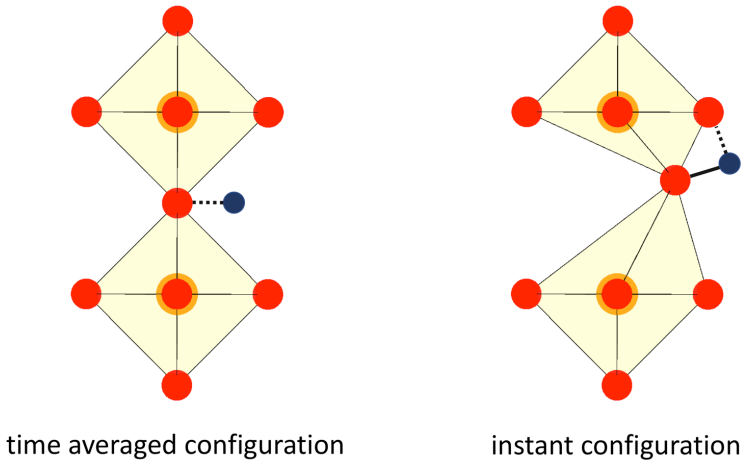

Fig. 3.8 Schematic depiction of the O lattice-assisted dynamical hydrogen bonding in a cubic perovskite. The time averaged and instant configurations illustrate the two limit cases, the first one being the average picture seen in a diffraction experiment. The free energy gained by hydrogen bond formation competes with the free energy required for the lattice distortion necessary for the formation of the bond itself.

3.2.3 Cerates

Among perovskite systems, those based on $BaCeO_3$ display the highest proton conductivities, in the order of 10^{-2} S/cm at 650 °C. This is attributed to the large ionic radius of Ce^{4+} (0.87 Å in a 6-coordinated environment) and its relatively low electronegativity, and to the low contribution of grain-boundaries to the total resistivity of ceramic samples. The most investigated systems are those doped with trivalent acceptor species. The conductivity of $BaCe_{1-x}Ln_xO_{3-\delta}$ solid solutions increases with x and reaches the highest values at x = 0.10-0.25, depending on the dopant ion (with Ln = rare earth element). With higher concentration of dopants, the conductivity decreases as a result of the appearance of impurity phases of the type $BaLn_2O_4$[16]. Most of rare earth elements, in fact, reach their solubility limit into the Ce sublattice at concentration of 20-30 mol%. Despite the promising electrochemical performances, cerate systems suffer a low thermodynamic stability in the presence of water and acidic gases. In addition, both undoped $BaCeO_3$ and acceptor-doped solid solutions exhibit polymorphism as a function of temperature and degree of substitution, which limits their application in high-temperature electrochemical devices because of the mechanical compatibility required with the other elements of the assembly.

$BaCeO_3$ is a perovskite with orthorhombic distortion, crystallising in the space group *Pmcn* at room temperature. It exhibits three phase transitions, *Pmcn* → *Incn* → *R3c* → *Pm3m* on heating[63]. Acceptor-dopants influence the temperatures at which the transitions take place but can't stabilise the cubic phase. In the case of $BaCe_{1-x}Y_xO_{3-\delta}$, at room temperature, for x = 0.10, 0.15 orthorhombic structures are displayed, with space groups *Pmcn* and *Incn* respectively[89]. For x = 0.20, 0.30 monoclinic (*I2/m*) and rhombohedral ($R\bar{3}c$) phases are observed[89]. Neutron diffraction experiments performed on the x = 0.20 solid solution show transitions at 500 °C (orthorhombic, *Imma*), 600 °C (rhombohedral,

$R\bar{3}c$) and 800 °C (cubic, $Pm\bar{3}m$)[90], and correlate the stability of the phases with the degree of hydration: while phase transitions are depressed by the presence of oxygen vacancies (in particular the $Pm\,\bar{3}\,m \rightarrow R\,\bar{3}\,c$), the protonic defects reinforce the tendency for octahedral tilting, shifting to higher temperatures the stability of lower symmetry phases, and promoting a monoclinic *I2/m* structure at temperature below 400 °C[91].

$SrCeO_3$-related phases are isostructural with $BaCeO_3$ and exhibit proton conductivity, but the decrease of the size of the alkaline-earth ion in $ACeO_3$ produces worse electrochemical performances, with the appearance of electronic contributions to the total conductivity under reducing atmospheres[92]. In general, barium cerate compositions have demonstrated that dopant ions with larger ionic radius than Ce^{4+} lead to higher proton conductivity. More electronegative ions tend to lead to materials of higher stability with respect to carbonation, but smaller ions decrease the stability onset temperature and the improvement is associated with a large drop in conductivity[93].

3.2.4 Zirconates

$BaZrO_3$ related phases are among the most studied systems: zirconate solid solutions are chemically stable and show good conducting properties. $BaZrO_3$ systems are cubic perovskites with large lattice constants and favourable activation energies for proton transport, due to the covalency of the Zr–O bond that reduces the repulsive interaction of the B-site cation with the proton. With increasing size of the rare-earth dopant, a decrease in conductivity is observed; conductivity is also affected by an increase in dopant concentration above 20-30 mol%, due to the association of defects that impacts negatively on the mobility and stabilisation of protons. Defects association also plays a role in lowering the conducting properties of Sc-doped $BaZrO_3$, although low degrees of hydration seem to counter the trapping effect because of the electrostatic repulsion between protons and the oxygen vacancies surrounding Sc ions[94]. The same phenomenon is not observed in In-doped phases, where the proton concentration can be adjusted by increasing the In ion concentration up to 75 mol% in the Zr^{4+} site[95]. Furthermore, the presence of extended structural distortions, caused by the size mismatch, seems to have a favourable effect on proton transport[50], although conductivities remain modest, $< 10^{-4}$ S/cm at 600 °C.

A key feature of $BaZrO_3$ is the availability of an ideal acceptor-dopant, Y^{3+}. Although Sc^{3+} (0.74 Å) and In^{3+} (0.80 Å) closely match the ionic radius of Zr^{4+} (0.74 Å), the resulting doped phases are worse conductors, even if Y^{3+} is much larger (0.90 Å). On one hand, Y on the Zr site produces tetragonal distortions above 5 mol%; on the other hand, it leaves the basicity of oxygen almost unchanged, and this produces the best results in terms of electrochemical performance. DFT calculations suggest, in fact, a highly ionic nature of the Sc–O bonds, a small covalent (bonding) contribution to the predominant ionic character of the In–O bond, and mainly covalent Y–O bonds with an anti-bonding character[54]. In particular, $BaZr_{1-x}Y_xO_{3-\delta}$ electrolytes (BZY) seem to have the highest bulk protonic conductivities in the range 300-600 °C[44]. However, their total proton conductivity is lower

than that of their cerate homologues, because of the large contribution that grain boundaries give to the total resistivity.

One of the main challenges for this kind of materials stems from the very high sintering temperatures (above 1700 °C) that are required in order to obtain very dense ceramic samples. High temperatures are responsible for the volatilisation of BaO and the alteration of the composition of grains and grain boundaries, lowering the total conductivity. In order to overcome these issues, soft chemistry methods are generally used to synthesise these phases (sol-gel methods, citrate-nitrate combustion) and sintering aids added to the mixture (such as CuO, NiO, ZnO)[13], which can diminish the sintering temperatures by 100-400 °C.

Y-doped barium zirconate materials exhibit mixed ionic-electronic conductivity under oxidising conditions, with a contribution from *p*-type carriers larger than that observed in $BaCeO_3$-based systems; an optimised concentration of dopant can, though, limit hole transport in the material. Studies on the influence of the A-site cation have shown that among zirconates, Ba-containing ones display higher conductivities and smaller activation energies than their Ca- and Sr- homologues, a fact that can be associated to the lowering of symmetry in $SrZrO_3$ and $CaZrO_3$ (respectively $t = 0.947$, and $t = 0.914$, while for $BaZrO_3$ $t = 1.01$).

Since the discovery of solid-state reactive sintering, new fabrication methods[96], surface processing steps[97] and thin-film deposition techniques[98] have demonstrated the potential of BZY materials for the next generation of PCFC devices. Mixed cerate-zirconate systems are also very promising, as recent advances in cell fabrication techniques show improved performance and stability at 600 °C and indicate scalability of the process[26].

3.2.5 Titanates

With respect to cerate and zirconate systems, relatively few studies have focussed on the proton conduction properties of alkaline-earth titanate compounds. $BaTiO_3$-based solid solutions have been extensively studied, as a means to tailor their ferroelectric properties, the main characteristics of this kind of materials. $BaTiO_3$ exhibits various crystal habits at room temperature, depending on the thermal history of the compound during the synthesis, and the synthesis route itself. While for pure $BaTiO_3$ $t = 1.06$, substitution of rare-earths for Ti^{4+} and/or Ba^{2+} (depending on the size of the dopant) produces a decrease in the tolerance factor with increasing ionic size on the B-site, and the opposite for increasing size on the A-site[99].

The main investigations on titanate phases stem from ionic conduction studies of doped browmillerite $Ba_2In_2O_5$[100,101]. The progressive filling of the intrinsic oxygen vacancies of the parent phase when replacing Ti for In, induces disordering of the vacancy array and stabilise cubic perovskite structures at room temperature, for substitutions larger than 15 mol%. These compounds show better oxide ion conductivities than the parent brownmillerite and significant level of protonic conductivity[102]. In the series, $BaIn_{0.8}Ti_{0.2}O_{3-\delta}$ displays the highest proton conductivities, but also a phase transformation from cubic $Pm\bar{3}m$, to tetragonal *P4/mmm* upon hydration[102]. Higher doping levels (50

mol% and above) fully stabilise cubic structures, but show poorer levels of protonic conduction[103]. Reverse Monte Carlo analysis of total scattering data[53] indicates a combination of regular InO_6 and distorted TiO_6 octahedra, that disrupt the regularity of the oxygen sublattice.

The investigation of Sc-doped $BaTiO_3$ systems[14,15] produced interesting results, with heavily doped phases showing close to unitary proton transference number, below 500 °C in inert atmosphere and a significantly higher total conductivity in O_2 atmosphere, indicating *p*-type electronic contribution. In the series $BaTi_{1-x}Sc_xO_{3-\delta}$, Sc levels control the symmetry of the unit cell, promoting a transformation towards cubic $Pm\bar{3}m$ structures at substitution levels above 50 mol%. Despite the poor densification of the ceramic samples (below 90% of the theoretical value), $BaTi_{0.3}Sc_{0.7}O_{3-\delta}$ shows proton conductivities above 10^{-3} S/cm, indicating a promising outlook for this system[15].

3.3 Other significant classes of ceramic protonic conductors

3.3.1 Brownmillerites

This class of compounds could be described as a layered perovskite with intrinsic oxygen vacancies, $ABO_{2.5}\square_{0.5}$. In the most studied phase, $Ba_2In_2O_5$ (*fig.3.9*), which is orthorhombic at room temperature, the vacancies undergo an order-disorder transition at high temperature, pushing the system towards a tetragonal symmetry (around 930 °C), and finally to a cubic oxygen-deficient perovskite (at 1040 °C)[104]. This greatly enhances the oxide ion conductivity and is the drive for the number of studies done on this and related doped systems, whereas proton conduction was initially treated as a contamination problem and only then investigated in its own right. $Ba_2In_2O_5$ undergoes a reversible phase transformation under humid conditions that yields $Ba_2In_2O_4(OH)_2$[105,106]. Above the temperature at which the order-disorder transition occurs, this water incorporated phase becomes a good protonic conductor, in humid conditions, due to the sharp increase in the concentration of mobile vacancies[107]. As previously mentioned, the Ti-doped phase $BaIn_{0.8}Ti_{0.2}O_{3-\delta}$[102] is the most studied and successful at conducting protons. The higher electronegativity of Ti^{4+} implies a decrease in basicity with Ti content, hence, compositions with lower Ti content react more keenly with water vapour and stabilise the protonic defects without trapping them[102]. For the composition with 20 mol% Ti, total conductivity reaches 10^{-3} S/cm at 450 °C, in wet N_2[102]. As for cerate systems, higher basicity means poorer stability towards carbonation that improves with Ti content.

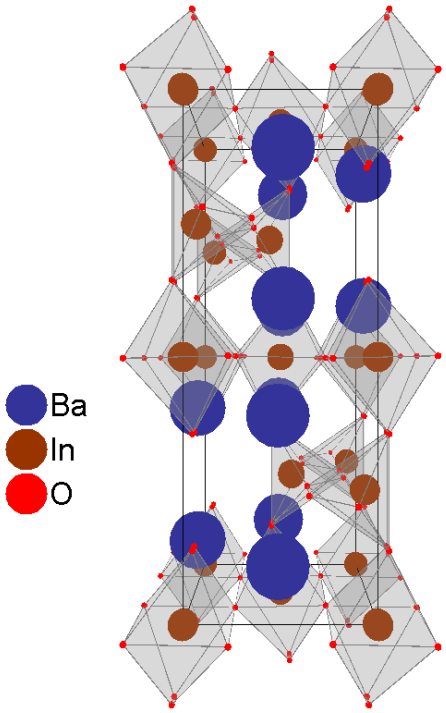

Fig. 3.9 Representation of the crystal structure of the brownmillerite $Ba_2In_2O_5$.

3.3.2 Phosphates, niobates, tantalates

Materials based on rare-earth cations on the A-site, generally indicated with the formula $LnBO_4$, attracted interest as potential high-temperature proton and mixed proton-electron conductors, because of their lower basicity with respect to alkaline-earth based materials. Rare-earth phosphates were the first reported to show significant level of proton conductivity, in Sr-doped $LaPO_4$[108]. Given the interesting proton conductivities among ortho-phosphates, the analogous rare-earth ortho-niobates and ortho-tantalates came in focus, with Ca-doped $LaNbO_4$ exhibiting essentially pure proton conductivity under wet conditions below 850 °C, with conductivities in the order of 10^{-3} S/cm[71]. The 1:1 Ln:Nb/Ta phases rare-earth ortho-niobates and ortho-tantalates, $LnMO_4$, are temperature-depending polymorphs. The monoclinic low-temperature phase corresponds to the Fergusonite-type structure, whereas the high-temperature phase is tetragonal and corresponds to the Scheelite-type structure (*fig. 3.10*). The materials show mixed proton-electron conduction at high temperatures (above 800 °C) under oxidizing conditions, while, under reducing conditions, practically no electron conductivity was observed. As general trends, conductivity decreases from the larger towards the smaller rare-earth cation and its maximum is shifted to higher temperatures.

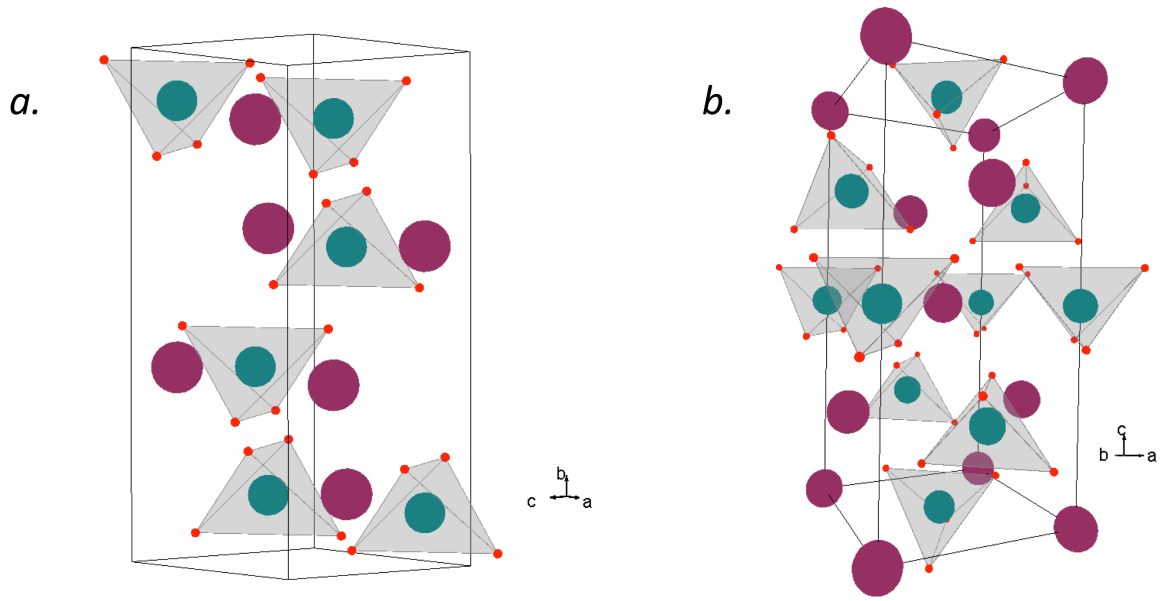

Fig. 3.10 Low-temperature, monoclinic Fergusonite-type structure (*a.*) and high-temperature, tetragonal Scheelite-type structure (*b.*) A-sites in purple are occupied by Ln^{3+} elements, B-sites in green are occupied by Nb, Ta. W-doped $LnNbO_{4+\delta}$ phases have been recently proposed as novel interstitial-based oxide ion conductors where, in the Scheelite-type phase, more than one interstitial site is potentially accessible[109].

3.3.3 Tungstates

This family of materials, depending on composition and conditions, are pure proton or mixed proton-electron conductors and may therefore have potential as electrolyte materials for proton-conducting solid oxide fuel cells or as dense membranes for H_2 separation. The structure of rare-earth tungstates, Ln_6WO_{12}, was described as an ordered defective fluorite, or as a disordered pyrochlore[110,111]. The structure changes along the Ln series: cubic or pseudocubic from La to Pr, *via* pseudo-tetragonal from Nd to Gd, to rhombohedral for the smaller rare-earth cations from Tb to Lu, and for Y_6WO_{12}. The description of lanthanum tungstate was later refined, revealing an average cubic fluorite-type structure with disordered inherent oxygen vacancies[112] (*fig. 3.11*). For Ln_6WO_{12} materials (with Ln = La, Nd, Gd, Er), ionic conductivity is dominated by protons under wet conditions, below 700 °C, and the maximum in proton conductivity decreases from $\approx 10^{-3}$ S/cm for La_6WO_{12}, to $\approx 10^{-4}$ S/cm for Er_6WO_{12}[73]. In general, the materials are mixed ionic-electronic conductors, where the ionic conductivity gradually decreases, to favour *n*- and *p*-type electronic conductivity, under reducing and oxidising conditions respectively, with decreasing size of the rare earth.

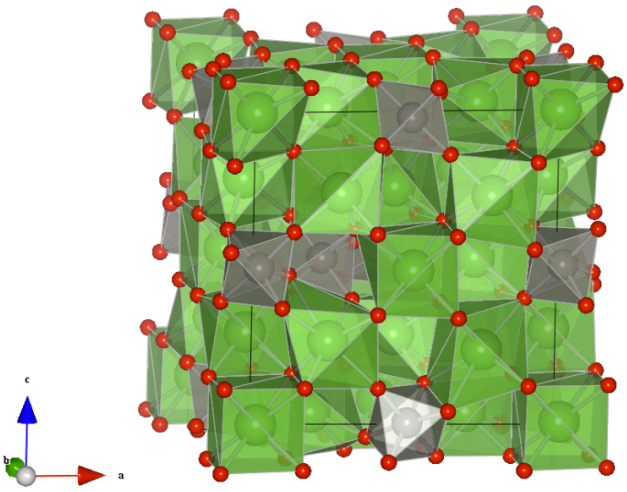

Fig. 3.11 Structure of lanthanum tungstate. La, in green, exhibits two different coordination environments, cubes and heavily distorted cubes, as a result of the intrinsic oxygen vacancies. W, in grey, forms WO_6 octahedra that tilt in various directions, showing disorder. Some W occupy the distorted cubic La sites to form a stable composition, and oxygen vacancies are filled up as a function of W content. The formula unit can be written as $La_{28-x}W_{4+x}O_{54+\delta}\square_{2-\delta}$ with $x \approx 1$[112].

3.3.4 Fluorite- and pyrochlore-related phases

Systems exhibiting the fluorite structure are known to be amongst the best oxide ion conductors; such in the case for acceptor-doped ZrO_2 and CeO_2. Modest proton transport was found in Gd-doped ceria[113] and, to a higher extent, in the system $La_2Ce_2O_7$[76]. In this latter, moderately favourable hydration thermodynamics combines with defects association that reduces the amount of charge carriers, invalidating the acceptor-doping strategy. Ce^{4+} is, in fact, easily reducible and while conferring poor electrochemical properties for an electrolyte, it gives good membrane separation properties to the material due to its mixed ionic-electronic conductive nature[16]. Empirical trends showed that the hydration enthalpy becomes more exothermic with more stable oxides, that is with smaller rare earths[60,114].

The pyrochlore structure, $A_2B_2O_7$, can be considered as an ordered anion deficient fluorite (*fig. 3.12*). A-site and B-site cations fill alternating crystal positions in a fcc lattice, while oxide ions fill seven of the eight tetrahedral interstices (the vacant one is highlighted in a paler shade of red). The larger A-site cations (≈ 1 Å) sit in (½, ½, ½) and are eight-fold coordinated whereas the smaller B-site cations (≈ 0.6-0.7 Å) coordinate six oxide ions and sit at the origin. Oxide ions are distributed over two different sites, *8a* (⅛, ⅛, ⅛) and *48f* (*x*, ⅛, ⅛), while *8b* (⅜, ⅜, ⅜) sites are intrinsically vacant. As a consequence, the one with higher multiplicity (*48f*) relax in the ⟨110⟩ direction towards the vacant site. A shift in its *x* coordinate gives a measure of the distortion of the coordination environment of A- and/or B-site cations. If the B cation is chosen as origin, when $x = 0.375$, A cations are located in a perfect cubic coordination; when $x = 0.4375$, B cations are in a perfect octahedral coordination[115].

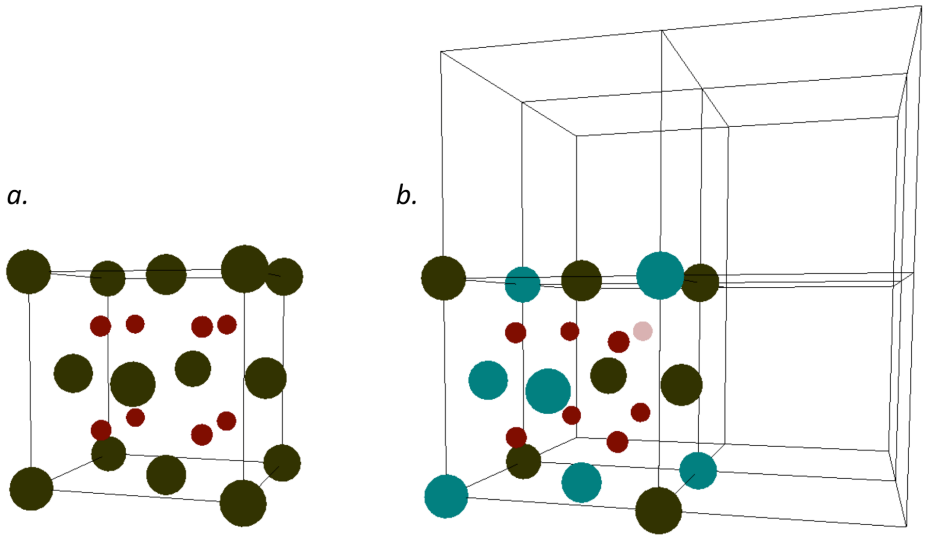

Fig. 3.12 The fluorite structure (*a.*) compared to the pyrochlore structure (*b.*), of which only one octant is shown for clarity. In binary oxides crystallising in the fluorite structure (space group $Fm\bar{3}m$) a face centred cubic (fcc) array of A cations, in green, describes the crystal lattice and oxide ions, in red, sit in the tetrahedral interstices. Pyrochlores crystallise in the $Fd\bar{3}m$ space group (a diamond glide plane along *a* replaces a mirror plane) and can be thought of as deriving from the fluorite structure.

Alternatively, it can be viewed as a network of BO_6 octahedra sharing vertices (*fig. 3.13*). This latter description reveals two distinct crystallographic sites for the oxide ions, one of which only interacts with the A cation and can accommodate a high level of vacancies. This, in turn, provides the ability for the structure to favour oxide ionic transport and protonic conductivity. Sr- and Ca-doped $La_2Zr_2O_7$ are the materials exhibiting the highest proton conductivity for this class (*ca.* 10^{-2} S/cm at 600 °C) with hole conduction becoming important at high temperatures and under oxidising conditions[116].

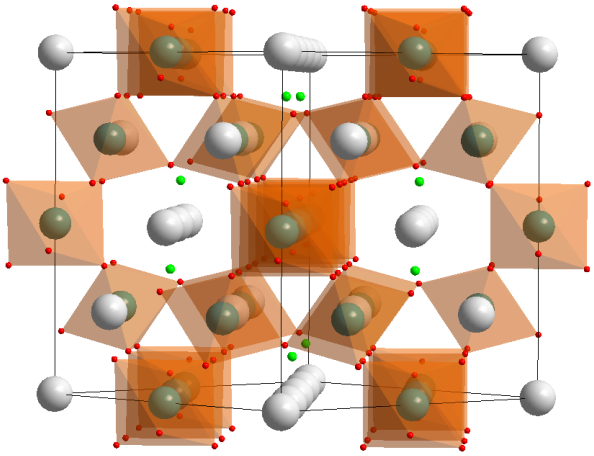

Fig. 3.13 The pyrochlore structure. BO_6 octahedra are highlighted in orange, A-site cations in grey, and non-polyhedral oxygens in bright green. In this representation, the interlinked rings of BO_6 octahedra form channels along the ⟨110⟩ crystal direction, where the A cations and the non-coordinated oxygens can be found.

3.4 On mixed protonic conduction, and H^- conductors

3.4.1 Mixed proton conductors

The conductivity of proton conducting phases is in reality more complicated than described in previous sections. Generally, acceptor-doped materials are not electronic insulators but weak *p*-type semiconductors. At high temperatures, in fact, a small amount of oxygen can react with the defective perovskite to partially fill the vacancies and generate a population of holes:

$$v_O^{\bullet\bullet} + \tfrac{1}{2}\, O_2 \longrightarrow O_O^{\times} + 2\, h^{\bullet} \qquad (3.7)$$

In addition, the presence of oxygen vacancies allows oxygen diffusion in the solid. This means that in wet conditions conductivity can involve three charge carriers (H^+, O^{2-}, and $h^\bullet$) or four, if electrons (e') are included. The contribution of each of these is strongly temperature-dependent. As an example, *figure 3.14* shows the variation of the transference number as a function of temperature for $SrZr_{1-x}Y_xO_{3-\delta}$. Protons dominate at lower temperatures, with proton transference number approaching unitary values; at intermediate temperatures, oxygen ion conductivity becomes dominant; at high temperatures, the material, depleted of protons, is mainly a hole conductor, where holes transference number approaches 1. Between these temperatures, at approximately 350 °C the solid is a mixed H^+ and O^{2-} conductor, while at approximately 650 °C it is a mixed hole and oxide ion conductor.

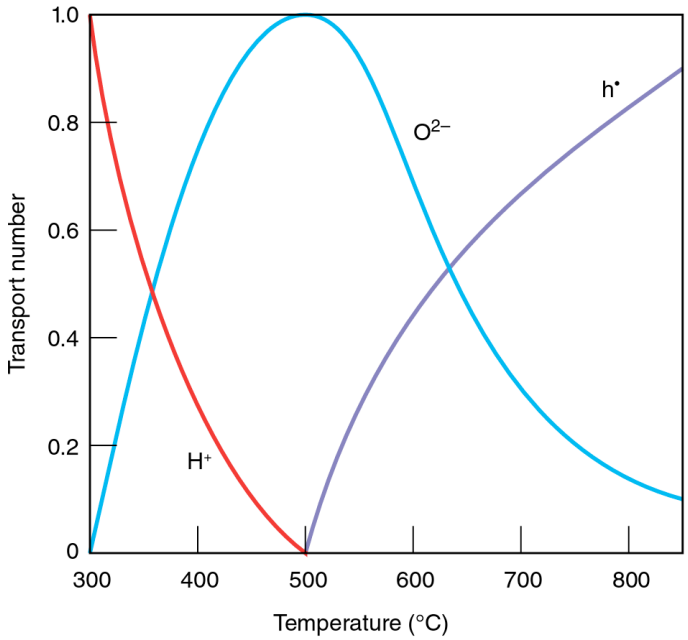

Fig. 3.14 The variation in transport number for proton, oxygen, and hole conductivity for the mixed proton conductor $SrZr_{1-x}Y_xO_{3-\delta}$[80].

3.4.2 Conductors of hydride ions

Along with the proton, hydrogen in ceramic materials can be a charge carrier also as hydride ion. In $BaTiO_{3-x}H_x$, H^- and O^{2-} ions form the octahedral environment around Ti and for the hydride ion two possible diffusional routes have been discussed: *a*) an oxygen vacancy assisted diffusion, and *b*) the transformation of the hydridic species into a protic one followed by interstitial diffusion to an empty lattice point and transformation back to hydride ion[117,118]. Differently than proton conduction, that takes place widely in oxides and other systems, H^- conduction has been verified only for a few hydrides of alkaline earth metals such as BaH_2[119]. Carrier mobility is, in fact, 1000 times greater for electrons than for much larger ions and the partial H^- conductivity can be easily hindered. Electronic conductivity must hence be suppressed in order to obtain a pure H^- conductor. Nonetheless, the existence of hydride ions has been speculated in proton conducting oxides[120], observed in the layered perovskite $LaSrCoO_3H_{0.7}$[121] and oxyhydride of $BaTiO_3$[117], and finally reported as the main charge carrier for the K_2NiF_4-type oxyhydride La_2LiHO_3[122]. This latter system features a cation sublattice whose ions have a sharper electron-donating character than H^- and an anion sublattice that can accommodate H^-, O^2, and vacancies.

Chapter 4
Experimental

4.1 Preparative methods

Ceramic materials can be prepared in a number of ways, all of them involving two main steps: the preparation of a mixture of precursors and one or more high-temperature treatments. The mixture of precursors can be obtained by dry or wet methods, each of them yielding a material with a different microstructural characteristic, mainly dealing with the size of the particles, or particles agglomerates.

4.1.1 Solid-state synthesis

A synthesis route in the solid state implies the homogenisation of a mixture of reactants by manually grinding the powders often using a mortar and pestle. The main goal of this operation is to break the original particles down to a size that improves the inter-diffusion of the reactants (by increasing the surface-to-volume ratio) when forming the desired phase during the heat treatments: the melt of the mixture is, in fact, not desirable and the reaction happens in the solid state. While the grinding step can be done with the assistance of machines (ball mills, planetary ball mills), manually grinding the powders can dramatically improve control over the system and avoid unwanted pollutants (attrition is a crucial factor). During the grinding process, homogenisation of the mixture can usually be enhanced by suspending the powders in a little amount of an inert liquid, such as ethanol, acetone, or other organic solvents, or water when possible, until dryness. Each suspending agent will produce a different result with respect to the agglomeration of the particles, because of its polar nature, its electrostatic interaction with the powder and the availability of hydrogen bonds. Once the mixture is prepared, it is transferred into a reaction vessel, made of an inert material (such as α-Al_2O_3, Pt) convenient to withstand the high temperatures involved in the reaction step, generally spanning from 800 °C to 2000 °C and more. The whole operation is, then, repeated until the desired phase is formed.

$BaTi_{1-x}Sc_xO_{3-\delta}$

Polycrystalline samples of the $BaTiO_3$-Sc_2O_3 solid solution (BTS) were synthesised by mixing dry, stoichiometric amounts of $BaCO_3$, TiO_2, and Sc_2O_3 and manually grinding the powders in an agate mortar with a pestle, with the addition of ethanol as suspending agent. Mixtures were pelletised, put into α-Al_2O_3 crucibles and annealed at high temperatures in box furnaces. Different compositions were attempted, of hexagonal and cubic structure types, and only four successfully synthesised, namely Sc-substituted

samples with x = ⅙, 0.2, 0.5, 0.7, respectively named BTS⅙, BTS20, BTS50 and BTS70. More details about the syntheses of BTS samples with x = 0.2, 0.5, 0.7 can be found in paper I[123], paper II[124], and section *5.2*. The sample with x = ⅙ was produced by annealing the mixture of reactants to room temperature from 1000 °C and, once pelletised, fired at 1200 °C for 24 h, at 1300 °C for 12 h, at 1350 °C for 24 h, at 1400 °C for 84 h with intermediate grinding and pelletising, at 1415 °C for 48 h, at 1425 °C for 60 h with intermediate grinding and pelletising steps.

Ruddlesden-Popper phases

Polycrystalline samples with the general formula $Ln_{1-x}AE_{1+x}MO_{4-\delta}$ (with Ln = La, Pr; AE = Mg, Ca, Sr, Ba; M = Sc, In) were synthesised by using stoichiometric amounts of La_2O_3, Pr_6O_{11}, MgO, $CaCO_3$, $SrCO_3$, $BaCO_3$, Sc_2O_3, In_2O_3. Dry reactants were mixed in a mortar with ethanol and/or acetone as suspending agent and annealed to room temperature from 1000 °C, in α-Al_2O_3 vessels. Powders were ground, pelletised and fired at 1100 °C for 12 h, at 1300 °C for 12 h, and at 1400 °C for 12 h.

Double perovskites

$Sr_2Mg(Mo_{1-x}Nb_x)O_{6-\delta}$ samples (with x = 0, 0.3, 0.5) were synthesised by using $SrCO_3$, MgO, MoO_3, and Nb_2O_5. Stoichiometric mixtures of dry reactants were ground in an agate mortar, suspended in ethanol to enhance homogenisation. The mixed powders were annealed to room temperature from 900 °C, then ground and pelletised. Uniaxially pressed pellets were fired at 1100 °C for 12 h and at 1500 °C for 96 h with intermediate grinding and pelletising steps. Syntheses were carried out in Pt vessels.

Pyrochlores

All samples were produced by mixing in ethanol stoichiometric amounts of desiccated reactants: oxides TiO_2, MoO_2, HfO_2, Y_2O_3, Gd_2O_3, Yb_2O_3, La_2O_3, Ga_2O_3, Sc_2O_3, Sm_2O_3, MgO; and carbonates $CaCO_3$, $SrCO_3$. Ti- and Hf-based systems were annealed in box or tube furnaces in air, while the Mo-based ones were annealed in tube furnaces with controlled atmosphere of Ar or 5% H_2 in Ar in order to prevent MoO_3 volatilisation. The synthesis of Ti-based pyrochlores consisted in few heating steps of 10 hours each at 1400 °C. Mo- and Hf-based systems required different attempts and temperature programmes (up to 1600 °C). Syntheses were carried out in α-Al_2O_3 vessels.

4.1.2 Pechini method

This method, introduced by M. P. Pechini in 1967 (patent US3330697 A[125]), is an easy and convenient way for the preparation of a variety of advanced ceramics. It involves the mixing of a solution of metal nitrates, oxychlorides, or oxides, with one of citric acid (or other polyacid) and an excess of a polyhydroxyl alcohol (such as ethylene glycol, or polyethylene glycol) in order to obtain a mixture of precursors. The scope of using citric acid is double: being a chelate agent, it complexes the metallic ions and it serves as polyacid for the formation of a polymeric reticulate network *via* polyesterification with the polyhydroxy alcohol. This polyester net reduces any segregation of the metallic cations and helps creating a homogeneous dispersion of the species that will form the desired phase, yielding an intimate mixing (at atomic level) that drastically reduces the

calcination temperature. Once the resin formed, in fact, the solution is evaporated to dryness and the solid decomposed and calcined, with intermediate grinding steps, until the intended compound is formed. The ratio between the concentration of chelating agent and that of the cations, as well as the pH, controlling the degree of protonation of the carboxylic and hydroxyl species, are important parameters influencing the microstructure of the final product. Modifications of the method itself yield different results with respect to the microstructure of the product[126] but, in general, through wet methods it is possible to obtain submicro- and nanosized powders[127].

$BaTi_{1-x}Sc_xO_{3-\delta}$

Stoichiometric amounts of Ba and Sc acetates were dissolved in ethylene glycol at 80 °C to prepare the solutions of the two metals. Ti butoxide solutions were prepared in a glovebox under N_2 atmosphere, by dissolving the stoichiometric amounts in dry ethanol while vigorously stirring. The Ba and Sc solutions were added to the Ti ones, while blowing N_2 on the surface to prevent any hydrolysis product. Traces of glacial acetic acid were added to catalyse the esterification and promote the gelation. After 24h of aging, the gels were dried on a hot plate and the xerogels calcined at 800 °C for 5h. Following synthesis steps are described in chapter 5, section *2.2*.

$BaZr_{0.8}M_{0.2}O_{3-\delta}$ (with M = Sc, Ga, Y, In, Yb)

Stoichiometric amounts of $Ba(NO_3)_2$ and $Zr(acac)_4$ were dissolved in a hot solution of ethylene glycol and ethanol, along with the nitrate salt of the metallic cation and monohydrated citric acid, so to have a total metal to citric acid ratio of 1.83. The solution was heated to 180 °C and gelated overnight. The gel was then dried at 300 °C and the products (burnt dark brown masses) collected and slowly (0.5 °C/min) calcined to 900 °C. The powders, now white, were uniaxially pressed into pellets and annealed, embedded in sacrificial powder in α-Al_2O_3 crucibles, in a box furnace. Samples were retrieved, the sacrificial powder sieved away and the pellets intensively ground and repelletised to be fired at 1100 °C for 24 h, at 1200 °C for 24 h, at 1300 °C for 24 h, at 1400 °C for 12 h and at 1500 °C for 12 h.

4.1.3 Vacuum drying

During the cooling down step of the syntheses, samples tend to incorporate water from the atmospheric moisture into their structure. These undesired proton defects are removed, prior to a controlled hydration step, by vacuum drying the samples in a tube furnace. The samples are placed into alumina boats and inside a quartz tube then connected to a turbomolecular pump and annealed at high temperature (500 to 1000 °C) under a pressure of *ca.* 10^{-6} mbar, for not less than 12h.

4.1.4 Hydration

A hydration experiment is employed in order to introduce protonic defects into the structure of the material under investigation, as illustrated by *equilibrium 2.1*. The hydration treatment is carried out in a tube furnace through which nitrogen passes, after bubbling through a round bottom flask filled with distilled water, or heavy water, D_2O.

The partial pressure of water, $p\mathrm{H_2O}$, is controlled by heating up the water in the round bottom flask. The temperature of the water is kept at 60 °C, providing a $p\mathrm{H_2O}$ of *ca*. 0.2 atm, for the whole duration of the experiments.

▻ BTS samples were exposed to gradually diminishing temperatures, from 400 °C, to 300 °C, to 200 °C, each for 1h of isothermal residence time, to finally 185 °C for 2 to 5 days.

▻ Barium zirconate samples were hydrated in an autoclave at 260 °C.

▻ Ruddlesden-Popper phases underwent two different hydration experiments. The successfully synthesised phases were first exposed to humid atmosphere in order to probe their stability. In a tube furnace temperature was risen to 800 °C and kept for 15 minutes, then allowed to cool down to 200 °C before retrieving the samples (procedure referred to as *HYD1*). The phases that were left unaltered by this treatment underwent a hydration step, in the same furnace, at 200 °C for 6 h (*HYD2*). Samples were retrieved at 200 °C.

Prior to the experiment, a thermogravimetric analysis of hydrated or as-prepared samples gives crucial information about the hydration behaviour of the compound, in order to set the right temperature programme for a successful hydration.

4.2 Characterisation techniques

4.2.1 Diffraction techniques

Crystal structure analysis is usually based on the scattering phenomena caused by the interaction of matter with a beam of radiation or particles, such as X-rays and neutrons. When the wavelength of the beam is comparable to the spacing of a periodic array of atoms, an interference pattern of the scattered waves can be observed. In 1912, W. L. Bragg described a simple method for obtaining the conditions for diffraction, as the consequence of the simultaneous scattering of an X-ray beam by the lattice planes belonging to the same family. The conditions for observing the maximum positive interference at the angle ϑ are satisfied when a multiple of the wavelength λ equals the difference in the path (AB+BC) between the waves scattered in D and B (*fig. 4.1*), according to the well-known Bragg's law:

$$2d_{hkl}\, sin\vartheta = n\lambda \qquad (4.1)$$

The scattering angle ϑ, known as Bragg angle, is the angle between the primary beam and the family of lattice planes *hkl*, with *d* being the spacing between two planes of the same family. This relationship was discovered while performing diffraction experiments with X-rays and it is verified also in the case of neutrons and electrons beams. Scattering phenomena can either be *elastic* or *inelastic*, whether the scattered beam emerges with the same wavelength as the incident one, or not. This implies that energy can be lost during a scattering event, that is, it can be transferred to the scattering centre. The

diffraction techniques here described rely on elastic interactions of the beam with the system under investigation, and inelastic scattering events are not considered.

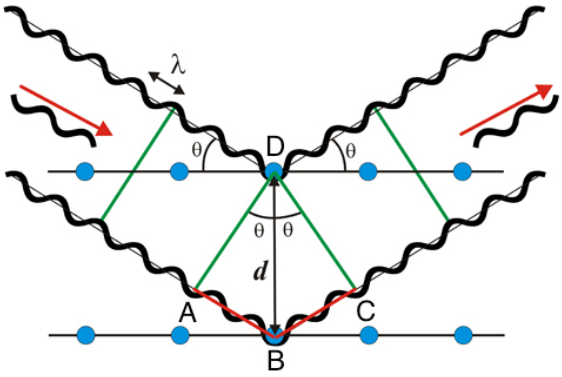

Fig. 4.1 Scattering of X-rays from two lattice planes belonging to the family *hkl*; *d* is the interplanar spacing.

4.2.1.1 X-ray powder diffraction

Powder X-ray diffraction (XRD) is probably the most common physical method in solid-state inorganic chemistry, used to perform phase analysis and assessments of phase purity, to calculate the size of a samples' crystallites, and to determine crystal structure. While single crystal X-ray diffraction techniques have provided the main information to start interpreting powder data, nowadays polycrystalline samples (*i.e.* powders) can also be used for structural characterisation thanks to the advances in instrumentation and, most importantly, to the work of H. M. Rietveld who introduced the Rietveld analysis method[128], discussed in a following paragraph.

A crystalline powder contains a large number of small crystallites randomly oriented, so that a part of those can meet Bragg's condition when performing a diffraction experiment. Diffracted intensities are plotted against the scattering angle, in order to produce a diffraction pattern from the analysis of which structural information can be obtained. Although peak indexing can become difficult, due to systematic absences, and to peak overlapping when dealing with structures of low symmetry, XRD is still a powerful technique, thanks to the vast and continuously growing library of powder diffraction patterns constituting the JCPDS-ICDD database (Joint Committee for Powder Diffraction Standards - International Centre for Diffraction Data), against which an experimental pattern can be matched by means of a software.

The interaction between X-rays and a crystalline sample involves the electrons in the crystal, therefore heavier elements (*i.e.* atoms with a high number of electrons) scatter X-rays more strongly than lighter ones and isoelectronic species cannot be distinguished, thus making structure determination more difficult, if possible at all. The ability of an atom to scatter X-rays, the *scattering factor*, is also influenced by the scattering angle, and intensities diminish with increasing angles.

X-ray diffractometer

Laboratory X-ray powder diffraction analyses were performed mainly on a Bruker AXS D8 Advance diffractometer. This instrument mounts a sealed-tube X-ray generator with a copper target, providing Cu K radiation from which the $K\alpha_1$ component (λ = 1.54056 Å) is selected with a Ge (111) crystal monochromator. The sample plate is mounted on a goniometer with Bragg-Brentano ϑ-2ϑ configuration and the information carried by the diffracted beam is collected with a solid-state LynxEye detector. Alternatively, experiments were carried out with a Siemens D5000 Kristalloflex Bragg-Brentano ϑ-2ϑ diffractometer mounting a scintillation detector and using a Cu radiation ($K\alpha_1$ and $K\alpha_2$). Phase analysis is carried out by profile matching against the ICDD database with the Bruker AXS DIFFRACplus EVA software.

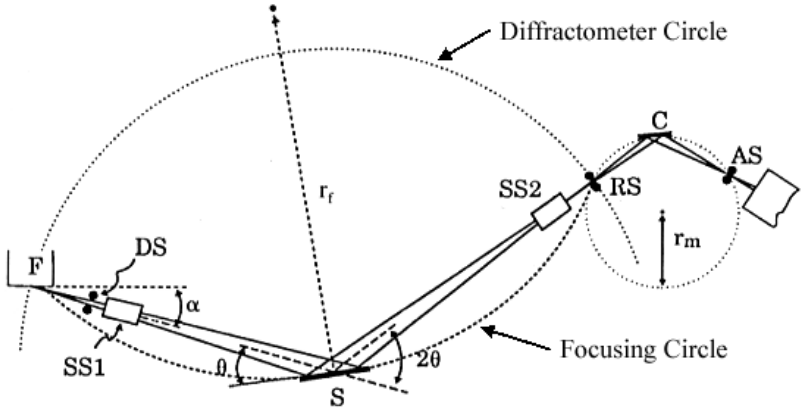

Fig. 4.2 A schematic of a X-ray powder diffractometer with Bragg-Brentano geometry. In such a geometry, the X-ray source (F), the sample (S) and the receiving aperture (RS) all fall on a circle of radius r_f. The divergence aperture (DS) and divergence Søller slit (SS1) illuminate the sample with a diverging beam of X-rays; these X-rays are subsequently focused back to the receiving aperture on the focusing circle. The focusing circle radius, r_f, is not constant. It is a function of the Bragg angle, ϑ, and the diffractometer radius, R: $r_f = R/(2\sin\vartheta)$.

Synchrotron X-ray diffractometer

A special kind of X radiation is generated at large facilities hosting a synchrotron ring. In these installations, charged particles (electrons or positrons), accelerated to relativistic velocities, emit electromagnetic radiation in the X-ray range. This radiation is characterised by a very intense photon flux (10^{13}-10^{23} photons s^{-1} mm^{-2} $mrad^{-2}$, against the 10^7-10^9 available with a laboratory diffractometer), a highly-collimated beam (divergence in the order of mrads and less), and the possibility to select the wavelength (generally in the interval 0.1-2.5 Å, depending on the synchrotron design and on the specific beamline optics). The diffraction experiments were carried out at the European Synchrotron Radiation Facility (ESRF) in Grenoble, France, on the ID22 high resolution X-ray powder diffraction beamline. The beam, monochromated by a Si (111) crystal, had a wavelength of 0.35477 Å and hit the samples enclosed in 0.2-0.3 mm diameter Lindemann glass capillaries.

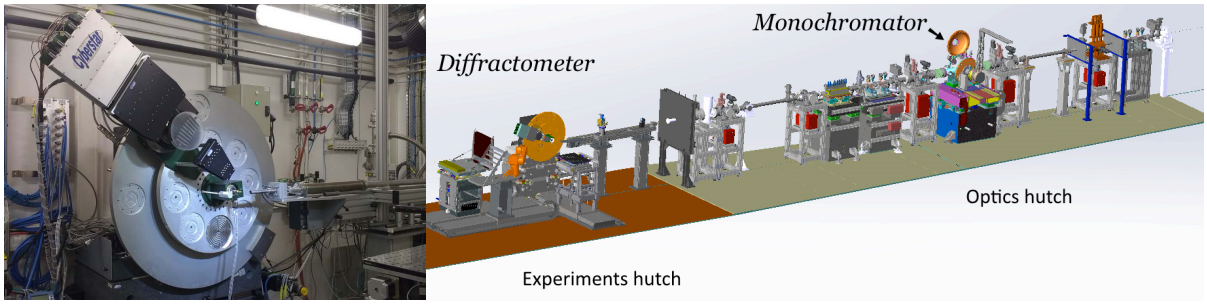

Fig. 4.3 The ID22 high resolution X-ray powder diffractometer (*left*) and the outline of optics and experiments hutches of its beamline (*right*).

4.2.1.2 Neutron powder diffraction

The main difference between neutron and X-rays arise from the scattering process: neutrons are scattered by atomic nuclei. For this reason, scattering factors do not decrease with the scattering angle and are constant, but vary randomly for different atomic species and different isotopes[129] (*fig. 4.4*). These features allow precise structural studies when heavy elements and lighter elements are present in a crystal, and will give more accurate distances, whereas for X-rays the distortion of the electron cloud is a source of error. On the other hand, the relatively low fluxes available at neutron facilities require larger samples for the experiments. Neutrons are produced in two different ways: as a result of atomic fission processes in a reactor, or by hitting a metallic target with protons, in a spallation process[129]. Each technique allowed the development of different instruments, employing a constant wavelength in the first case, or a broader spectrum in time-of-flight instruments at spallation sources, discussed in more details the following paragraphs. The properties of neutrons make this technique especially valuable when investigating the location of protons in a structure, especially when hydrogen atoms are in the presence of heavy metallic species, as in ceramic protonic conductors.

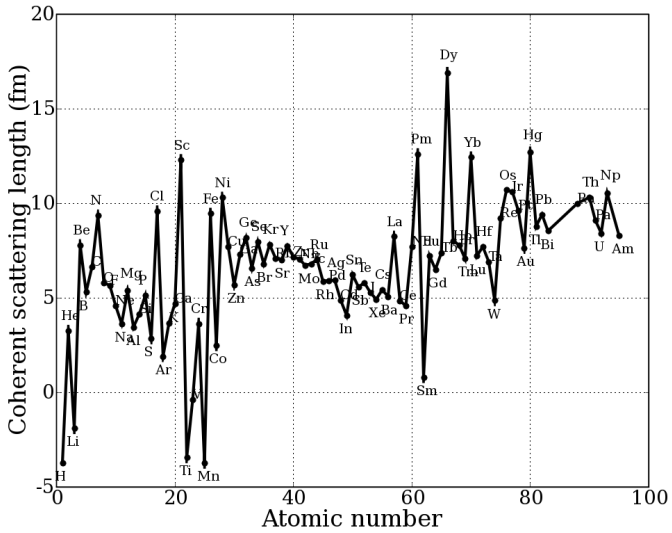

Fig. 4.4 Neutron coherent scattering lengths as a function of the atomic number. *Note*: incoherent scattering processes happen as well but do not yield any structural information and are seen as background signal. Those processes are not considered in the present studies and won't be discussed any further.

The D2B neutron diffractometer

Constant wavelength neutron powder diffraction experiments were performed at the Institut Laue-Langevin (ILL) in Grenoble, France. The ILL hosts a 58 MW research reactor that produces the most intense continuous neutron flux available nowadays, namely 1.5×10^{15} neutrons s^{-1} cm^{-2}. The high-energy neutrons produced by the fission reaction are slowed down by heavy water, D_2O, to the so-called *thermal neutrons*: these are the kind of neutrons generally used in diffraction experiments. The neutron beam, once guided and collimated towards the instrument, was monochromated by a Ge (335) diffracting plane, providing a 1.594 Å wavelength. Diffracted neutrons are detected by a bank of 128 position sensitive ^{3}He tubes, in a semi-circular arrangement, opportunely moving during the experiment in order to cover a 2ϑ range up to 160°.

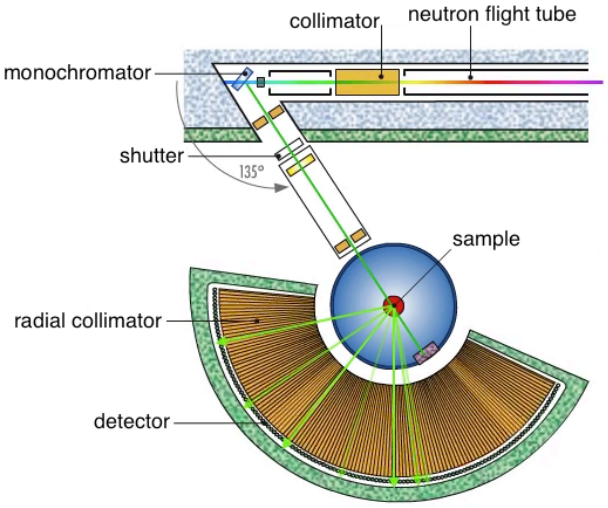

Fig. 4.5 Layout of the constant wavelength neutron diffractometer D2B.

The Polaris neutron diffractometer

As previously mentioned, neutrons can be produced also in a time-structured way, in a spallation source. Spallation is a chaotic process where, from an accelerated particle hitting the nucleus of an element with high atomic number, a series of subatomic particles are produced. The accelerated particles are produced in bunches in a synchrotron ring, which gives the neutron beam its pulsed nature. The diffraction geometry at pulsed neutron sources is generally based on time-of-flight (ToF) techniques. Here, the diffraction angle is fixed by the position of the detectors and the arrival time of each neutron in the pulse is measured. The detection time of each neutron, t_{hkl} (μs), can be obtained from Bragg's law (*equation 4.1*) with opportune modifications:

$$d_{hkl} = \frac{\lambda}{2\,sin\vartheta} = \frac{h}{m\,v}\frac{1}{2\,sin\vartheta} = \frac{h\,t_{hkl}}{m\,L}\frac{1}{2\,sin\vartheta} \qquad (4.2)$$

where h is Plank's constant, m is the mass of the neutron and v its velocity, and L is the distance between source and detector.

An important advantage of ToF techniques is the efficient utilization of most neutrons present in the incident beam, which allows shorter acquisition time. These methods are advantageous especially when following structural changes that evolve as a function of time, temperature, or pressure, since the bank of counters remains stationary and a whole diffraction pattern can be collected simultaneously. ToF neutron powder diffraction experiments were performed at the Intense Spallation Isotope Source (ISIS), part of the Rutherford Appleton Laboratory (RAL) in Harwell, UK. Bunches of protons, accelerated in a synchrotron, hit a tungsten target, producing 15 neutrons per proton collision and about 20 million every second. Polaris features a vacuum vessel of about 20 m^3, which mounts detector banks, with ZnS scintillators and ^{3}He tubes, distributed around the sample in a radial configuration.

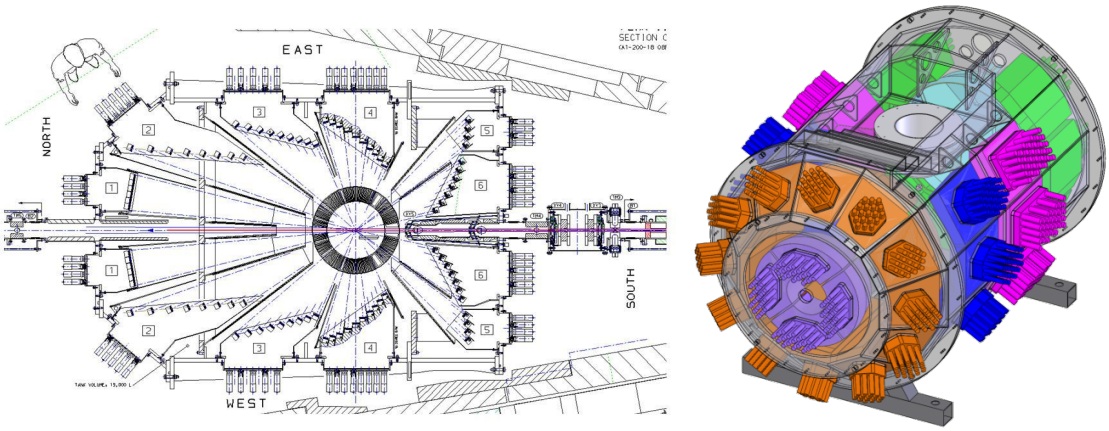

Fig. 4.6 Schematic drawings of the time-of-flight neutron diffractometer Polaris, showing the layout (*left*) and the detector modules (*right*) situated through the walls of the vessel to provide a large solid angle of detector coverage.

In situ characterisation techniques

The challenges that originate from the need of a deeper understanding of proton transport in proton conducting materials can be addressed by running multiple characterisation during one single experiment, while trying to mimic operative conditions. In such way, it is possible to observe a process in a more comprehensive manner than what is offered by *ex situ* characterisation approaches and therefore gain a unique set of information that can crucially complement the existing knowledge in explaining the structure-to-properties relationship and provide new insight for enhanced material design. In this spirit, the dehydration behaviour of perovskite structured proton conductors was probed with a combination of thermogravimetry and neutron thermodiffractometry. The experiment was performed at the ISIS Neutron and Muon Source in Harwell (UK), using the Intelligent Gravimetric Analyser for Neutrons (IGA^n, Hiden Isochema). The equipment consists of a steel case hosting a spring balance (with a sensitivity of 0.1 μg) from which the samples is hanging in a vanadium cylindrical holder heated up by two resistive coils situated above and below it, that is loaded into the vessel of Polaris. *Fig. 4.7* shows a depiction of the experimental setup.

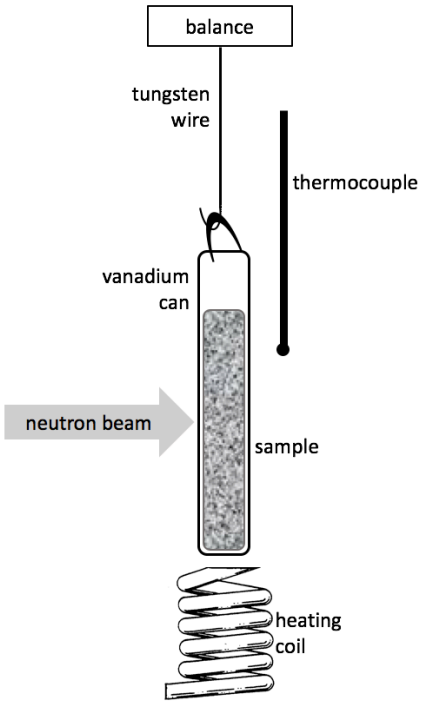

Fig. 4.7 Representation of the experimental setup of the IGA^n (Intelligent Gravimetric Analyser for neutrons). For clarity, the heating element above the sample is not shown.

4.2.1.3 Total scattering as a probe for local ordering

The structure determined by the scattering techniques previously described (X-ray and neutron diffraction) represents an average picture of the crystal structure of a material. When there are competing forces at the atomic level, such as those arising from the size mismatch in doped perovskites, the structure reflects the conflict, for example, by introducing a distortion that could locally (from less than 1 nm to a few nanometres) lower the overall symmetry of the unit cell[130,131]. The structure of complex materials can, therefore, deviate from the perfect crystal structure that arises from the interpretation of Bragg peaks as crystallographic methods *a priori* assume prefect lattice periodicity. In the case of well-ordered crystals, the average structure also reveals the local structure (although, *stricto sensu*, even a perfect crystal is not truly periodic because of quantum-mechanical and thermal vibrations: if a snapshot of the structure is taken, the crystal symmetry, including the translational one, is gone)[131]. When local distortions are present, the local structure must be studied directly in combination with the average structure since large aperiodic local atom displacements usually have repercussions on displayed properties, even when the average symmetry is unaltered. This understanding can direct the enhancement of a material or the creation of new ones with better properties.

The relative atomic positions can be described by using a set of interatomic distances, $r_{\nu\mu}$, with ν and μ referring to the individual atoms. In the case of an isotropic system, the distribution of interatomic distances in one dimension is given by:

$$\rho(r) = \rho_0 g(r) = \frac{1}{4\pi N r^2} \sum_{\nu} \sum_{\mu} \delta(r - r_{\nu\mu}) \tag{4.3}$$

where ρ_0 is the number density of atoms in the system of N atoms, and δ is the Dirac delta function. The function $\rho(r)$ is called *atomic pair density function*, and $g(r)$ the *atomic pair distribution function* (PDF). The PDF is a one-dimensional function with peaks at distances $r_{\nu\mu} = |\mathbf{r}_\nu - \mathbf{r}_\mu|$, separating the ν-th and μ-th atoms. The result is a histogram of all atom-atom distances in the solid. With the sums taken over all atoms in a sample, $\rho(r)$ becomes a quasicontinuos distribution function that drops to zero below a certain value of r because two atoms cannot come too close to each other. Since what is measured are deviations from the average density, $\rho(r)$ and $g(r)$ are referred to as *pair correlation functions*: they give information about correlations (deviations from average behaviour) of pair of atoms. These functions concern the local environment of atoms and valuable information can be extracted, such as how many neighbours there are and how far they are situated. Analogously, a three-dimensional model can be obtained and used to describe the experimental PDF. The PDF can be experimentally determined by diffraction measurements using X-rays, neutrons, or electrons[131].

This method is applicable to any system, whether amorphous or crystalline, isotropic or anisotropic, and polycrystalline or single crystal samples, although only recently it has become an established technique in the field of structural study of crystalline solids. This is due to two main reasons: *a*) the advent of synchrotron radiation sources and pulsed spallation sources; *b*) the availability of cheap high-speed computing[131]. The name *total scattering* derives from the inclusion, in the intensity, of scattering arising from Bragg peaks (the average structure), elastic diffuse scattering (the static local structure), and inelastic diffuse scattering from moving atoms that contains information about atom dynamics. All these are measured over a wide range of Q so that as much coherent scattering as possible is collected.

4.2.2 Rietveld analysis

The basic idea behind the Rietveld method is to calculate the powder diffraction pattern using a series of parameters and to refine and improve those parameters by minimising the weighted sum of the squared difference between the observed and the calculated powder pattern using a least squares method. Devised by Hugo M. Rietveld during the 1960s[128], the method became increasingly popular thanks to the advances in the field of computer and information technology: nowadays Rietveld analysis is an invaluable tool for the determination of crystal structure from polycrystalline samples.

The method requires the input of a model, against which least squares refinements are carried out until a best fit is obtained. The *best fit* is the best least squares fit to all the observed intensities simultaneously. The residual to be minimised, S_y, is given by:

$$S_y = \sum_i w_i (y_{i_{obs}} - y_{i_{calc}})^2 \tag{4.4}$$

where w_i is the weight of the i-th observable ($1/y_i$) while $y_{i\,obs}$ and $y_{i\,calc}$ are the observed and calculated intensities at the i-th step, respectively.

A powder diffraction pattern can be imagined as a collection of individual scattering profiles, each having a peak height, position, breadth, decay tails, and an integrated area proportional to the Bragg intensity I_K, where K represents the Miller indices hkl. I_K is proportional to $|F_K|^2$, the square of the absolute value of the structure factor. Calculated intensities are determined from the structure factor calculated from the structural model by summing the calculated contributions from neighbouring Bragg peaks plus a background term:

$$y_{i_{calc}} = s \sum_K L_K |F_K|^2 \varphi(2\vartheta_i - 2\vartheta_K) P_K A + y_{i_{bkgd}} \tag{4.5}$$

where s is the scale factor, L_K combines the Lorentz, polarisation and multiplicity factors, φ is the profile function that describes the peak shape, P_K is the preferred orientation function, A is an absorption factor, and $y_{i\,bkgd}$ is the background intensity at the i-th step. The peak shape is modelled by a function that approximates instrumental and sample effects. The most widely used for X-ray and constant wavelength neutron data is a linear combination of Lorentizan and Gaussian components, called *pseudo-Voigt*. Usually the background is modelled using one of the functions supplied with the software for Rietveld analysis, for example a linear combination of a number of polynomials with refinable coefficients.

It is important to note that the method does not resolve a structure but contributes to its solution by the refinement of parameters of an initial input model. Chemical knowledge and intuition are therefore equally important, if not at the basis of the whole process of structure solution. The parameters being refined include lattice constants, background, peak profile, atomic positional and thermal parameters. The precision of the structural model, fitted against the experimental data, is evaluated by a commonly used series of reliability factors, R.

The *weighted profile factor*, R_{wp}, contains the residuals to be minimised at its numerator:

$$R_{wp} = \sqrt{\frac{\sum_i w_i (y_{i_{obs}} - y_{i_{calc}})^2}{\sum_i w_i \, y_{i_{obs}}^2}} \tag{4.6}$$

The *Bragg R factor*, R_{Bragg}, contains the Bragg intensities:

$$R_{Bragg} = \frac{\sum_K \left| I_{K_{obs}} - I_{K_{calc}} \right|}{\sum_K I_{K_{obs}}} \tag{4.7}$$

The *structure R factor*, R_{F^2}, based on the observed and computed structure factors:

$$R_{F^2} = \frac{\sum_K {F^2}_{K_{obs}} - {F^2}_{K_{calc}}}{\sum_K {F^2}_{K_{obs}}} \tag{4.8}$$

Practically Rietveld analyses were carried out by using the software package GSAS[132] mounting the EXPGUI[133] interface, or the software Topas v5[134].

In a Rietveld refinement, a mathematical model is assumed to describe the experimental pattern, so that the intensity y_i observed at the *i*-th step can be compared to the corresponding one calculated *via* the model. If only a partial structural model is available, the calculated intensities may deviate significantly form the observed ones, complicating the initial refinement of profile parameters. In such case, a structure-free approach can be preferred in order to obtain initial values. With this approach, referred to as Le Bail refinement[135], calculated intensities are adjusted to fit the observed ones in an extraction without structural model.

4.2.3 Reverse Monte Carlo analysis

The correlation function (PDF) can be used as the input for a procedure similar to the Rietveld refinement, in which a structural model making use of different parameters is adjusted in order to minimise the difference between experimental and calculated PDFs. The structural model so obtained gives emphasis to the local structure, making it complementary to the Rietveld method. In the case of solid solutions, as in many other, techniques that are anchored to crystallographic descriptions of a structure are limited when describing local disorder. The Reverse Monte Carlo (RMC) is a method that removes symmetry constrains and incorporates both local and average structural information in a single model. This is attained by generating a virtual box containing a large number of atoms (tens of thousand), calculating the total scattering functions, comparing those with experimental data, and adjusting atomic positions to improve the agreement. The technique originates from X-ray and/or neutron scattering studies of liquids and amorphous materials, for which unit cells as repetitive units do not exist and which description relies on a model containing large ensembles of atoms. As engineered materials become more complex, models obtained by means of RMC analysis of total scattering data provides useful insight over different length scales and, most importantly, into the relationship between average and local structures.

4.2.4 Thermogravimetry

A thermogravimetric (TG) analysis is utilised to monitor and measure the change in mass of a sample as a function of a temperature programme, therefore as a function of temperature or time. This technique is often employed in the study of proton conducting materials as a mean for assessing the success of the hydration reaction (*equilibrium 2.1*) by measuring the water content of the sample, that is the degree of hydration of its oxygen vacancies. TG is also used to determine the crystallisation water content of the precursor salts for wet chemical synthesis routes. TG data were collected with a Netzsch STA 409 PC Luxx, using α-Al_2O_3 pans for the samples, referenced against an empty pan. Analyses were carried out under a flow of 20 ml/min of nitrogen or argon (AirLiquide Alphagaz 1), and heating rates varying from 5 to 20 °C/min, usually up to 1000 °C. Each set of analyses was proceeded by a blank run, under the same conditions, to be used as correction to the actual dataset.

4.2.5 Electrochemical Impedance Spectroscopy

Electrochemical Impedance Spectroscopy is a technique based on the characterisation of a sample's response to an alternating potential of variable frequency. The electric impedance of a system represents the ratio between the applied sinusoidal voltage and the resulting electrical current. Through the impedance, the resistivity of a material can be determined by modelling the physicochemical processes occurring while applying the tension, by means of an appropriate equivalent electrical circuit. In the ideal case of a polycrystalline homogeneous sample, which relative density equals the theoretical one, or a monocrystalline solid, perfectly in contact with the electrodes, the sample itself can be described as a resistor in parallel with a capacitor.

Conductivity is defined by:

$$\sigma = \frac{l}{R\,S} \tag{4.9}$$

where l is the thickness of the sample, S is the surface area of the electrode, R the resistivity. Given the Arrhenius law

$$\sigma = {}^{\sigma_0}/_{T}\ e^{-\Delta E/N_A k_B T} \Rightarrow \log(\sigma T) = \log \sigma_0 - \frac{\Delta E}{2.3 \cdot 1000 \cdot N_A \cdot k_B} \cdot \frac{1000}{T} \tag{4.10}$$

by plotting log (σT) versus 1000/T, macroscopic data about the sample can be obtained, such as the activation energy of the proton jump.

The impedance of the $La_{1-x}Sr_{1+x}ScO_{4-\delta}$ solid solution (Ruddlesden-Popper phases) was measured by means of a Solartron 1260 frequency response analyser connected to a ProboStat (NorECs, Norway). Few mm thick discs were sintered with the aid of a polymeric binder, attaining *ca*. 70% of the theoretical density, and Pt electrodes prepared on both faces. Measurements were performed in air and under controlled atmosphere, dry and wet Ar, over the frequency range 1 MHz to 100 mHz with an applied sine wave amplitude of 1 V.

4.2.6 Scanning Electron Microscopy

The Scanning Electron Microscope (SEM) generates a picture by moving an electron beam across the surface of a sample and detecting either the backscattered or, more commonly, the secondary electrons coming from the sample. Using secondary electrons, that have relatively low energies in the range of a few eV, has the advantage to give a very good image of the surface topography of the sample, since only secondary electrons from very near the sample surface can escape and reach the detector. An SEM consists of four main components: an electron gun, a system of magnetic lenses, the sample holder and a detector. Electrons are accelerated in an electric field and concentrated into a defined beam by the magnetic lenses. The sample needs to be conductive, since the bombardment with high energy electrons depletes electrons from the surface, thus creating a positive charge surplus that needs to be extinguished. Nonconductive samples need to be covered with a conductive material and gold is often used for this purpose. The two most important detectors are a detector for the secondary electrons, and one for the

backscattered electrons. While the number of backscattered electrons mostly depends on the mass of the atoms the electron beam encounters, thus giving information about the chemical composition of the sample, the number of secondary electrons depends mostly on the topography of the sample: a crest in the surface has more area to let secondary electrons escape than a dip, so the detector registers a higher electron count for it.

4.2.7 Focussed Ion Beam

The Focussed Ion Beam (FIB) is a technique that uses the same basic principle as electron microscopy but, instead of an electron beam, a beam of heavy ions is used, usually Ga^+. The technique can therefore be used for imaging but also for manipulation of the sample, in terms of material removal as well as for deposition. The ions are produced by a tungsten needle wet with gallium that is subjected to a high voltage that removes Ga ions from the liquid Ga, that are then accelerated and focused into a beam similar to the electrons in electron microscopy. By using different acceleration voltages, it is possible to either use the ion beam for imaging or for manipulation of the sample. At low voltages, the ions produce secondary electrons and ions that can be detected to build images. At higher energies the sputtering effect is predominant so it can be used to mill away material in a controlled manner. This is used, for instance, to create structures on the sample surface or to cut away material in order to look inside the grains in polycrystalline materials.

4.2.8 Energy Dispersive X-ray Spectroscopy

An important method for the determination of the elemental composition of a sample is based upon the characteristic X-ray emission from its elements, stimulated by a focussed beam of electrons. The electron beam can knock out electrons from the inner shells (K, L) of the elements constituting the sample. The following relaxation of the excited state involves the generation and emission of characteristic X photons. The energies of the emitted photons depend on the atomic number and on the energy levels of the electronic states involved in the transition the produces the X photon. The X-ray emission is, then, analysed by an energy dispersive spectrometer, giving qualitative information about the elemental composition of a sample.

4.2.9 X-ray Photoelectron Spectroscopy

X-ray Photoelectron Spectroscopy (XPS) is an analytical technique that uses the photoelectrical effect in order to analyse a sample in terms of elemental composition and electronic configuration of the species. The energy needed to remove an electron is, in fact, characteristic not only for each element but also for each electron shell, that is for how strong the electron is bound to the material. The binding energy of electrons is sensitive to the chemical environment (i.e. binding state, oxidation state) the element is in. This makes possible to gain information ranging from the elemental composition of a sample, over the exact environment of the elements within it, to the band structure of the electrons. An X-ray photoelectron spectrometer consists mainly of three parts: an X-ray

source, the sample holder and a detector that resolves photoelectrons by their kinetic energy. As X-rays hit the sample, photoelectrons are produced. These are then focussed by an array of magnetic lenses and sent through an energy analyser. By scanning through a voltage range it is possible to record an energy spectrum of the photoelectrons. Since in this process electrons are removed from the sample, the sample material either has to be conductive to transport away the accumulating positive charge, or it is necessary to counter the phenomenon by using an electron gun that replenishes the lost electrons.

4.2.10 IR spectroscopy

Atomic positions in chemical species are not immobile nor fixed, but ever fluctuating due to vibrational motions within the molecule or the crystalline solid material. These vibrations can be divided in two main categories: stretching and bending. The first kind implies the change in the interatomic distance along the bond axis. Bending vibrations are characterised by variations of the angle between two bonds: scissoring and rocking in the plane, wagging and twisting out of the plane. To each of these vibrations is associated a particular energy, with respect to the system that is analysed.

The infrared (IR) region of the electromagnetic spectrum spans from about 12800 to 10 cm^{-1} and the most utilised for analytical purposes extends from 4000 to 400 cm^{-1}. This kind of radiation interacts with molecular species presenting comparable energy differences in their vibrational states. For the radiation to interact with the system under study, a net change in the dipole moment (or charge distribution) of this latter (or portion of it) must be possible as a consequence of vibrational or rotational motion, hence producing a transfer of energy with the absorption of one or more frequencies (usually a band) of the IR radiation. For this reason, homonuclear diatomic species such as H_2, O_2, N_2, Cl_2, cannot interact with IR radiation. By means of IR spectra collected on polycrystalline hydrated samples it is possible to obtain information about the energies involved in the stretching of the O–H and therefore the energy landscape of the protonic defects in the materials.

IR spectrometer

IR spectra of the hydrated powders were collected on a ThermoFisher Scientific Nicolet 6700 FT-IR spectrometer with Collector II accessory for diffuse reflection measurements. The instrument mounts a DTGS (deuterated triglycine sulfate)-KBr detector, a KBr beamsplitter, and is equipped with a diamond window. Spectra were collected in air at room temperature, between 4000 and 400 cm^{-1}, with a resolution of 2 cm^{-1}.

4.2.11 Raman spectroscopy

When a radiation beam hits a sample, a small fraction of its intensity is scattered in all directions. The wavelength of the scattered radiation differs from that of the incident beam and this phenomenon, called *inelastic scattering*, is the result of quantised vibrational transitions due to the structure of the system under study. The differences in energy correspond to wavelengths in the IR region but the species that are active in Raman spectroscopy may not be so in IR spectroscopy, therefore the techniques may be used on a complementary basis. While in IR spectroscopy a vibration mode must be associated to a variation of the dipole moment for it to be active, in Raman spectroscopy the scattered light is the result of a momentary distortion of the electrons involved in a bond. Such a distortion implies only a temporary polarisation and the induced instantaneous dipole is cancelled after the relaxation and re-emission.

The polarisability of a bond varies periodically with its stretching vibrations, attaining its maximum value with the larger separation distance. When the radiation is re-emitted, a Raman *shift* is observed, with a frequency corresponding to that of the vibrational mode. There are therefore three kinds of scattered radiation: *Stokes*, *anti-Stokes*, and *Rayleigh*, the latter corresponding to the frequency of the incident radiation. Stokes shifts are characterised by bands situated at lower frequencies, and anti-Stokes ones are found in the higher frequency region of the spectrum, with respect to the Rayleigh band.

Raman spectra are obtained by irradiating a sample with a powerful laser beam, with a wavelength in the visible or IR portion of the electromagnetic spectrum, but different from the absorption bands of the analyte. During irradiation, the spectrum of the inelastically scattered radiation is measured at a certain angle, usually 90°. It is noteworthy that Raman shifts are independent from the particular wavelength used for the excitation therefore a different type of laser won't alter the information obtained.

Raman spectrometer

Raman spectra were measured at the temperatures of 80 K and 300 K, using a Renishaw InVia Reflex spectrometer. A 532 nm laser was used as the excitation source and the laser beam was focused on the sample through a ×50 objective lens (NA = 0.5). The power of the laser beam impinging on the sample was approximately 1 mW. The light backscattered from the sample was then collected through the same objective lens and was dispersed by a 2400 l/mm grating prior to the detection by a CCD camera. Each spectrum was recorded for 10 s over 3-6 accumulations. The temperature was controlled by a Linkam THMS 600 heating stage.

4.2.12 *Neutron vibrational spectroscopy (Inelastic Neutron Scattering)*

A representation of the neutron-nucleus scattering event is shown in *fig. 4.8*. The energy, $\hbar\omega = E_i - E_f$, and momentum, $\boldsymbol{Q} = \boldsymbol{k}_i - \boldsymbol{k}_f$, exchanged are determined by the initial (i) and final (f) states of the neutron, that is before and after the scattering event. When no energy is exchanged $\hbar\omega = 0$ and the scattring is referred to as *elastic*, otherwise the scattering event is called *inelastic*.

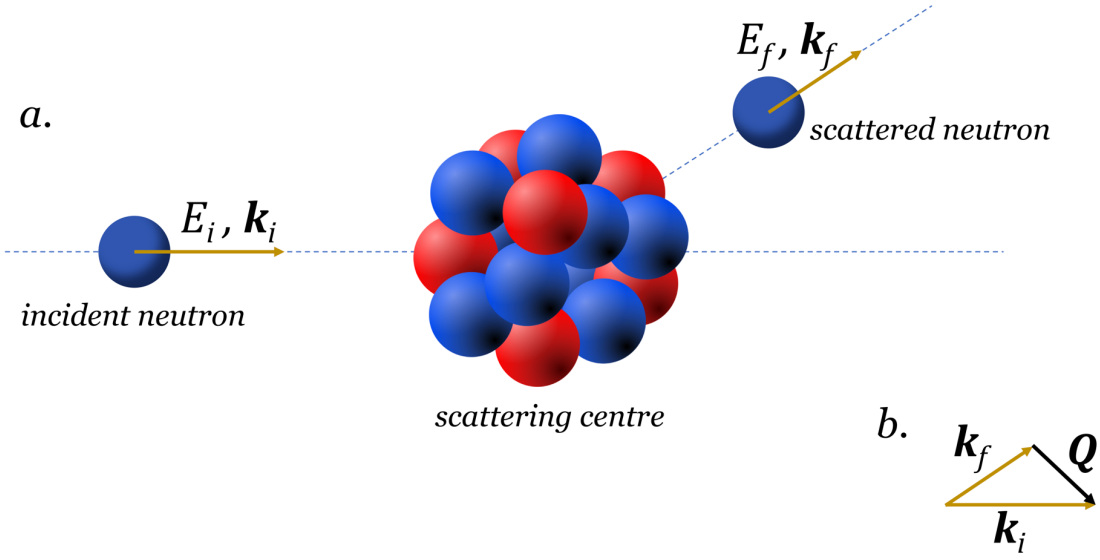

Fig. 4.8 Illustration of the neutron scattering process (*a.*) and representation of the transferred momentum $\boldsymbol{Q} = \boldsymbol{k}_i - \boldsymbol{k}_f$ (*b.*).

In an inelastic neutron scattering experiment (INS), the intensity of scattered neutrons, $S(\boldsymbol{Q}, \omega)$, is measured as a function of transferred energy, $\hbar\omega$, and momentum transfer, $\boldsymbol{Q}$, both at the same time. The energies lost by the neutron correspond to the position of the observed transitions (eigenvalues), which are a function of the structure and of intramolecular forces. The momentum loss experienced by the neutron, and the atomic displacement occurring during a vibration (eigenvectors) are, instead, linked to the strength of the observed transitions. Atomic displacements are determined by structure and intramolecular forces but the momentum transferred is determined by the particular instrument used for the INS experiment. The energies of *thermal* and *cold* neutrons, the ones used in scattering experiments, are comparable to the energies of IR and microwaves radiations, and much smaller than X-rays ones. These energies are the ones needed for the study of vibrational dynamics in solid-state materials and the technique offers resolutions ranging from meV to neV. Further, INS is not subject to optical selection rules and all vibrations are active and, in principle, measurable. The technique was used to study the proton local environment in BTS samples, and in particular the O–H vibrational modes, wag (δ) and stretch (ν).

The neutron spectrometers IN1-LAGRANGE, TOSCA and MAPS

INS experiments were performed on different instruments, in order to cover a large energy range and to provide opportune resolutions and counting statistics for the analysis of the data. For INS spectroscopy, the most relevant instruments are built with either direct or indirect geometry (*fig. 4.9*). For the direct geometry instruments, the incident energy of the neutron beam is fixed and the INS intensity is measured for different final energies. Instruments that fix the final energy are known as indirect geometry instruments.

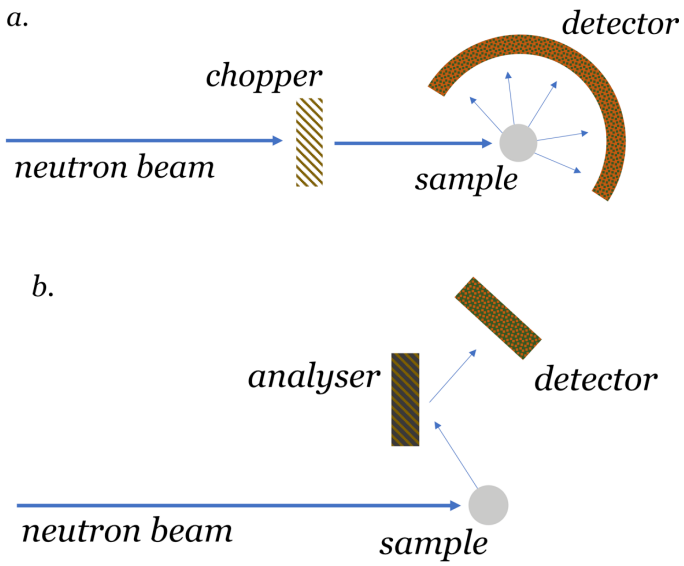

Fig. 4.9 Schematic representation of a direct geometry (*a.*) and an indirect geometry (*b.*) INS spectrometer.

The IN1-LAGRANGE (LArge GRaphite ANalyser for Genuine Excitations) is an indirect geometry spectrometer, based on the space focussing of neutrons scattered by the sample in a very large solid angle (≈ 0.8π ≈ 2.5 Steradian), all recorded with a relatively small single counter (a ^{3}He gas detector). The focussing reflecting surface of ≈ 1 m^2 is built from pyrolytic graphite crystals set to reflect neutrons with the fixed average energy of 4.5 meV. Using a combination of monochromator crystals, spectra were collected over the energy range 0-500 meV, and with increased statistics in the region 50-200 meV in order to obtain information about the O-H vibrational stretching mode. This spectrometer is located at the Institut Laue-Langevin (ILL) in Grenoble, France.

TOSCA is another indirect geometry spectrometer optimised for vibrational spectroscopy in the 0-500 meV region. Scattered neutrons are Bragg reflected from a pyrolytic graphite analyser, to yield a final energy of about 4 meV. Neutrons are then detected by an array of ^{3}He gas tubes, distributed over five forward detector banks, with a scattering angle of 45°, and five backscattering banks, with an angle of 135°. The instrument was used to complement the IN1-LAGRANGE dataset over the extended O–H stretching mode region.

MAPS is a direct geometry spectrometer that was used to study O–H stretching vibrations, in the energy region 300-600 meV. Spectra were collected with incident energies of 650 meV and 300 meV, with respective chopper frequencies of 600 Hz and 400 Hz. Scattered neutrons are detected by a 16 m^2 array of position sensitive ^3He gas tubes. Both TOSCA and MAPS are located at the ISIS Neutron and Muon Source in Harwell, UK.

Chapter 5
The BTS system: results and discussion

5.1 Introduction

The perovskite-like system $Ba_2(In_{1-x}Ti_x)_2O_{5+x}$[100–102,136] has received attention for the significant level of proton conduction. This mixed indate-titanate system, a brownmillerite with a phase transformation to disordered cubic perovskite for $x > 0.15$, shows a maximum in proton conductivity for the composition with $x = 0.2$, where $\sigma = 1.1\times10^{-3}$ S/cm at 450 °C, under wet N_2[102]. For the $x = 0.5$ composition, the conductivity is at least one order of magnitude lower, in the same temperature range and wet atmosphere[103]. Reverse Monte Carlo analysis of neutron diffraction data of $BaTi_{0.5}In_{0.5}O_{2.53}(OD)_{0.44}$[53] reveals that its oxide ions framework results from the combination of regular InO_6 and distorted TiO_6 octahedra, and suggests a negative impact on the proton mobility due to the presence of multiple, size mismatched metal environments. The substitution of scandium for titanium should alleviate this size mismatch, as Sc^{3+} (0.74 Å) is smaller than In^{3+} (0.80 Å), in a hexacoordinated environment[137].

The $BaTi_{1-x}Sc_xO_{3-x/2}$ system forms the basis of this work, done to understand how structure influences proton mobility and to develop strategies to optimise doped materials. The early studies on this system[14,15,138] provided a number of interesting observations. The series undergoes a structural transformation driven by the scandium content, with 6H hexagonal perovskite structures for $x < 0.2$, cubic perovskite-like structures for $x > 0.5$, and a multiphasic region in-between[15]. Proton conductivity, which is fairly good in the highly Sc-substituted samples, is dramatically affected by the structural type, with the highest conductivity observed for the cubic $x = 0.7$ member, where $\sigma \approx 10^{-3}$ S/cm *vs.* $\sigma \approx 10^{-5}$ S/cm for the hexagonal ones, under wet Ar at 500 °C[15]. Further, proton conductivities in the cubic members of the series are significantly greater than in similar perovskite-structured heavily acceptor-doped titanates like $BaTi_{0.5}In_{0.5}O_{3-\delta}$[103] and $BaTi_{0.2}In_{0.8}O_{3-\delta}$[136], and zirconate phases like $BaZr_{0.5}In_{0.5}O_{3-\delta}$[139] and $BaZr_{0.5}Yb_{0.5}O_{3-\delta}$[140].

In the temperature range 700 to 200 °C, in the cubic members under inert wet conditions, charge carriers are predominantly protons, and proton transference numbers are close to unitary below 500 °C[15]. For $x = 0.5$ the vibrational band associated to the

stretching of the O—H bond is quite broad[14], suggesting that protons experience a range of hydrogen bonding strengths, which means a range of nearest oxygen interactions that weaken the primary O—H bond and lower its vibrational frequency, as observed in the series $BaZr_{1-x}In_xO_{3-\delta}$[55]. The cubic x = 0.5 is also characterised by a surprisingly small lattice expansion that accompanies the hydration of the material[14]. Hydration thermodynamics become more favourable with increasing Sc content in the cubic members, as $\Delta_{hydr}H°$ = −57(2) kJ/mol for x = 0.5, and $\Delta_{hydr}H°$ = −83(2) kJ/mol for x = 0.7, while the hexagonal phase, with x = 0.2, is capable of retaining the protonic defects to higher temperatures with respect to its cubic counterparts, with its $\Delta_{hydr}H°$ = −108(2) kJ/mol[138].

These results opened a Pandora's box of new clues and questions that were examined and addressed in the studies that are included in this thesis. Firstly, they strongly hinted at the difference in cationic ordering and oxygen vacancy distribution that would characterise the members of the series on the basis of its polymorphism driven by the scandium content. Those differences were investigated in paper I[123] and by exploratory works on hexagonal phases with x = ⅙ and ⅓, and a metastable cubic phase[141] with 20 mol% Sc substitution. Further, local environments seem to play a crucial role for proton transport and structural dynamics, especially in the cubic phases, as differences in proton conductivity and in the hydration/dehydration behaviour are hardly explained only by the number of protonic defects in the hydrated materials, and vacancies in the dried ones. These questions were tackled by the work presented in papers II[124], III and IV.

5.2 Optimisation of synthesis route

The main information regarding the synthesis of BTS materials is reported in papers I[123] and II[124], and in section *4.1.1*. Here, additional details about the reasons that justify the use of sacrificial powder during the syntheses are given. Evidence of Ba loss from BTS samples were, in fact, investigated but not found, from the results of the Rietveld analyses[123]. The observation of diffusion phenomena of metallic species in the reaction vessels (*fig. 5.1*), though, and the differences in the XRD patterns of the samples and the loose powders was convincing for justifying the consistent use of the (time-consuming but safe) embedding procedure. Also, the attempted syntheses of a BTS phase with x = ⅓ and of a metastable cubic phase with 20 mol% Sc substitution are reported, in order to give a heads-up to the reader interested in follow-up studies.

5.2.1 Embedding procedure

Above 1000 °C, the mixtures of powders were intensively ground (up to 2 h) and pelletised by uniaxial pressing, then embedded in loose sacrificial powder, to avoid any undesired reaction with the reaction vessel (*fig. 5.1a*) and to prevent volatilisation of BaO, that, especially above 1300 °C, could affect detrimentally the intended compositions (*fig. 5.1b*). The problem of BaO exsolution or evaporation is, in fact, known[142] and

acknowledged in the field thanks to the vast literature on doped $BaCeO_3$ and $BaZrO_3$. Several authors have faced the problem of the stoichiometric ratio between A and B site when synthesising and/or sintering Ba-based perovskite materials. The presence of a BaO-rich grain boundary phase was reported in Gd-doped $BaCeO_3$[38], and the discrepancies in reported proton conductivities in Gd- and Y-doped $BaCeO_3$ revealed that variations in stoichiometry in the A site have a dramatic effect on proton conductivity[143,144]. The same was observed by Snijkers and co-authors[145] who investigated the effect of both a stoichiometric amount and an excess of $BaCO_3$ in the starting mixtures of reactants for the synthesis of 10 mol% Y-doped $BaZrO_3$: in samples produced from excess $BaCO_3$ the conductivity is increased by about one order of magnitude. These observations prompted following authors[146,147] to embed the pressed powders in a mixture of the same sample powder added of a 10 mass% of $BaCO_3$. Although the procedure has quantifiable effects[146] over the stoichiometry of 20 mol% Y-doped $BaZrO_3$ samples, the BaO evaporation phenomenon seems to differ in its effects with respect to the system composition and the thermal history of the sample[148].

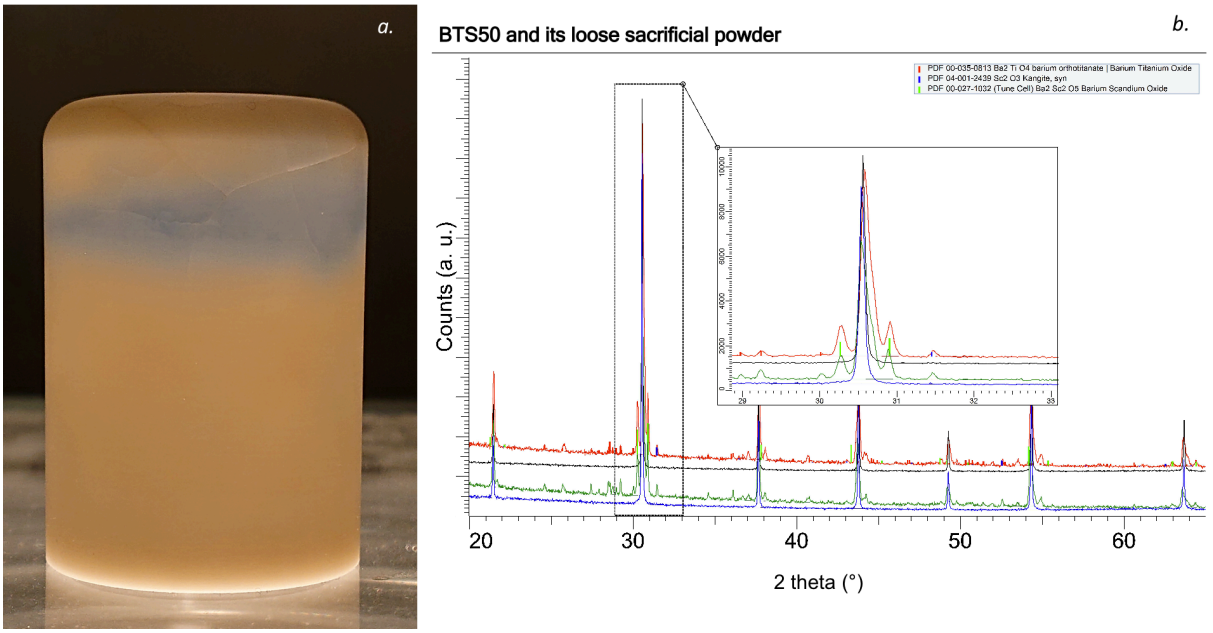

Fig. 5.1 Stained reaction crucible (*a.*) and X-ray diffractograms relative to the last synthesis steps of $BaTi_{0.5}Sc_{0.5}O_{3-\delta}$, BTS50 (*b.*). The blue coloured stain on the α-Al_2O_3 crucible is probably due to the diffusion of Ti^{IV} into the corundum structure, giving blue sapphire. This is reflected, in the loose sacrificial powder (green and red XRD patterns), by the formation of Ti poor phases such as Ba_2TiO_4, and Sc_2O_3 and $Ba_2Sc_2O_5$ where Ti is absent.

In *fig. 5.2* is shown the evolution of the XRD patterns of the loose powder used in the synthesis of BTS50. The persistence of phases where the stoichiometry indicates Ti loss, such as Ba_2TiO_4, and $Ba_2Sc_2O_5$ and Sc_2O_3, is noticeable and reinforces the need for a sacrificial powder. This is also shown by the diffractograms that followed the thermal treatments which the as-prepared BTS50 powder underwent during sintering in the form of a pellet (*fig. 5.3*). The absence of an embedding medium has a detrimental effect that is

clearly visible from the XRD patterns of the surface of the pellets with the formation of secondary phases.

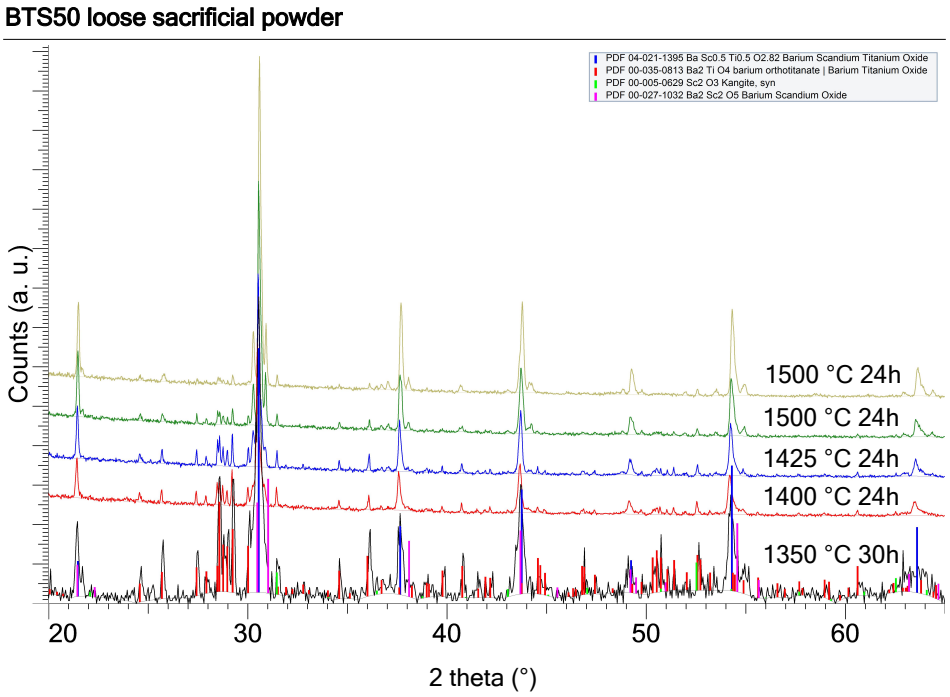

Fig. 5.2 Evolution of the phases constituting the loose embedding powder utilised in the synthesis of BTS50.

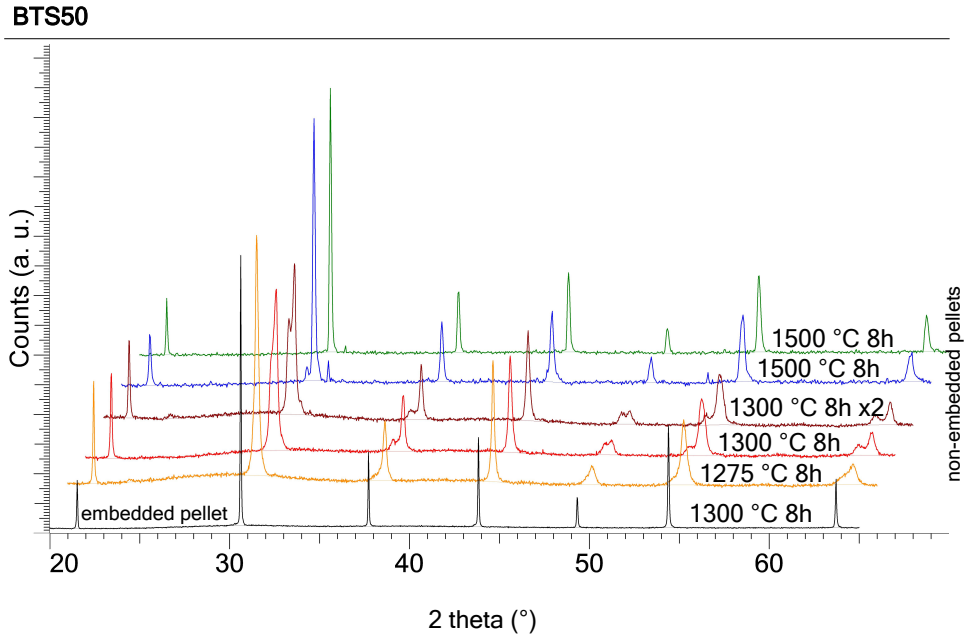

Fig. 5.3 Effect of the presence, compared to the absence, of an embedding medium during the sintering of a pellet of BTS50 powder. Diffractograms are offset for clarity.

In particular, the sides of the pellet sintered at 1500 °C show a difference in their composition and reveal the effects of a loss of Ba in the surface exposed to air, and of Ti on the surface in contact with the crucible (*fig. 5.4*). The diffractograms indicate that the volatilisation of Ba induces the segregation of Sc_2O_3 away from the main phase, while the diffusion of Ti into the reaction vessel causes the formation of Ti-poor phases and segregation of Sc_2O_3. Interestingly, none of that occurs while sintering BTS70, that seems to be unaffected by any other thermal treatments, at least up to 1300 °C. A possible explanation for such behaviour can be found from the comparison of the $\Delta_{Hydr}H°$ and Goldschmidt tolerance factors of the two materials. As Sc content increases, $\Delta_{Hydr}H°$ becomes more exothermic[138] and the tolerance factor decreases (t_{50} = 1.03, t_{70} = 1.02). As suggested by Bjørheim and co-authors[138], since there are no changes in the crystal symmetry, this trend reflects the stability of the oxide, which is evident in the experimental results.

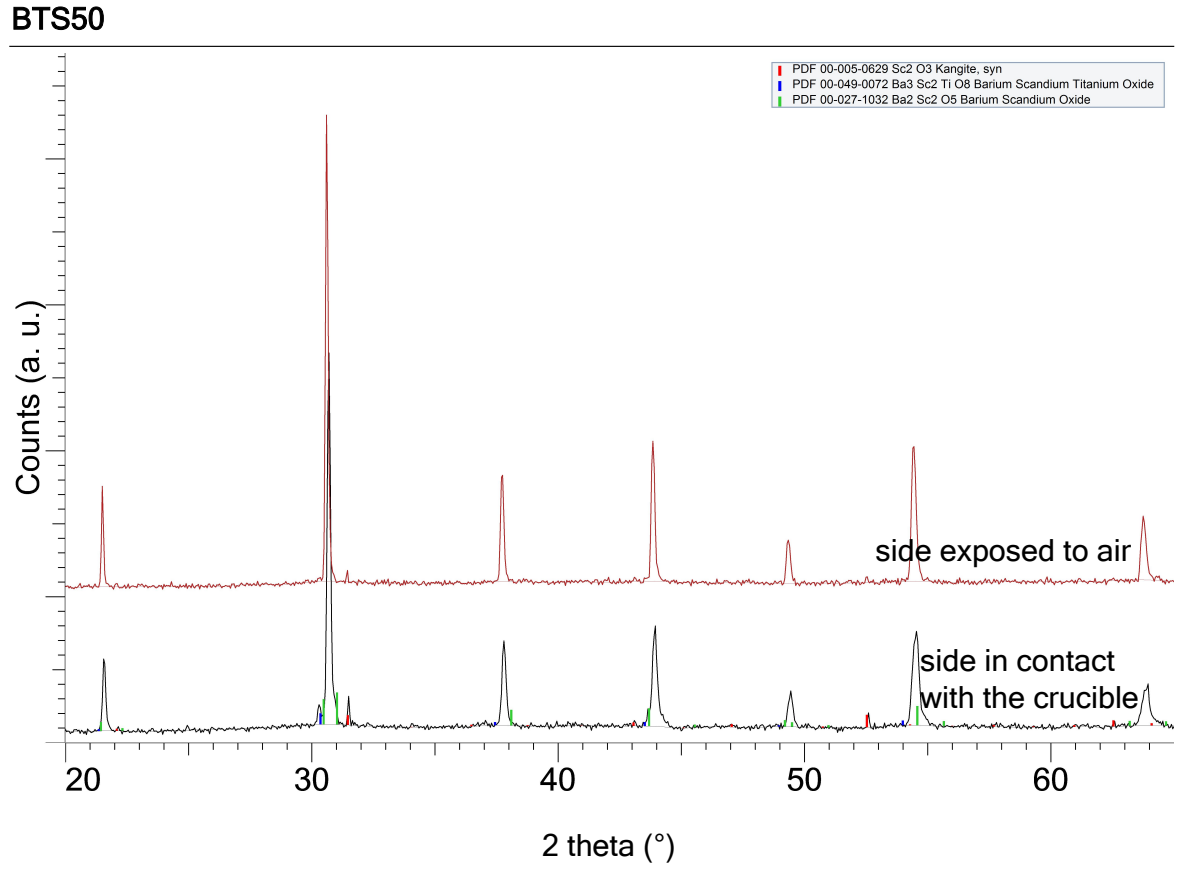

Fig. 5.4 Different sides of a pellet of as-prepared BTS50 powder, sintered at 1500 °C for 8h.

5.2.2 Synthesis of hexagonal BTS⅙ and BTS⅓, and of metastable cubic BTS20

In order to thoroughly describe the hexagonal structural types and confirm the ordering of cations[123], several attempts (solid-state and sol-gel) at synthesising the samples with x = ⅙ and x = ⅓ were made. The first would exhibit a 50-50 % shared occupancy of the *2a* site by Sc and Ti. The second would be characterised by a complete segregation of Sc into *2a* crystal sites. Exploratory synthetic work (2 g of sample) gave encouraging results and the syntheses were scaled up to meet the requirements for NPD experiments. Of the syntheses carried out at the solid state, only the x = ⅙ was successful while the x = ⅓ was not. Indeed, for x = ⅓, the synthesis presents some difficulties as even slight stoichiometric imbalances put the system in that region of Sc content where multiple phases coexist (*fig. 5.5*). Besides unreacted Sc_2O_3, other unidentified phases are present along with the main, desired compound. This result supports the hypothesis of Sc content as driver for the structural transformation from hexagonal to cubic types since getting closer to full occupancy of *2a* sites by Sc complicates the synthesis of pure phases.

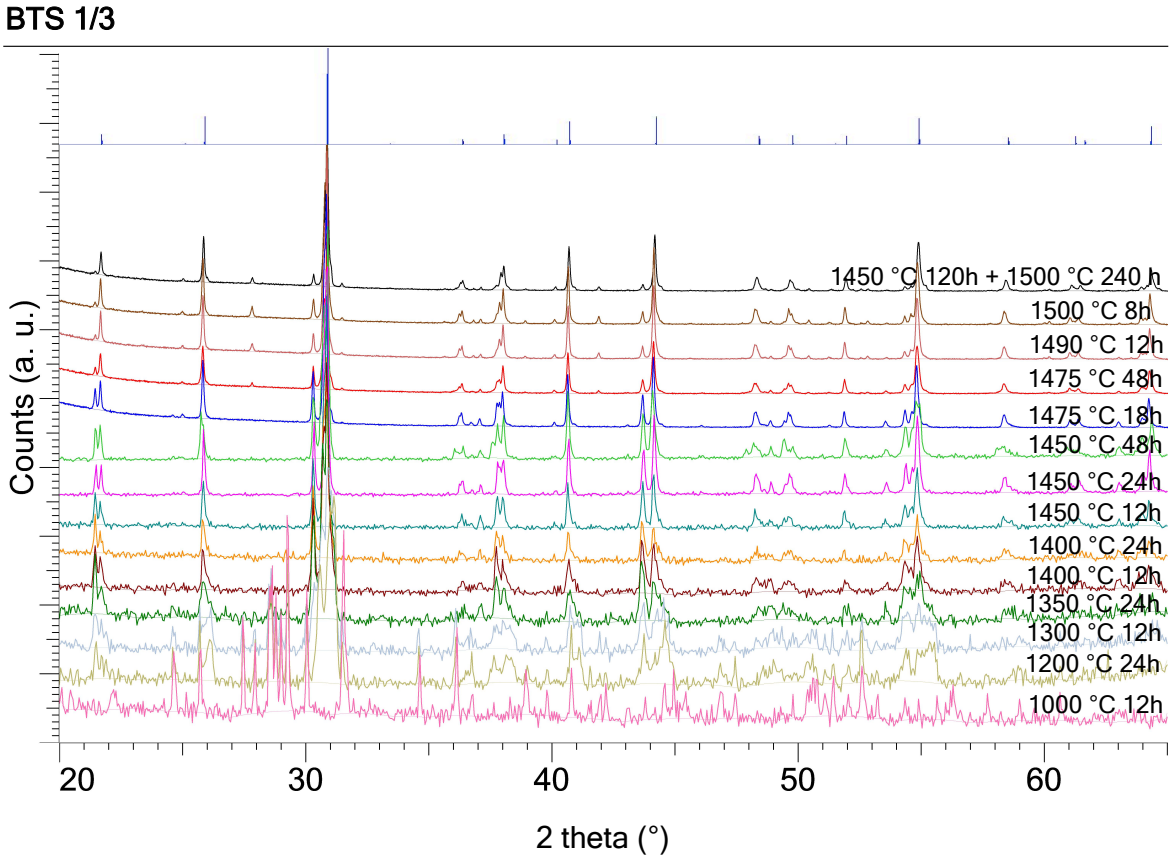

Fig. 5.5 Evolution of the sample BTS⅓ with increasing temperature and residence time along the solid-state synthesis steps. The inset on top shows the theoretical Bragg peaks corresponding to a phase of stoichiometry $BaTi_{⅔}Sc_{⅓}O_{2.92}$ built on the basis of the 6H structural model with a = 5.77 Å, and c = 14.14 Å.

The advantages offered by a sol-gel method were, hence, exploited to synthesise the $x = ⅓$ phase, along with another composition with $x = 0.2$ that in its metastable form would crystallise as a cubic $Pm\bar{3}m$ perovskite[141]. Synthesising a 20 mol% Sc-doped material exhibiting a cubic perovskite structure would make possible a direct comparison of the electrochemical behaviour of two phases with the same composition but with different crystal structure. This would unequivocally show that the localisation of protons in the 6H structure is the reason for its poorer conductivity. The evolution of the hexagonal phase with $x = ⅓$ is shown in *fig. 5.6*. After its annealing at 1300 °C, a heat treatment under dynamic vacuum (10^{-4} mbar) and acidic washing followed by filtration and annealing in air were employed in order to ameliorate the purity of the sample since higher temperatures promoted the formation of parasitic phases. The exsolution of Sc_2O_3 and the limited amount recovered (*ca.* 3 g) discouraged the NPD experiment.

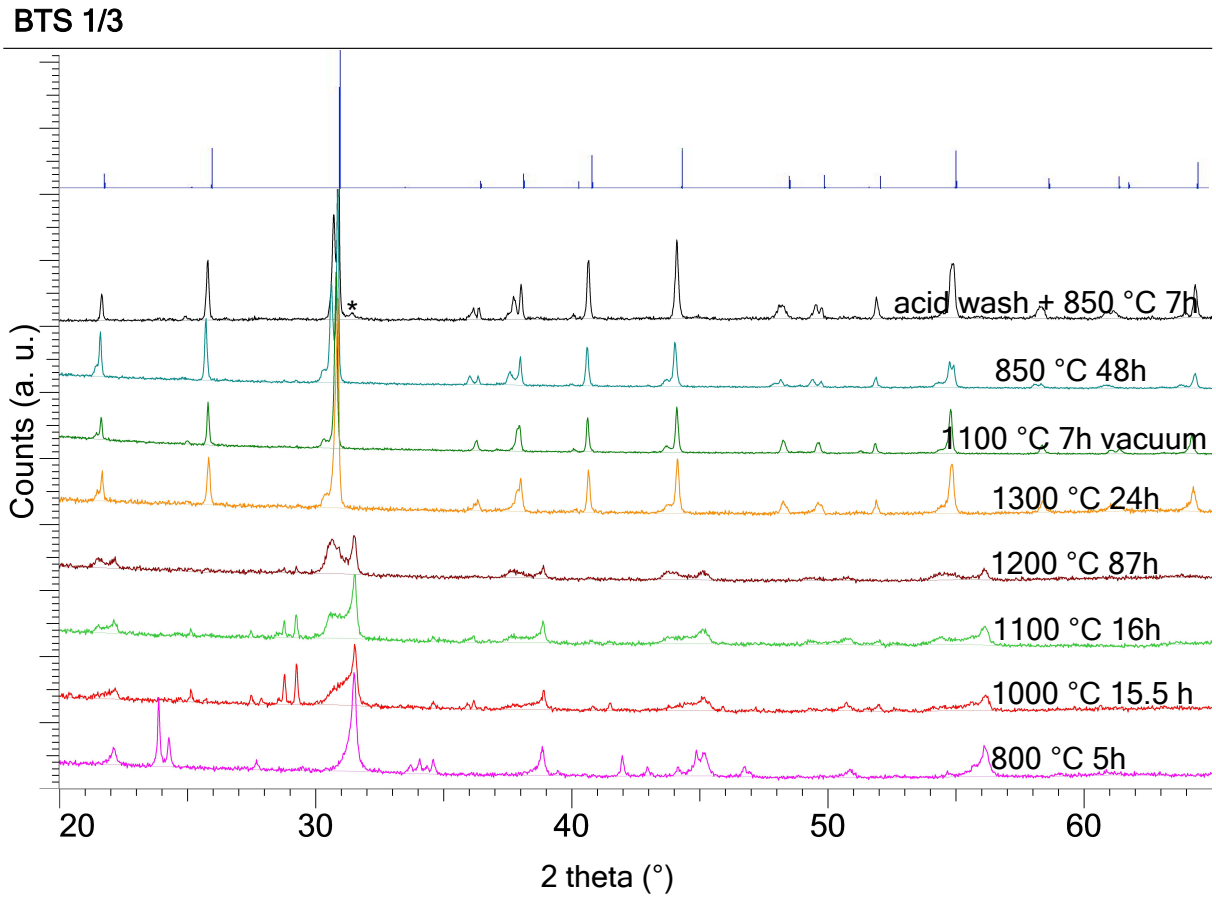

Fig. 5.6 Evolution of the sample BTS⅓ produced with the sol-gel method. The asterisk indicates the presence of Sc_2O_3. The inset on top shows the theoretical Bragg peaks corresponding to a phase of stoichiometry $BaTi_{⅔}Sc_{⅓}O_{2.92}$ built on the basis of the 6H structural model with a = 5.77 Å, and c = 14.14 Å.

The cubic $x = 0.2$ phase formed already at 800 °C but it was contaminated by $BaCO_3$, a secondary hexagonal phase, and Sc_2O_3. *Figure 5.7* shows the evolution of the phase with the heat treatments, and a closer detail of the 2ϑ region 20°-42.5° highlighting the secondary phases.

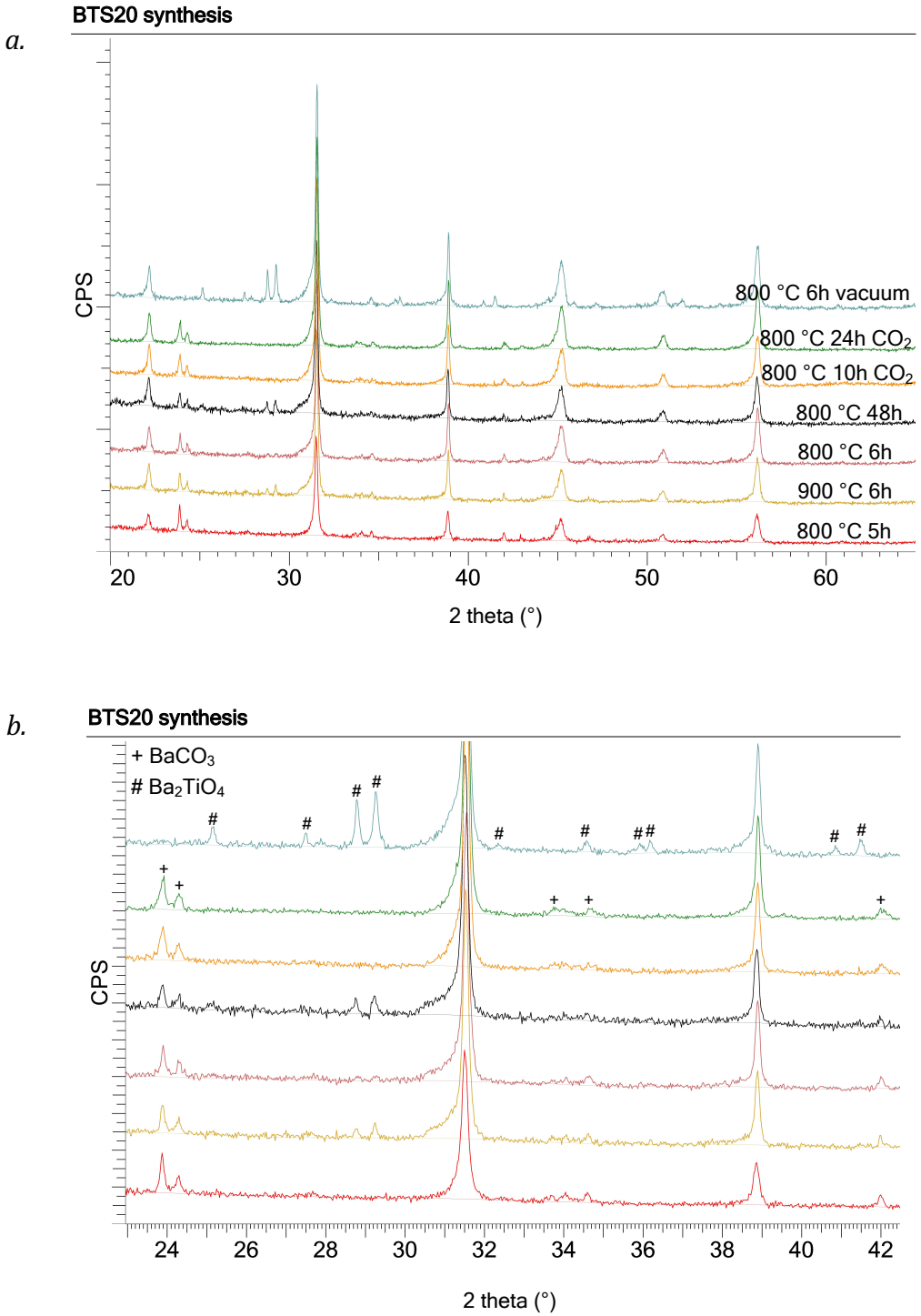

Fig. 5.7 (*a*). Evolution of the cubic sample BTS20 with increasing temperature and residence time along the synthesis steps; (*b.*) details of the diffractograms highlighting the presence of secondary phases $BaCO_3$ and Ba_2TiO_4.

Ba_2TiO_4 is a phase that commonly occurs during the sol-gel synthesis of $BaTiO_3$[149] and that it is suppressed by annealing the sample under CO_2, as from *equilibrium 5.1*. Under vacuum, at 800 °C, Ba_2TiO_4 forms again.

$$BaTiO_3 + BaCO_3 \rightleftarrows Ba_2TiO_4 + CO_2 \quad (5.1)$$

Higher temperatures promoted the irreversible formation of secondary phases and were therefore detrimental to the purity of BTS20 cubic (*fig. 5.8*).

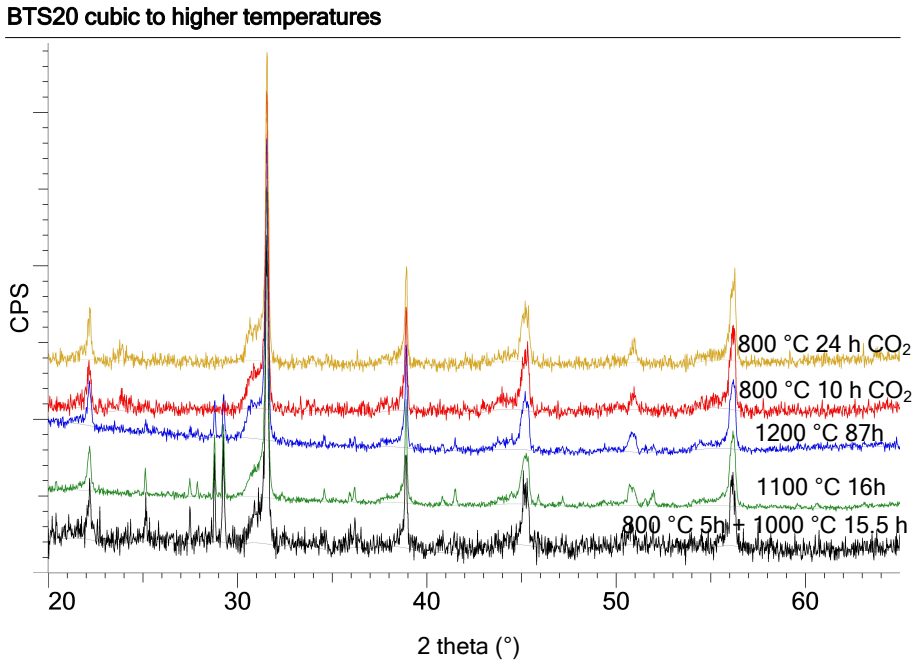

Fig. 5.8 The evolution of the cubic sample BTS20 with increasing temperature and residence time along the synthesis steps.

5.2.3 Summary

All BTS samples were synthesised *via* solid-state route. The use of an embedding procedure with sacrificial powder proved to be crucial as BaO volatilisation and Ti diffusion into the reaction vessels must be prevented in order to have control over the system and obtain target stoichiometries. The same route for the synthesis of BTS⅓ demonstrated scalability issues. Despite the unsuccess, this result indirectly supports the hypothesis of Sc doping level as driver for the structural transformation from hexagonal to cubic types. The sol-gel syntheses were complicated by the higher reactivity of the fine powders. The increased surface-to-volume ratio facilitates the formation of carbonated species therefore a careful choice of experimental conditions is recommended, such as controlled atmosphere with a higher pO_2/pCO_2 ratio and smaller temperature increases.

5.3 Structural characterisation

From the early XRD and impedance data on the series[15], the suspicion of a different ordering for Sc and Ti in the hexagonal phases, along with the ordering of vacancies and proton sites, was strong and therefore the first materials produced for the neutron diffraction characterisation were the hexagonal $x = 0.2$ and the cubic $x = 0.7$, respectively worst and best material with respect to proton conduction properties. From the Rietveld refinements of diffraction data[123], the ordering of Sc and Ti in the hexagonal 6H structure was found: Sc occupies the *2a* position, and Ti is distributed over *2a* and *4f* sites (*fig. 5.9*). Further, oxygen vacancies were found to lie in the plane of the shared faces of the TiO_{9-x} dimers, the O(1) position *6h* (*fig. 5.10*). Once vacancies are filled with water, as from *equilibrium* 2.*1*, protons sit in a *12j* position, in the same plane (*fig. 5.10*).

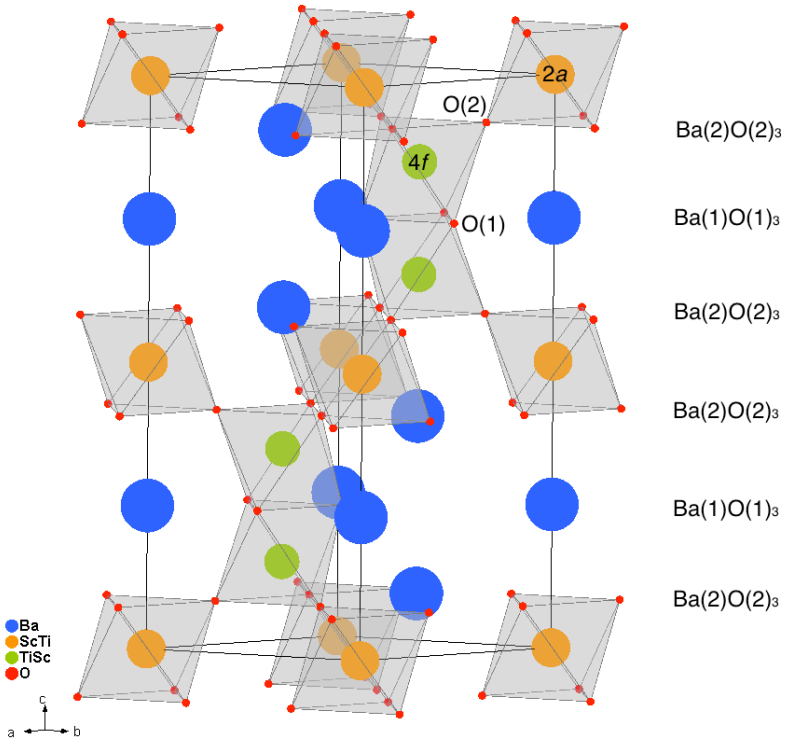

Fig. 5.9 Polyhedral representation of the hexagonal 6H structure of the phase $BaTi_{0.8}Sc_{0.2}O_{3-\delta}$, BTS20, after the Rietveld analysis. Meaningful crystallographic sites are labelled where necessary. The hexagonal structure, crystallising in the $P6_3/mmc$ space group, is composed of MO_3 layers (M = Sc, Ti) stacked in a $(hcc)_2$ succession, resulting in pairs of MO_6 face-sharing octahedra that are linked by corner-sharing octahedra.

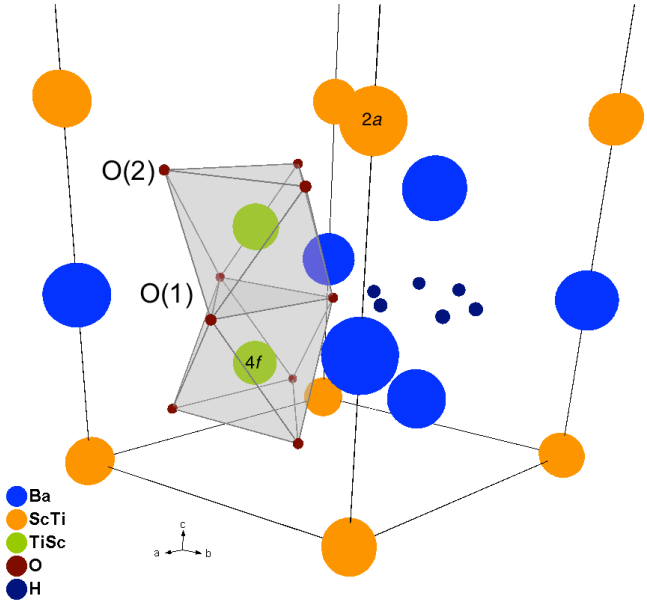

Fig. 5.10 Enlarged view of the hexagonal 6H structure, highlighting the oxygen positions and showing the refined proton positions and their local coordination.

For cubic BTS70 (*fig. 5.11 a* and *b*), Sc and Ti are statistically distributed over the same lattice site, *1a*, and protons are highly disordered around the single oxygen site, in a 24-fold position, *24k*.

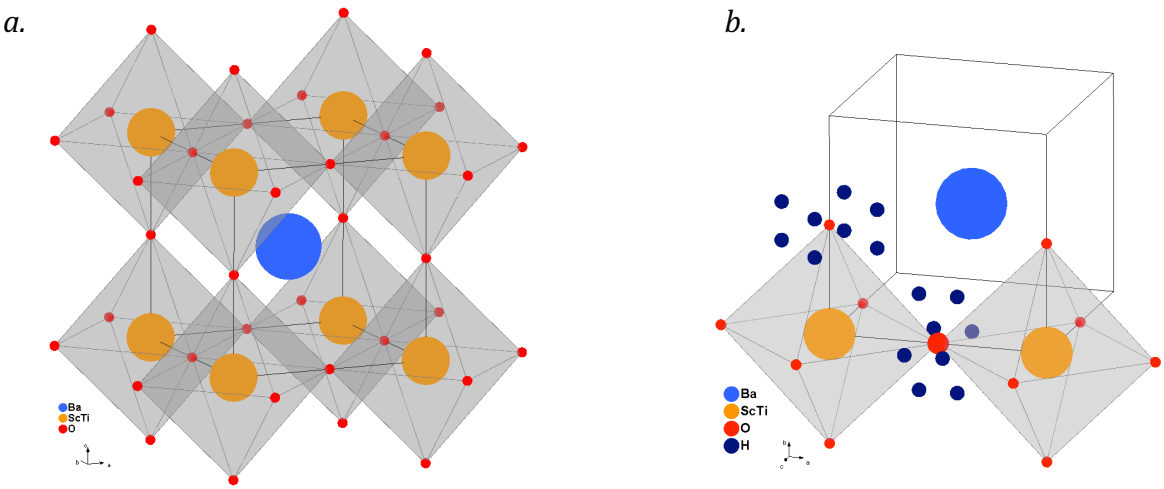

Fig. 5.11 (*a.*) Polyhedral representation of the cubic structure (space group: $Pm\bar{3}m$) of the phase $BaTi_{0.3}Sc_{0.7}O_{3-\delta}$, BTS70, after the Rietveld analysis; (*b.*) refined proton positions and their local coordination.

These structural models are clear in pointing towards the protonic ordering in the 6H hexagonal type as the reason for the poorer performance of BTS20 in conducting protons. Here protons are more localised and their diffusion requires a path *via* a proton site that is characterised by a higher energy and is unoccupied at room temperature[123]. On the other hand, the same average models are limited in providing the necessary information that would allow a more detailed understanding of the oxygen and proton disorder that seems to characterise the cubic types (Sc ≥ 50%). This is indicated by the presence of a large diffuse scattering component in BTS70 (*fig. 5.12*). The analysis of the diffuse scattering with the Reverse Monte Carlo method provides just that information.

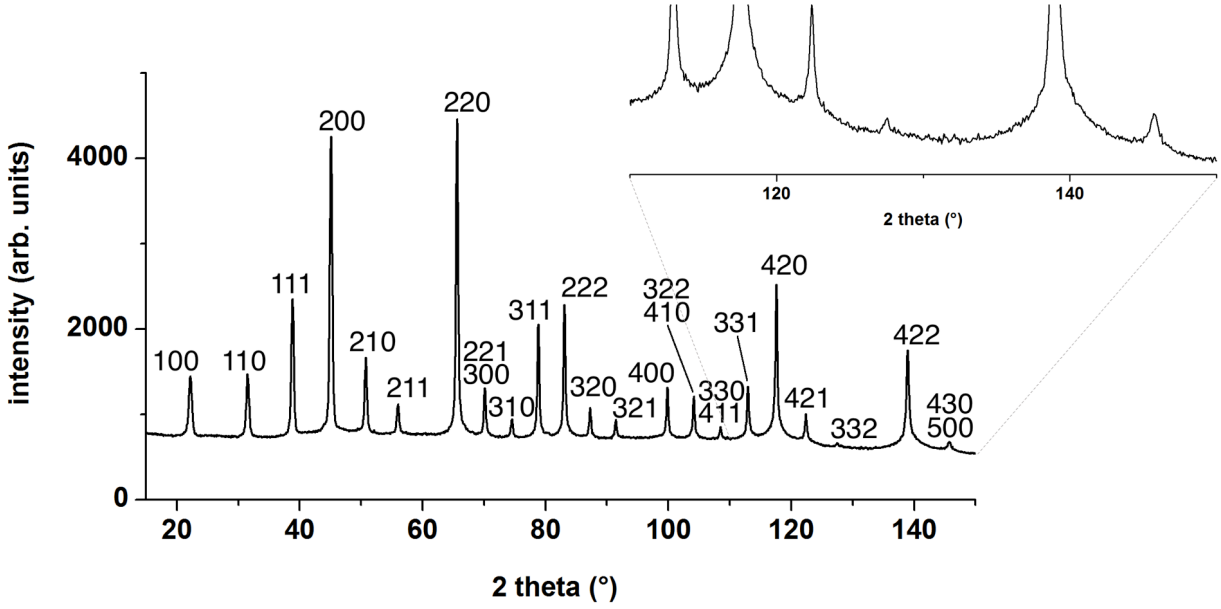

Fig. 5.12 Constant wavelength neutron diffraction diagram for BTS70H at room temperature, showing the indexed Bragg peaks and an expansion of the 2θ region 130°-150°, where broadening at the base of the (420) and (422) peaks is visible, indicative of diffuse scattering.

The results of the Rietveld analysis are able, nevertheless, to explain the reason for the structural transformation that accompanies the increasing level of Sc substitution in the series. A too short Ti–Ti separation distance, 2.755(7) Å, is likely to be responsible for the cationic ordering in the 6H structure, as the shortest M–M distance in Sc_2O_3 is 3.24-3.26 Å[150] and no Sc compound is known exhibiting a face-sharing arrangement. A complete segregation of Sc in *2a* sites would give a composition of $BaTi_{⅔}Sc_{⅓}O_{3-\delta}$: here, any further substitution would result in the hexagonal-to-cubic phase transformation. The results of the Rietveld analyses of the dry samples are summarised in *tables 5.1*.

Tables 5.1 Summary of the results obtained from Rietveld analysis of NPD data for (*a.*) dry BTS⅙ and BTS20 in the 6H hexagonal structure at RT (space group: $P6_3/mmc$); (*b.*) dry BTS50 and BTS70 in the cubic crystal system at RT (space group: $Pm\bar{3}m$).

a.

	BTS⅙	**BTS20**
a (Å)	5.7573(1)	5.7699(1)
c (Å)	14.0949(2)	14.1408(3)
Volume (Å^3)	404.60(1)	407.70(1)
Ba(1) *2b* (0, 0, ¼)		
U_{iso} (Å^2)	0.0022(4)	0.0047(7)
Ba(2) *4f* (⅓, ⅔, z)	0.09550(11)	0.09662(14)
U_{iso} (Å^2)	0.0086(3)	0.0075(6)
Sc / Ti(1) *2a* (0, 0, 0)		
Occ. factor	0.364(2) / 0.636(2)	0.526(3) / 0.474(3)
U_{iso} (Å^2)	0.0003(6)	0.0046(8)
Ti(2) / Sc *4f* (⅓, ⅔, z)	0.84839(14)	0.84684(23)
Occ. factor	0.990(1) / 0.010(1)	0.963(2) / 0.037(2)
U_{iso} (Å^2)	0.0045(4)	0.0045
O(1) *6h* (x, y, ¼)	0.51770(12)	0.51626(21)
	0.03535(24)	0.03242(43)
Occ. factor	0.938(3)	0.899(5)
U_{iso} (Å^2)	0.0109(3)	0.0145(5)
O(2) *12k* (x, y, z)	0.83275(8)	0.83126(13)
	0.66548(17)	0.66244(27)
	0.08219(4)	0.08241(6)
U_{iso} (Å^2)	0.0066(2)	0.0066(2)
R_{wp} (%)	6.20	5.88
R_{F^2} (%)	17.72	4.33

b.

	BTS50	**BTS70**
a (Å)	4.13136(3)	4.15663(3)
Volume (Å^3)	70.515(1)	71.816(1)
Ba *1b* (½, ½, ½)		
$U_{11} = U_{22} = U_{33}$ (Å^2)	0.0132(2)	0.0200(4)
$U_{12} = U_{13} = U_{23}$ (Å^2)	0	0
Sc / Ti *1a* (0, 0, 0)		
Occ. factor	0.491(1) / 0.509(1)	0.661(3) / 0.339(3)
$U_{11} = U_{22} = U_{33}$ (Å^2)	0.0015(2)	0.0097(4)
$U_{12} = U_{13} = U_{23}$ (Å^2)	0	0
O *3d* (½, 0, 0)		
Occ. factor	0.918	0.883
U_{11} (Å^2)	0.0116(4)	0.0172(8)
$U_{22} = U_{33}$ (Å^2)	0.0185(3)	0.0291(5)
$U_{12} = U_{13} = U_{23}$ (Å^2)	0	0
R_{wp} (%)	5.43	7.46
R_{F^2} (%)	23.57	15.50

5.4 Hydration/dehydration

Experimental details about hydration and dehydration of the BTS samples can be found in papers I[123] and II[124], and in section *4.1.4*. *In situ* and *ex situ* TG experiments are outlined in sections *4.2.1.2* and *4.2.4*, respectively. *Table 5.2* summarises the results of *ex situ* thermogravimetric experiments. Experimental mass losses for the four samples are reported alongside the theoretical ones corresponding to the target stoichiometries, that is the ones intended at the moment of the syntheses. For these ceramic samples, mass losses thermograms are sigmoid curves that are dependent in their onset temperatures of dehydration on the heating rate, when sample mass, particles size and sample holder are comparable. Slower heating rates shift the onset temperature of dehydration to lower temperatures.

Table 5.2 Summary of the results of *ex situ* thermogravimetric analyses (RT to 1000 °C) and comparison to the theoretical mass losses for the target compositions of the samples.

Sample	*Theoretical mass loss (target compositions) (%)*	*Experimental mass loss (%)*
BTS⅙	0.64	0.50
BTS20	0.77	0.90
BTS50	1.94	1.80
BTS70	2.72	2.80

With saturated phases, that is when water fills all the available oxygen vacancies, the discrepancies between theoretical and experimental values for the mass losses are indicative of the same differences between the intended stoichiometries and the actual ones. For these systems, and especially for the cubic types, when analysed with the Rietveld method, serial parametric correlations are important. Occupancies of the Sc/Ti sites and of the oxygen sites can't be independently calculated so the process of refining metal and oxygen sites parameters crucially rely on the information provided by the gravimetric method. Mass losses are therefore a measure of the occupancy of the oxygen site when materials are dry. More accurate occupancies of the metal sites can so be obtained by fixing the occupancy of the oxygen sites to the values suggested by TG[123,124].

The introduction of protonic defects in the structure of acceptor-doped perovskites is generally accompanied by an expansion of the unit cell[66–68,91,151], a phenomenon that is critical to the mechanical stability and, therefore, to the lifetime of any device making use of such ceramic phases. This *chemical expansion* can readily be noticed from the comparison of the X-ray diffractograms of vacuum dried (VD) and hydrated (H) phases. The shift of all Bragg peaks to lower angles is an immediate indication of the success of the hydration procedure as, from the application of Bragg's law (*eq. 4.1*), to higher angles correspond larger unit cells (*fig. 5.13*).

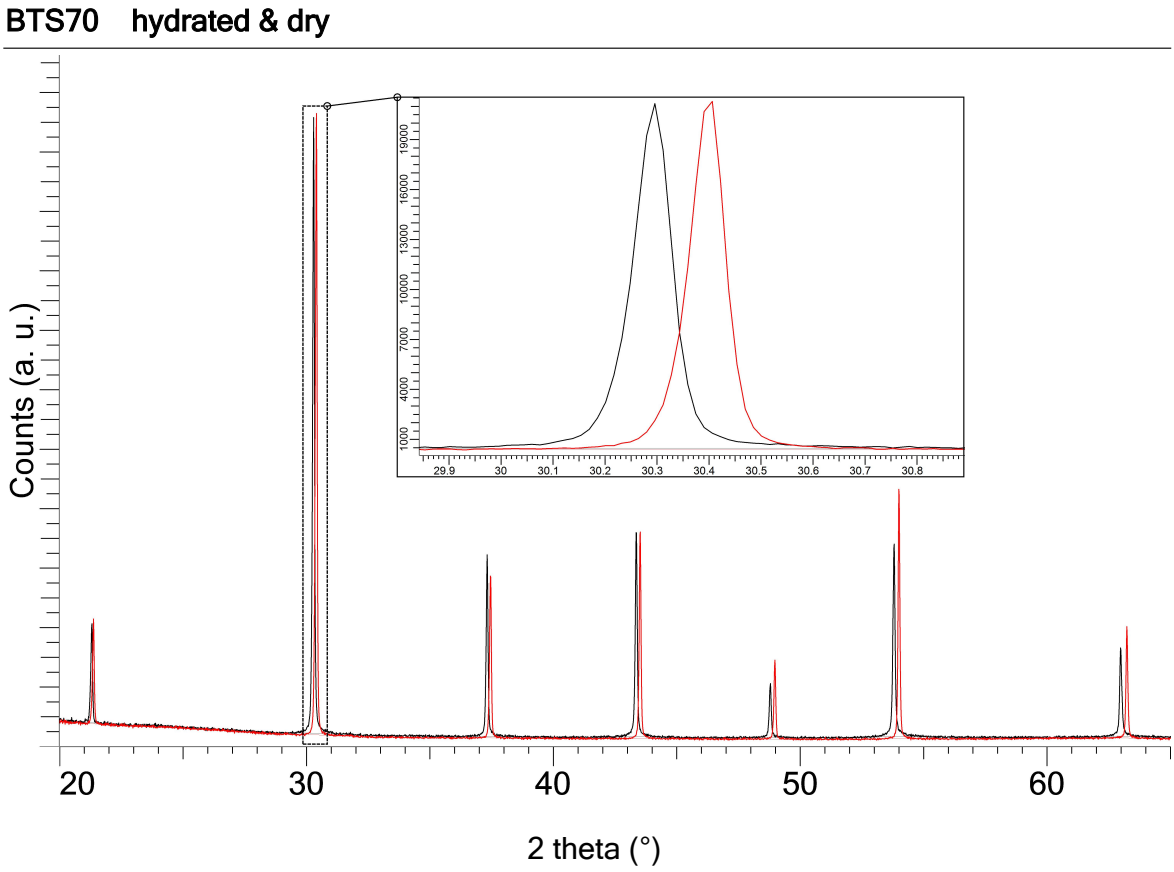

Fig. 5.13 Diffractograms of BTS70 samples, hydrated (in black) and dry (in red), collected with the laboratory diffractometer, a Bruker AXS D8 Advance. The detail in inset shows the separation in 2ϑ angle of the two (110) peaks.

The observation of a very small chemical expansion in BTS50[14] prompted the investigation of the structural response in the cubic materials upon hydration. This was done by means of a simultaneous *in situ* neutron powder thermodiffractometric and thermogravimetric experiment during dehydration[124]. The evolution of the cubic cell parameters of BTS50 and BTS70 with temperature is shown in *fig. 5.14 a* and *b*. The correlation between oxygen site occupancies and hydration levels in the materials allowed the calculation of the size of oxygen vacancies from structural and thermodynamic data[124].

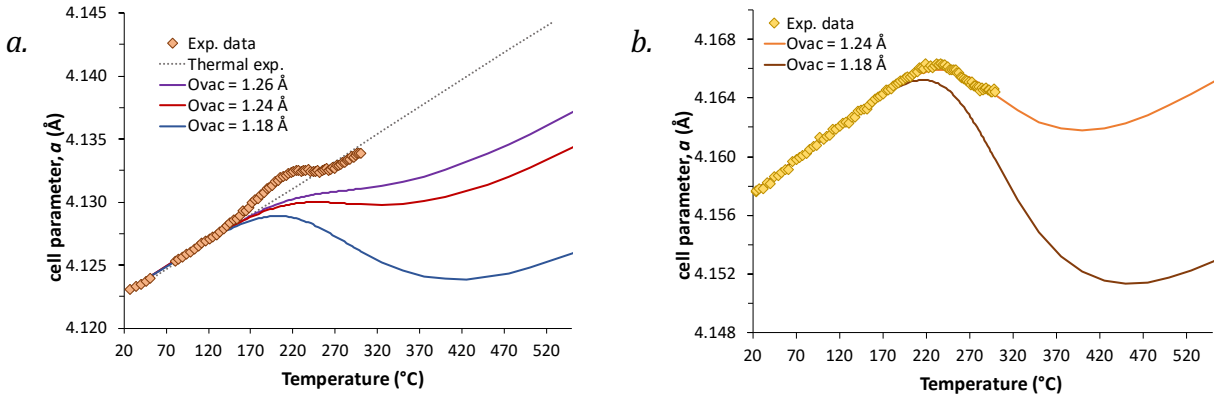

Fig. 5.14 Evolution of the lattice parameters during thermally induced dehydration for BTS50 (*a.*) and BTS70 (*b.*). The dotted line in figure *a.* shows the modelled evolution of the hydrated material solely by thermal expansion. The modelled curves of chemical expansion are shown by the solid lines, with the respective oxygen vacancy size as in the legend.

The chemical expansion of BTS50 (in this case a chemical contraction due to the dehydration of the samples) was found to be very small in magnitude also by *in situ* experiments. For BTS70 the behaviour was found to be more conventional in nature as an expansion of the unit cell is followed by a contraction due to the evolution of water away from the structure. This indicates that the size difference between the $v_O^{\bullet\bullet}$ and the protonic defects is smaller in BTS50. Both systems are very heavily substituted and support a high level of oxygen deficiency when dry. Oxygen vacancy-to-vacancy correlations and clustering of vacancies are therefore a concrete possibility that could also be associated with localised B-site ordering. The cell parameter in the dry state will, thus, be influenced as the magnitude of the chemical expansion linked to hydration of the vacancies will.

5.5 Local environments and short-range ordering

Pair Distribution Functions analysis

The information gathered so far indicates that local environments play a crucial role for proton transport and structural dynamics, especially in the cubic phases, as differences in proton conductivity and in the hydration/dehydration behaviour are hardly explained solely by the number of protonic defects in the hydrated materials and vacancies in the dried ones. By employing the Reverse Monte Carlo (RMC) method for the analysis of total scattering data, the local ordering was probed in order to bring clarity on the matter. The analysis provided enhanced structural models for hexagonal and cubic types within the BTS system. Especially in the cubic samples, in fact, the refined models obtained from Rietveld analysis of the Bragg scattering do not reflect at all the reality of the materials as local distortions are not considered and yet characteristic of these systems.

The information extracted from the analysis of the pair distribution functions (PDF) in dry samples confirms the previous observations on the hexagonal system and provides new insight into the structural disorder of cubic types. In hexagonal 6H BTS20, the segregation of Sc in the site *2a* and of Ti in the *4f* is clearly visible from the partial distributions (see paper III). The shortest distance of 2.74 Å is, in fact, displayed only by the $g_{TiTi}(r)$, in agreement with the separation distance extracted from Rietveld refinement of NPD data of 2.755(7) Å[123], for the Ti–Ti pair in the dimeric Ti_2O_9 arrangement. Distributions centred at 3.92 Å for $g_{TiTi}(r)$, and at 3.96 for $g_{ScTi}(r)$ indicate the *2a* to *4f* separations for, respectively, the Ti–Ti pair and the Sc–Ti pair. The first distribution of Sc–Sc distances can only be found centred at 5.78 Å, coinciding with the lattice parameter *a*. The second distribution is found at an average distance of 7.08 Å, matching the cell parameter *c*/2. The analysis of the coordination environments of Sc and Ti(1) confirms that vacancies are found around Ti(2) as the coordination positions are saturated (*fig. 5.15*).

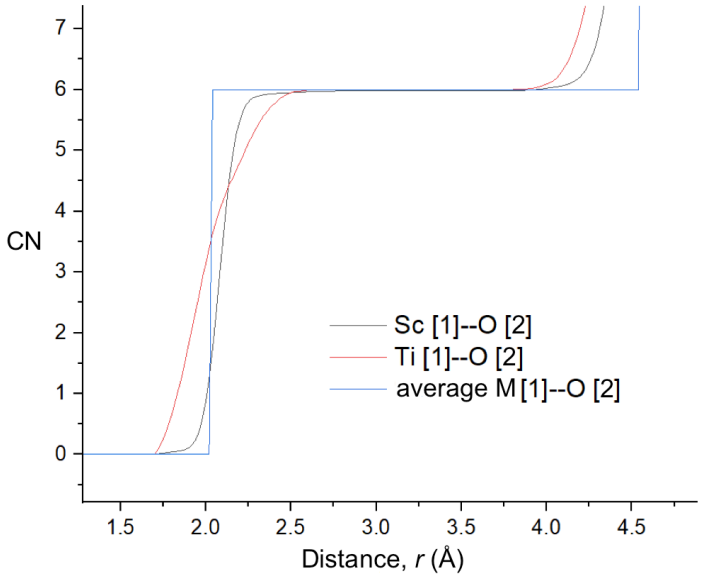

Fig. 5.15 Coordination numbers for Sc (grey) and Ti (red) in BTS20. In blue the average CN of the metal at the *2a* site.

In the cubic samples, BTS50 and BTS70, it is found that the distances involving Ti are distributed around multiple centres (*fig. 5.16 a* and *b*), indicating a specific ordering for the ion. In particular, from the analysis of Ti–O distributions, it is clear that a regular octahedron cannot describe the reality of the coordination environment of Ti. A severe off-centre displacement of the coordinating ion and its repercussions on the ligands must be considered to describe more precisely these materials.

a.

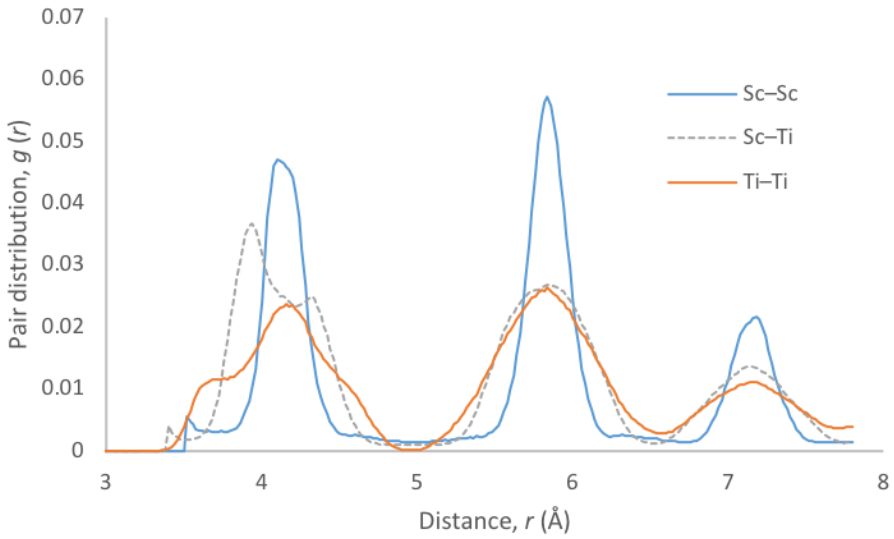

b.

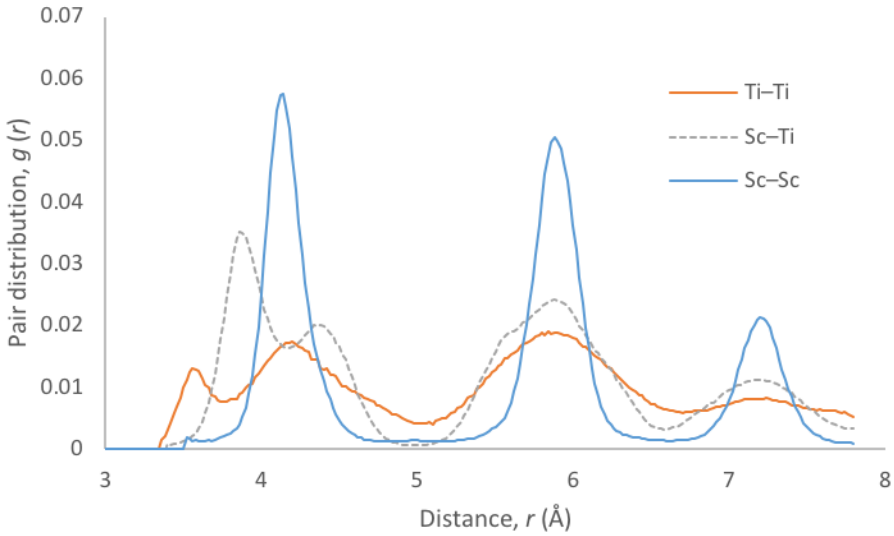

Fig. 5.16 Partial distribution functions $g_{ScSc}(r)$ (solid orange), $g_{ScTi}(r)$ (dashed blue), and $g_{TiTi}(r)$ (solid grey) for BTS50 (*a.*) and BTS70 (*b.*).

The hypothesis of vacancy-vacancy interactions in these systems finds evidence in the study of the local environments. As PDF data show, it is not the larger number of vacancies that can be found in BTS70 that favours stronger interactions but the interplay between metal and oxygen sublattices. The distributions of Ti–O pairs indicate that higher Sc-substitution levels in this system promote the distinct grouping of Ti–O bond lengths (see paper III), which ultimately leads to materials that are less able to accommodate lattice strains and therefore more rigid, for which the chemical expansion associated to the filling of oxygen vacancies with protonic defects has a larger impact.

In BTS50, the broad range of Ti–O bond lengths would more easily favour vacancy-vacancy interactions and Sc^{3+} would facilitate the pairing by contributing some of its electron density, as the BVS value for its valence leans towards exceeding 3. The interplay of titanium and oxygen sublattices produces a material that is able to accommodate lattice strains to a higher degree, eventually resulting in its surprising behaviour during hydration/dehydration cycles, where the unit cell undergoes very little volume changes. On the contrary, in fluorite-structured materials such as Y- and Sc-doped zirconia vacancy-vacancy interactions are minimised by vacancy ordering and those interactions are not influenced by the concentration nor the nature of the dopant species[152,153].

Spectroscopy with light and neutrons

Local environments were studied also with spectroscopic techniques. The Raman spectra provided information about the lattice vibrational modes. For the hexagonal samples, BTS⅙ and BTS20, characteristic Raman modes of hexagonal perovskite oxides and of hexagonal $BaTiO_3$ were observed. Alongside, additional features suggested that the local disorder due to the Sc doping induces Raman-active modes. The same is evident in the cubic samples, BTS50 and BTS70. The symmetry breaking at the local scale was confirmed by the presence of vibrational bands that should be forbidden in crystal structures of perfect cubic symmetry.

Infrared spectroscopy (IR) and inelastic neutron scattering (INS) experiments provided information about the O–H vibrational modes, wag (δ) and stretch (ν). Cubic samples were characterised by a broad δ(OH) vibrational band, a feature that is attributed in this family of compounds to a distribution in the strength of the hydrogen bonds. By comparison, the spectra of the hexagonal samples showed several well-defined peaks over the δ(OH) region that suggested the presence of at least three distinct proton environments. The overall blue-shift of the δ(OH) band and associated red-shift of the ν(OH) band indicated that stronger hydrogen-bonding can be found in the hexagonal rather than in the cubic phase, agreeing with earlier investigations[138].

The three different proton environments (see paper IV) were characterised as configurations typical of hexagonal (inter-octahedral OH···O hydrogen bond, the most stable) and cubic structures (intra-octahedral OH···O hydrogen bond). The description of these configurations was supported by DFT modelling and provided an evidence to the 3-steps migration pathway for protons that was hypothesised in paper I[123].

The presence of low energy shoulders in the INS spectra of BTS50 suggested that remnants of hexagonal-type hydrogen bond configurations may be still present in Ti clusters in the cubic samples. These configurations are unfavourable for proton transport, as conductivity data of hexagonal BTS20 showed[15]. They would originate from Ti-rich domains, more likely in BTS50 compared to BTS70, and would explain the poorer proton conducting properties associated to lower Sc content in the cubic regime[15].

5.6 Summary

Hexagonal and cubic samples in the $BaTi_{1-x}Sc_xO_{3-x/2}$ system with x = ⅙, 20, 50 and 70 were synthesised *via* solid-state reaction and characterised with a combination of gravimetric, scattering and spectroscopic methods. The hexagonal types are characterised by ordering of Sc and Ti cations, oxygen vacancies and protons. The ordering of cations results from Sc doping. This ordering, suggested by XRD[15] studies and indicated by NPD[123], was confirmed by the RMC modelling of total scattering data. Sc levels are also responsible for the structural transformation to cubic types with increasing Sc concentration, as well suggested by the preliminary results of the synthetic work on BTS⅓. Oxygen vacancies are found within the plane of the faces shared by $TiO_{6-\delta}$ polyhedra and protons are bonded to the corresponding oxygens in hydrated materials. Evidence for this proton siting was provided by INS and supported by DFT calculations. They indicated the presence of other stable proton configurations that would demonstrate the anisotropic 3-step migration path hypothesised in paper I[123]. In the hexagonal regime, lower Sc levels are associated to stronger hydrogen bonds that impacts negatively on proton migration.

The cubic types are characterised by disorder of cations, oxygen vacancies and protons, at least to a first approximation. The indication is that extended and local environments are different in these materials. A simplified model was used for the interpretation of Bragg diffraction data, where unit cells of cubic symmetry provided the first descriptions. No sign of long-range ordering was found but the observation of appreciable diffuse scattering in hydrated and dry BTS70 was indicative of local ordering. The RMC modelling of total scattering data provided the first evidence of that, observed in the PDF (see paper III). The ordering concerns Ti ions, that are off-centred from the expected crystal site based on cubic symmetry. Evidence of local symmetry-breaking effects were also found in the Raman spectra (see paper IV). This ordering is a direct consequence of Sc doping and impacts the oxygen sublattice as well. In hydrated materials, to lower Sc levels correspond smaller differences in size between protonic defects and the oxygen vacancies that form upon dehydration. In dry materials, vacancy-vacancy interactions are minimised by the interplay between metal and oxygen sublattices, with surprising macroscopic effects. Higher Sc levels, that is a larger amount of vacancies, promote the distinct grouping of Ti–O bond lengths. In BTS50 the Ti ordering is less pronounced and results in a broader range of Ti–O distances which makes the material undergo very small volume changes upon hydration/dehydration cycles. A more pronounced ordering in BTS70 produces a bimodal distribution of Ti–O bond lengths and a more conventional behaviour. Protons sites are characterised by a higher multiplicity in cubic materials, favourable for proton transport. Spectroscopy studies suggested the presence of remnants of hexagonal-type hydrogen bond configurations in Ti clusters. These are more likely in BTS50, hindering proton migration and resulting in the poorer proton conductivity along with a stronger hydrogen bond that weakens with increasing Sc levels.

Chapter 6
Other investigated systems

6.1 Introduction

The development of new electrolyte materials is critical for reducing the operation temperature and related cost of the potential devices that would make use of ceramic proton conductors. As discussed in chapter 3, most of the materials for which high temperature proton conduction is observed have crystal structures of the perovskite type or that derive from that or from fluorite or pyrochlore structures. These structures have in common a sublattice of oxide ions, more or less regular, constituting the framework that hosts proton transport. The symmetry, basicity and dynamics of such framework are influenced by the lattice cations and play a major role in determining the effects of defects interactions that favour or disfavour proton migration.

A series of compositions within the relevant structure types were therefore investigated with respect to the doping strategy, the synthesis, and their interaction with water vapour. One simple observation useful for qualitatively discerning proton conducting properties in potential candidate phases concerns, in fact, their water uptake. That is the ability of an oxide system to fill its oxygen vacancies as illustrated by *equilibrium 2.1*. The following sections report and discuss the results obtained from the investigation of those systems. Details concerning the synthesis and hydration of the phases are summarised in sections *4.1.1*, *4.1.2* and *4.1.4*.

6.2 Barium zirconate systems

Ceramic proton conducting electrolytes are the benchmark among acceptor-doped perovskite-structured materials. $BaZrO_3$-based systems are considered the most promising ones[98], with Y-doped materials (BZY) characterised by good chemical stability[44,154] and the highest bulk proton conductivity[44,147,155–157]. This system suffers, though, from drawbacks caused by its highly resistive grain boundaries[24,68,158] that hinder proton transport. These are being addressed by optimising fabrication methods[96,157,159] and grain surface processing[97]. Beside the microstructure and morphology of the materials, proton transport is also crucially dependent on the nature of the doping species[160]. In general, large lattice constants and high crystal symmetry seem to favour proton mobility[24], hence, the ionic radius of the dopant[160–162] (M), its Pearson hardness[163], and the nature of the M–O bond[51,162], altogether play an important role. Since local

structural features (local ordering and symmetry, defects interaction) impact on proton transport, determining the structural environment of the proton itself is necessary for a thorough understanding of its transport mechanism. The determination of the preferred locations for the proton site in proton conducting perovskites has, therefore, been the object of several neutron diffraction studies[49,53,91,123,164–168]. Protons prefer a *24k* crystal site, located around the oxygen, with O–H distances of about 1.0 Å.

The aim of this study was to elucidate the proton structural environment in zirconate perovskites and to understand how different dopants influence it. A series of samples were synthesised, where the host $BaZrO_3$ phase was doped with five different trivalent cations, Sc^{3+}, Ga^{3+}, Y^{3+}, In^{3+}, Yb^{3+}. In BZY materials the highest proton conductivity is measured for dopant molar concentration of 20%[169,170], therefore the same doping level was chosen for all compositions. The structural features of the deuterated phases were studied with neutron powder diffraction experiments.

6.2.1 Results and discussion

Laboratory XRD analyses indicated phases with impurity levels below the detection limit of the technique. Thermogravimetic data indicated hydration levels close to saturation, above 90%. With NPD data, attempts to locate the D position by difference density maps and by refining the *24k* and *12h* positions (*fig. 6.1*) were, though, unsuccessful. The refinements were insensitive to the H/D position most likely because of the partial exchange of deuterons with protons that occurred during storage, and transportation of the samples to the neutron facility ($b_{Coh,\,D}$ = 6.671 fm, $b_{Coh,\,H}$ = –3.7406 fm). The results of the Rietveld analyses are summarised in *table 6.1*. Fractional occupancies for the *1a* site were fixed to the intended stoichiometry for the samples doped with Ga and Y because of the similar neutron scattering lengths that these elements exhibit with respect to Zr (b_{Ga} = 7.288 fm, b_{Y} = 7.75 fm, b_{Zr} = 7.16 fm). In such cases diffraction experiments making use of neutrons are not suited for probing the occupancies of shared crystal sites.

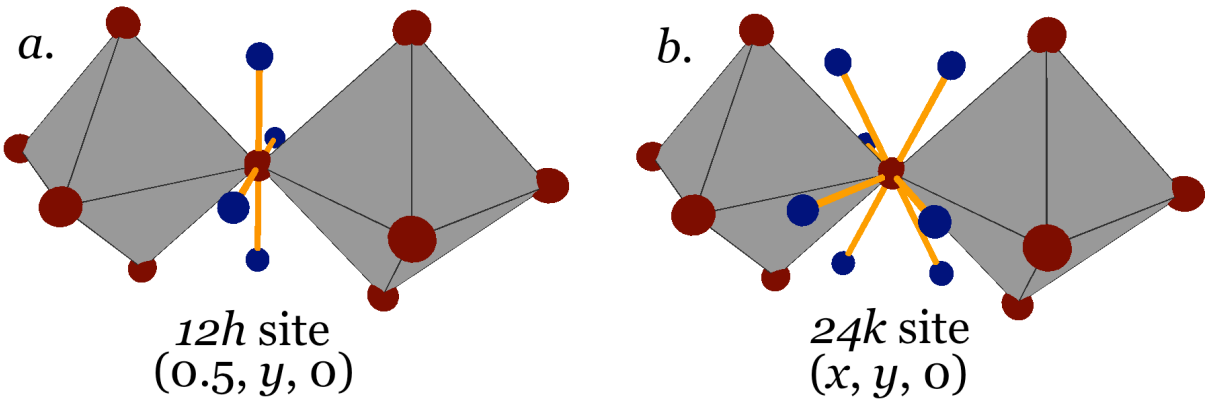

Fig. 6.1 Representation of the *12h* (*a.*) and *24k* (*b.*) structural sites for protons (deuterons) in cubic $Pm\bar{3}m$ perovskites.

The results showed that changes in the lattice parameter of doped $BaZrO_3$ are not correlated to the size of the dopant ion[161,171], i.e. a larger effective size does not necessarily mean a larger unit cell (*fig. 6.2 a*). Along the substitutional series, for example with In[95], Y[52] and Yb[140,172], with increasing dopant concentration larger unit cells are observed but Sc doping has a small impact on $BaZrO_3$. The lattice parameter of the undoped material, 4.1931(1)-4.194(1) Å[52,173], is similar to that of the as-prepared doped phases, being 4.194(1) Å with 6 mol% Sc[174], 4.19279(6)-4.1952(1) Å with 10 mol% Sc[148,160], 4.1883(1) Å and 4.1906(2) Å respectively for 19 mol% Sc dry and hydrated[171]. The same can't be said when doping $BaTiO_3$. The cubic phase of the undoped material exhibits a lattice parameter of 4.000(1) Å[175,176], while the pseudo-cubic lattice constants of the tetragonal 5 mol% Sc is 4.019(1)[177], of the hexagonal 10 mol% is 4.065(1) Å[15], of the hexagonal 20 mol% is 4.084(1) Å[15], and the cubic 50 mol% and 70 mol% have lattice constants of 4.1343(1) Å[14] and 4.1673(1) Å[15] respectively, clearly indicating the expansion of the unit cell with increasing Sc content.

Table 6.1 Summary of the results obtained from Rietveld analysis of NPD data for $BaZr_{0.8}M_{0.2}O_3$ in the cubic crystal system at 5 K (space group: $Pm\bar{3}m$).

	Ga	***Sc***	***In***	***Yb***	***Y***
a (Å)	4.19070(5)	4.19076(5)	4.19788(5)	4.22001(11)	4.21728(15)
Volume (Å³)	73.597(3)	73.600(3)	73.976(2)	75.152(6)	75.006(8)
Ba *1b* (½, ½, ½)					
$U_{11} = U_{22} = U_{33}$ (Å²)	0.0003(1)	0.0033(1)	0.0026(1)	0.0031(1)	0.0043(1)
$U_{12} = U_{13} = U_{23}$ (Å²)	0	0	0	0	0
M / Zr *1a* (0, 0, 0)					
Occ. factor	0.2 / 0.8	0.878(3) / 0.122(3)	0.821(5) / 0.179(5)	0.792(6) / 0.208(6)	0.2 / 0.8
$U_{11} = U_{22} = U_{33}$ (Å²)	0.0015(1)	0.0037(1)	0.0020(1)	0.0036(1)	0.0027(1)
$U_{12} = U_{13} = U_{23}$ (Å²)	0	0	0	0	0
O *3d* (½, 0, 0)					
U_{11} (Å²)	0.0022(2)	0.0019(1)	0.0017(1)	0.0021(2)	0.0029(3)
$U_{22} = U_{33}$ (Å²)	0.0052(1)	0.0077(1)	0.0090(1)	0.0135(2)	0.0160(2)
$U_{12} = U_{13} = U_{23}$ (Å²)	0	0	0	0	0
R_{wp} (%)	1.91	1.55	1.52	1.90	2.25
R_F^2 (%)	4.27	5.31	5.09	9.02	9.85

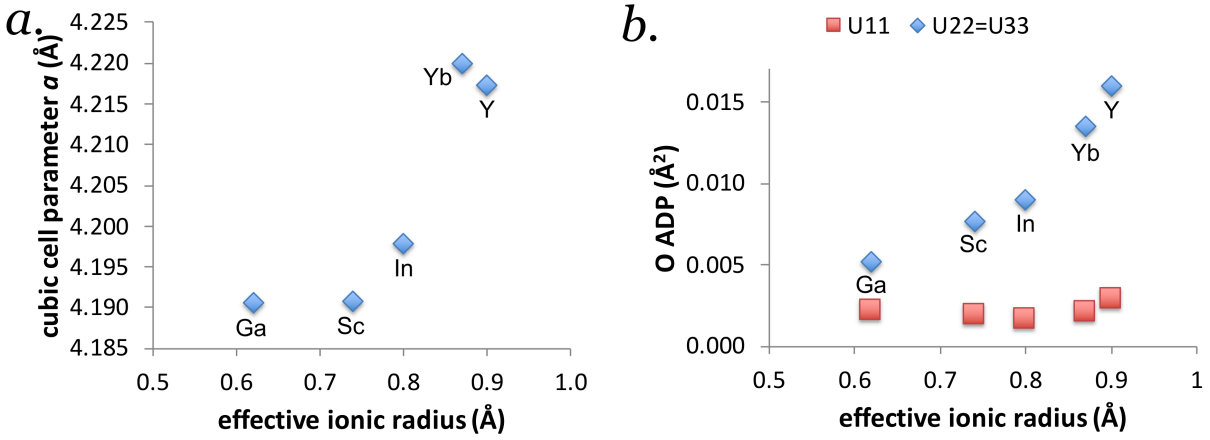

Fig. 6.2 Cubic cell parameter (*a.*) and O site displacement parameter (*b.*) as a function of the ionic radius of the dopant ion.

The Rietveld analysis suggested that a correlation exists between the size of the ion (in an octahedral environment) and the ADP of the oxygen site (*fig. 6.2 b*). U_{11} is affected to a lesser extent than U_{22} (U_{33}) for which a clear trend can be observed. This indicated that the strain produced on the lattice by the increasing size mismatch between Zr^{4+} and the trivalent dopant ion is relieved by distortions in the oxygen sublattice. The volume occupied by oxygen becomes larger and oblate along the ⟨100⟩ direction and expanding in the (200) plane. High local disorder is characteristic of the materials with the highest bulk conductivity, as shown by EXAFS studies on 10 mol% M-doped $BaZrO_3$ (with M = Ga^{3+}, Gd^{3+}, In^{3+}, Sc^{3+}, Y^{3+})[51], 6 and 15 mol% Y-doped $BaZrO_3$[52], and 2-75 mol% In-doped $BaZrO_3$[178]. The same trend can be observed in the cubic regime of the BTS system where to a higher Sc content correspond larger ADPs of the oxygen site, especially U_{22} (U_{33}) (see *tab. 5.1*). The result of these refinements agreed with previous observations and it was an indication of the role of the oxygen sublattice dynamics for fast proton transport.

6.2.2 Conclusions

Acceptor-doped $BaZrO_3$ samples were synthesised by a wet chemical method, pre-characterised by XRD and TG analyses and structurally characterised by Rietveld analysis of neutron powder diffraction data collected at 5 K. The main goal of the study was not attained since partial deuteration of the materials frustrated all efforts to locate the proton site. The recommendation is that deuteration techniques and transport of the materials to the neutron facility should be planned carefully when exchange is likely.

The present results agreed with previous studies, showing that the lattice parameter is not a function of the ionic radius of the dopant and that Sc has a smaller impact on the size of the unit cell. A correlation is found with the oxygen site displacement paraments. Results indicated that larger ions contribute to increased local disorder of the oxygen sublattice where thermal ellipsoids are oblate along the ⟨100⟩ direction and expand in the (200) plane.

6.3 Ruddlesden-Popper systems

Ternary compounds with the general formula $A_{n+1}B_nX_{3n+1}$ have attracted attention in the last decades because of their chemical and physical properties, such as catalytic activity[179], ferroelectricity[180], colossal magnetoresistance[181], and potential for high temperature superconductivity[182,183]. Alternating perovskite-like, corner-sharing BO_6 sheets and rock salt-like AO sheets characterise such phases, which show a layered structure. Such a structure is interesting because it allows a wide range of chemical compositions, to yield a versatile class of compounds. These include cell elements for SOFC, thanks to the ionic and mixed ionic-electronic conducting properties, and substantially lower thermal expansion coefficients with respect to disordered perovskites, especially in Ni- and Cu-containing phases[184].

It is intriguing that some of these phases intercalate water molecules, forming layers inside the rock-salt type block through which protonic conduction can occur (*fig. 6.3*). Water intercalation produces layers of water/hydroxide/oxonium species and leaves the existing layers practically intact: it produces elongation in the layer-stacking direction (*c* axis) and affects the *ab*-plane only slightly. On the other hand, the formation of water-containing layers impacts on the stability of the original phase. In general, the most important factors influencing the reactivity with water are the size of the A cations and the oxygen content of the phase. Higher reactivity is observed for phases with progressively larger A cations and smaller oxygen content.

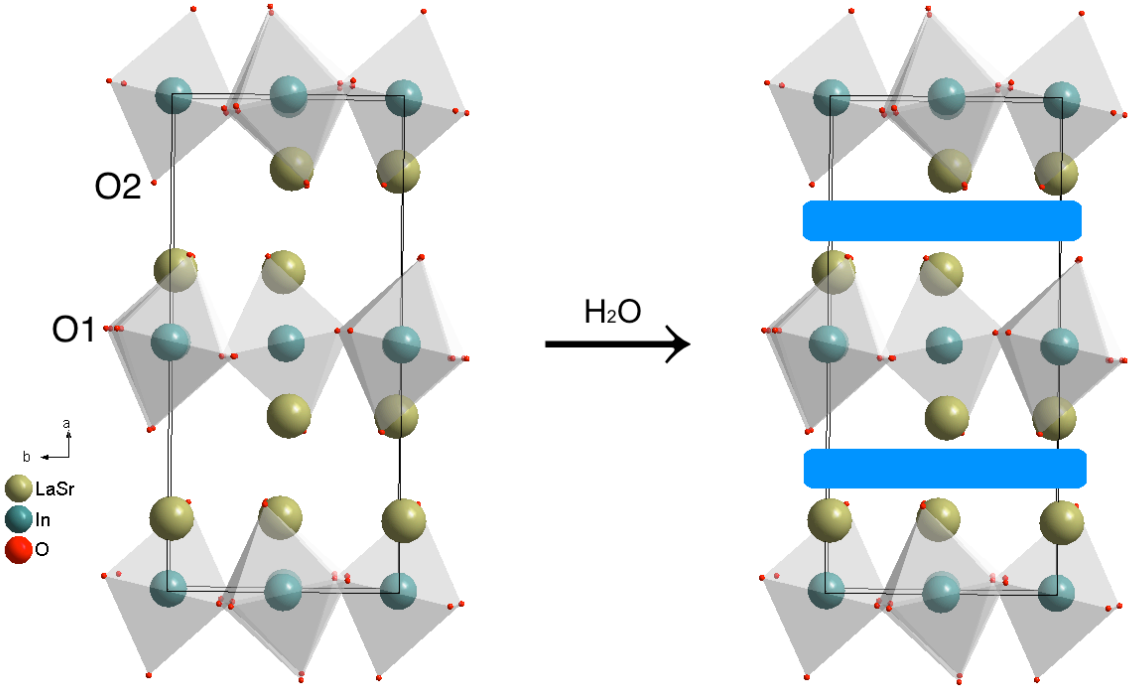

Fig. 6.3 Representation of the crystal structure of $LaSrInO_4$, a Ruddlesden-Popper phase, alternating perovskite (with tilted, corner-sharing InO_6 octahedra) and rock-salt layers. Exposure to moist atmosphere produces its water derivative phase, where intercalated water layers can most likely be found in between the rock-salt sheets.

Oxide ion conductors represent a relevant class of materials when exploring novel proton conducting phases. They are characterised by the presence of oxygen vacancies and favourable dynamics of the oxygen sublattice for ionic transport, features that are advantageous also for protonic conduction. Further, Sr doped $LaMnO_3$ is usually employed as cathode material for solid oxide fuel cells (SOFC)[185–187] and other perovskite-type cathode materials are mixed ionic and electronic conductors (MIEC) with compositions (La, Sr)(Co, Fe)$O_{3-\delta}$[184,188].

Drawing inspiration from studies on n = 2 compounds[83,189,190], a series of compositions with n = 1 was investigated in order to further understand the factors influencing the reactivity with water and to explore the electrochemical properties. In the attempted compositions (*tab. 6.2*) the A-site is hypothetically shared by a lanthanide and

a rare-earth cation. These were chosen on the basis of similarity in ionic radius in a 9-fold coordination, exception made for Mg^{2+} that was chosen in order to test the hypothesis since no example of that coordination chemistry is known for the ion. While Sr- and Ba-containing phases are known the Ca-containing ones are not. La was chosen because the perovskite oxide $LaGaO_3$ doped with Sr at the A-site and Mg at the B-site is reported to exhibit high ionic conductivity among oxide ion conductors and is stable over a wide range of oxygen partial pressures[191]. Pr was chosen for the possibility to introduce mixed conducting properties[192] given its variable oxidation state, for instance in the oxide Pr_6O_{11}. The B-site is occupied by Sc or In, for which Ruddlesden-Popper phases are known to exist.

The successful layered perovskite phases were further investigated by acceptor-doping the A-site (La, Pr) with additional 10 mol% of the same alkaline-earth cation with which they share the crystal site, in order to introduce oxygen vacancies while keeping the B-site (Sc, In) unaltered. Hence four families of compounds were studied, from the point of view of the success of the solid-state reaction, and from that of their stability towards water vapour and subsequent water uptake.

6.3.1 Results and discussion

Synthesis and structural characterisation

Table 6.2 shows the results of the syntheses. For the La-based compositions, it is noticeable that only Sr^{2+} and Ba^{2+} are able to share its crystal site in the rock-salt layer as Ca^{2+} is smaller (1.22 Å, 1.31 Å, 1.47 Å, 1.18 Å, respectively for the 9-fold coordinated La^{3+}, Sr^{2+}, Ba^{2+} and Ca^{2+}). Even though Ca^{2+} matches the size to Pr^{3+} the desired phases did not form. In this case matching ionic radii is not a reliable strategy for predicting the stability of a phase. Indeed Ca^{2+} was successfully employed as a dopant for the La site in La_2CuO_4[193,194] up to 15% and in La_2NiO_4 up to 30 mol%[195]. The authors noted that the stability of the phases decreases with increasing Ca content and that further substitutions did not yield stable phases. This was explained[193] by the repulsive interaction between oxygens becoming stronger with the decrease of the average cation radius at the A-site. As in framework perovskites, a smaller A-site cation is also associated with octahedral tilting[80] that lowers the crystal symmetry. Further, the Goldschmidt tolerance factor decreases with increasing Ca content, with the lowest value of 0.8834 for $La_{1.7}Ca_{0.3}NiO_{4+\delta}$[195]. The comparison of the values of *t* calculated for the investigated phases (0.8591 for $LaCaScO_4$; 0.8357 for $LaCaInO_4$; 0.8525 for $PrCaScO_4$; 0.8292 for $PrCaInO_4$) suggested that those could not be stable. Still, the concentration of Ca can be higher in the nickelate phases than in the cuprate ones, suggesting that the size of the B-site cation plays a role too (0.69 Å *vs.* 0.73 Å in a 6-fold coordination). The desired Ba-containing phases were not pure as the larger A-site cation favoured the formation of a mixture of layered phases with n = 1 and 2, especially with Sc at the B-site confirming that size matching on both sites is important for phase stability. Pr-containing phases were found to be very sensitive to ambient atmosphere, changing colour upon grinding from black to

burnt sienna. As expected, Mg-containing phases did not form. The focus was put on the samples $LaSrScO_4$ and $LaSrInO_4$.

Table 6.2 Summary of the syntheses attempted for the compositions with Ruddlesden-Popper layered perovskite structure and the results of the phase analysis performed on the respective samples. Ruddlesden-Popper phases with n =1, 2 are referenced.

Desired phase	***Phase analysis***
$LaMgScO_4$	$LaScO_3$, La_2O_3, MgO
$LaCaScO_4$	$LaScO_3$, La_2O_3, CaO
$LaSrScO_4$	$LaSrScO_4$[196,197], $La_2SrSc_2O_7$[198]
$LaBaScO_4$	$LaBaScO_4$[196], $La_2BaSc_2O_7$[199]
$LaMgInO_4$	$LaInO_3$, MgO, $MgIn_2O_4$
$LaCaInO_4$	$LaInO_3$, CaO
$LaSrInO_4$	$LaSrInO_4$[200,201]
$LaBaInO_4$	$LaBaInO_4$[200], $La_2BaIn_2O_7$[202]
$PrMgScO_4$	$ScPrO_3$, MgO
$PrCaScO_4$	$ScPrO_3$, $PrO_{1.75}$, $CaSc_2O_4$
$PrSrScO_4$	$PrSrScO_4$[197], $Pr_2SrSc_2O_7$[198]
$PrBaScO_4$	unindexed phases
$PrMgInO_4$	MgO, unindexed phases
$PrCaInO_4$	unindexed phases
$PrSrInO_4$	$PrSrInO_4$[200], $SrIn_2O_4$, unindexed phases
$PrBaInO_4$	$Pr_2BaIn_2O_7$[203], unindexed phases

Impurity levels of the layered phase with n = 2 were found in $LaSrScO_4$, 1.05(5) wt% as assessed by Rietveld refinement of X-ray diffraction data. The only phase that withstood HYD1 was $LaSrScO_4$ while the other decomposed. A further 10 mol% of Sr was hence used to replace La and produce the acceptor-doped phase $La_{0.9}Sr_{1.1}ScO_{3.95}$. $LaSrInO_4$ showed a certain stability towards HYD2, meaning that the original phase was obtained again once dehydrated (*fig. 6.4*); an acceptor-doped phase was hence produced, $La_{0.9}Sr_{1.1}InO_{3.95}$. The broadening of the Bragg peaks in the hydrated phase is likely due to the effect of water intercalated between the rock-salt layers[189,190], which produces stacking disorder as layers can slide and shift from their position. *Tables 6.3* and *6.4* summarise the results of the Rietveld analyses of the undoped and acceptor-doped phases.

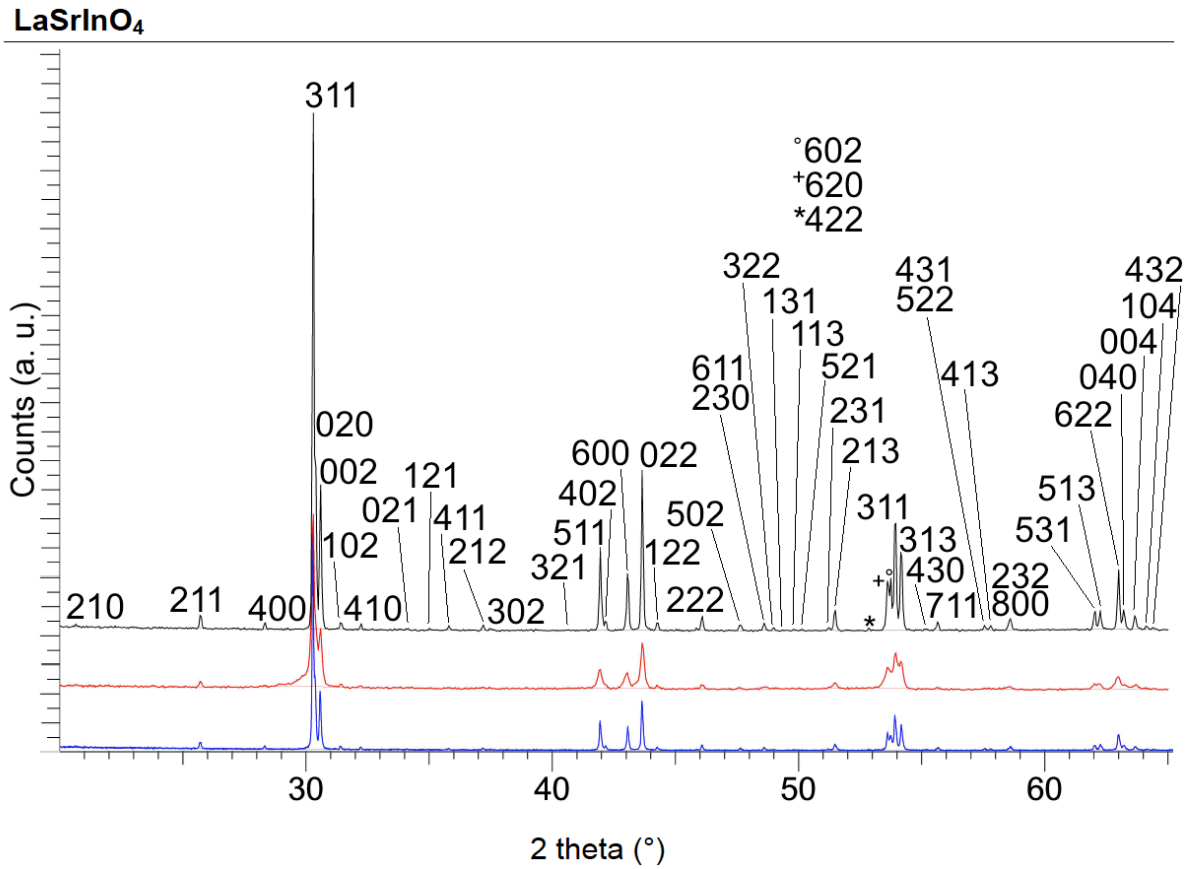

Fig. 6.4 Diffraction patterns relative to $LaSrInO_4$. Exposure to moist atmosphere at 200 °C produces broadening of the diffraction peaks (red pattern), while the original phase is formed again upon dehydration (black pattern). The same behaviour can be observed in $LaSrScO_4$ and in the acceptor-doped phases.

Table 6.3 Summary of the results of the Rietveld analysis of XRD data for $LaSrScO_4$ and $La_{0.9}Sr_{1.1}ScO_{3.95}$ in the orthorhombic crystal system at RT (space group: *Pbca*).

	LaSrScO₄	***La$_{0.9}$Sr$_{1.1}$ScO$_{3.95}$***
a (Å)	5.77244(5)	5.77530(5)
b (Å)	5.76400(5)	5.76746(5)
c (Å)	12.49387(7)	12.51288(7)
La / Sr *8c* (*x*, 0, *z*)	0.0135, 0.3566	0.0140, 0.3568
Occ. factor	0.5 / 0.5	0.45 / 0.55
U_{iso} (Å^2)	0.0326(3)	0.0236(2)
Sc *4b* (0, 0, 0)		
U_{iso} (Å^2)	0.0276(7)	0.0222(6)
O1 *8c* (¼, ¼, *z*)	0.0137	0.0163
U_{iso} (Å^2)	0.0489(21)	0.0303(18)
O2 *8c* (*x*, 0, *z*)	0.4429, 0.3280	0.4465, 0.3274
U_{iso} (Å^2)	0.0517(22)	0.0430(19)
R_{wp} (%)	7.46	7.62
R_F^2 (%)	6.47	10.50
χ^2	7.05	5.71

Table 6.4 Summary of the results of the Rietveld analysis of XRD data for $LaSrInO_4$ and $La_{0.9}Sr_{1.1}InO_{3.95}$ in

the orthorhombic crystal system at RT (space group: *Pbca*).

	LaSrInO₄	***La$_{0.9}$Sr$_{1.1}$InO$_{3.95}$***
a (Å)	12.60156(39)	12.62867(16)
b (Å)	5.88421(19)	5.88951(8)
c (Å)	5.84597(19)	5.84812(8)
La / **Sr** *8c* (*x*, *y*, *z*)	0.1459, –0.0169, 0.9723	0.1454, –0.0113, 0.9725
Occ. factor	0.5 / 0.5	0.45 / 0.55
U_{iso} (Å²)	0.0195(4)	0.0199(5)
In *4b* (½, 0, 0)		
U_{iso} (Å²)	0.0166(5)	0.0168(5)
O1 *8c* (*x*, *y*, *z*)	0.0268, 0.2225, 0.2188	0.0285, 0.2266, 0.2161
U_{iso} (Å²)	0.0297(46)	0.0063(36)
O2 *8c* (*x*, *y*, *z*)	0.3236, 0.0819, 0.0260	0.3181, 0.0873, 0.0172
U_{iso} (Å²)	0.0011(28)	0.0096(29)
R_{wp} (%)	11.35	10.95
R_F^2 (%)	8.57	9.44
χ^2	1.35	1.43

All phases were refined in the orthorhombic crystal system and the space group *Pbca*. $LaSrInO_4$ and the related doped phase were reported[200,201] crystallising in the same space group while $LaSrScO_4$ was reported[196,197] crystallising in the space group *Cmca*. Both space groups do accommodate octahedral tilting but the improvement of the fit factors in the refinements when employing the space group *Pbca* justified the use of this description for $LaSrScO_4$ and the novel related doped phase. Indeed, as shown by Patel and co-workers[197], both orthorhombic and tetragonal crystal systems can be used to describe the structure of $LaSrScO_4$ and the choice of structural model ultimately relies on the quality of the fit, with tetragonal models being more precise at higher temperatures. Unit cells are larger in the In-based samples, as expected from the larger ionic radius of In^{3+} with respect to Sc^{3+} (0.80 Å *vs* 0.74 Å, in octahedral environments). An elongation in the layer-stacking direction is observed in the doped phases, while the two smaller dimensions are almost unaffected. Replacing Sr^{2+} for La^{3+} produces larger unit cells (1.31 Å *vs* 1.22 Å, in 9-fold environments), with slightly greater separations between rock-salt layers (within 0.02 Å, with a more significant change in $La_{1-x}Sr_{1+x}InO_{4-\delta}$ samples) and significantly stretches the In–O2 bonds while the Sc–O2 bonds are only slightly affected (*tab. 6.5*).

Table 6.5 Interatomic bond distances and angles of M and O in the investigated phases.

	$LaSrInO_4$	**$La_{0.9}Sr_{1.1}InO_{3.95}$**	**$LaSrScO_4$**	**$La_{0.9}Sr_{1.1}ScO_{3.95}$**
distances				
M–O1 (Å)	2.10(1) ×2	2.08(1) ×2	2.05(1) ×4	2.05(1) ×4
	2.13(1) ×2	2.16(1) ×2		
M–O2 (Å)	2.28(1) ×2	2.36(1) ×2	2.17(1) ×2	2.18(1) ×2
angles				
M–O1–M (°)	157(1)	156(1)	170(1)	169(1)

In–O1 lengths are grouped into two shorter and two longer bonds whereas Sc–O1 are equivalent. In general, acceptor-doping the rock-salt layer distorts the MO_6 octahedra and

an increased tendency for titling is observed since M–O–M angles decrease. In the parent phases InO_6 octahedra are much more tilted than the ScO_6 ones, with In–O–In angle *ca*. 157°, and Sc–O–Sc *ca*. 170°. InO_6 octahedra are, in general, more distorted and ScO_6 more regular, agreeing with what observed in previous works on layered perovskites[197,201]. The same trend can be found in pair distribution function studies on 50% doped $BaTiO_3$ with In[53] and Sc (see paper III). Interestingly, in framework perovskites the regularity of InO_6 coordination environments is a function of the difference in size between A- and B-site cations ($diff_{A–B}$, calculated by considering only host cations). Octahedra are regular in $BaCeO_3$[163] ($diff_{A–B}$ = 0.74 Å), tilted $BaZrO_3$[50,57] ($diff_{A–B}$ = 0.89 Å) and distorted in the hydrated 50% doped titanate phase[53] ($diff_{A–B}$ = 1.01 Å). The B-site cation becomes harder in the order $Ce^{4+} < Zr^{4+} < Ti^{4+}$ (Pearson hardness), all harder than In^{3+}. In framework perovskites the A-site is fully coordinated (CN = 12) but in layered perovskites the A-site sits in a 9-fold environment and an inverted tendency is observed. By comparing bond lengths and angles in $SrLaInO_4$ and $BaLaInO_4$[200] one can notice that larger size differences between A- and B-site cations (i.e. in $BaLaInO_4$) promote more regular In–O bonds and increased tilting of the InO_6 octahedra. For smaller differences the opposite is observed, less regular octahedra and smaller tilting. Ba^{2+} is a softer ion than In^{3+} but Sr^{2+} is harder. Even though the ions occupy different sites in layered perovskites, their coordination numbers are not so dissimilar as they are in ABX_3 perovskites. It seems therefore that increasingly harder cationic species in the lattice promote distortions in InO_6 octahedra and since Sr^{2+} is harder than La^{3+} the same can be stated for ScO_6 octahedra as well.

Interaction with water vapour

The reactivity of these phases towards moisture is high and their dehydration behaviour complex. The stability of the phases towards water vapour decreased with increasing average size of the A-site. With HYD2 $LaBaInO_4$ decomposed in $La(OH)_3$ and $Ba_4In_3O_{8.5}$ while $LaSrInO_4$ underwent reversible changes. The water uptake, even at ambient temperature, was fast and evident: all pellets prepared during the final synthesis stages hardly maintained the shape and tended to open up in an accordion-like fashion showing layer intercalation. This tendency is slowed down by employing acetone as suspending agent during the grinding step. An explanation for this observation can be found when considering the different intermolecular interactions existing in acetone and ethanol. Acetone molecules can't interlink *via* hydrogen bonds so the mixture in the mortar is left drier since the carbonyl group can be protonated by the water already present, which can so be stripped away with the evaporation of the suspending medium. *Fig. 6.5* shows the thermograms of the investigated phases, as-prepared and after HYD2.

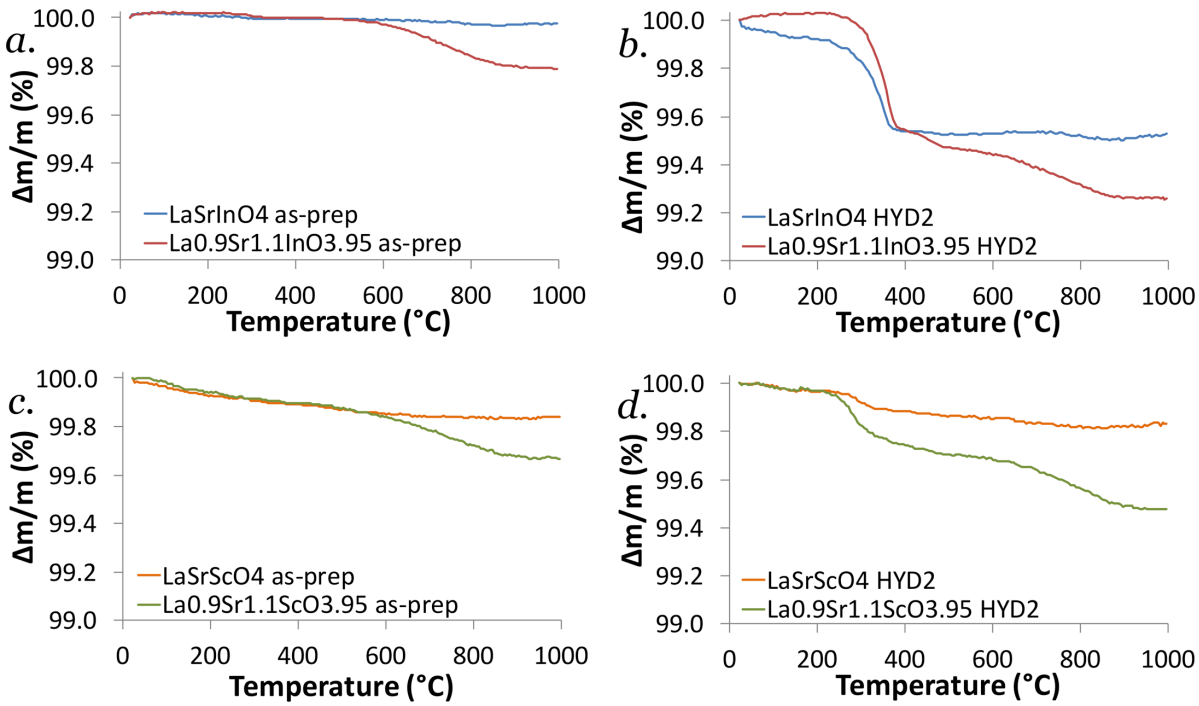

Fig. 6.5 Thermograms of the investigated phases. (*a.*) and (*b.*) show the behaviour, upon heating, of the In-based samples; (*c.*) and (*d.*) display the behaviour of the Sc-based ones. The "as-prep" label refers to as-prepared samples; "HYD2" refers to the samples that underwent the HYD2 protocol.

From inspection of the curves the dehydration behaviour can be divided into two regions. Below 500 °C intercalated water is lost. The mechanism involves two or more steps, as observed by Matvejeff, Lehtimäki *et al.*[83,189,190] in n = 2, 3 compounds of the Ruddlesden-Popper series. It seems, therefore, that the intercalation produced a mixture of various derivative species with different water content, being released within different ranges of temperature. In-based samples were able to accommodate larger amounts of intercalated water because of the larger unit cell. Above 500 °C, the behaviour of the parent phases did not produce flat signals therefore the presence of carbonated species that would decompose can't be ruled out. Appreciable mass losses in the doped compounds could be linked to water incorporated in the oxygen vacancies, absorbed *via* dissociation of water molecules[44]. If only oxygen vacancies were filled, theoretical mass losses would be 0.27% and 0.23%, respectively for the Sc and the In-based phase; measured mass losses are 0.23% and 0.21%, for the same compounds. Seemingly, vacancies were more easily filled in the In-based doped sample, representing an inversion of tendency for these layered phases. Hydration thermodynamics in $BaTiO_3$ are more favourable for Sc-doped samples than for In-doped ones[138]. The larger unit cell and ability to accommodate intercalated water that produces stacking disorder could influence the water uptake, making it easier when In is at the B-site of layered perovskites. Yet comparisons should be taken *cum grano salis* since the chemistry of the A- and B-sites are very different.

Electrochemical characterisation

Plots of the total conductivity as a function of inverse temperature, in the range 300-800 °C, for the Sc-based samples are shown in *fig. 6.6* and *6.7*. The phases exhibited semiconductive behaviour, as conductivities increased with temperature. The improvement of conductivity, under air, with the doping of the A-site (*fig. 6.5*) may be explained by the increased amount of charge carriers and the total conductivity would arise from the sum of oxide ion and electronic contributions, as vacancies can be filled to produce electron holes:

$$\tfrac{1}{2}\, O_2\,(g) \;+\; v_O^{\bullet\bullet} \;\rightleftarrows\; O_O^{\times} \;+\; 2\,h^{\bullet} \qquad (6.1)$$

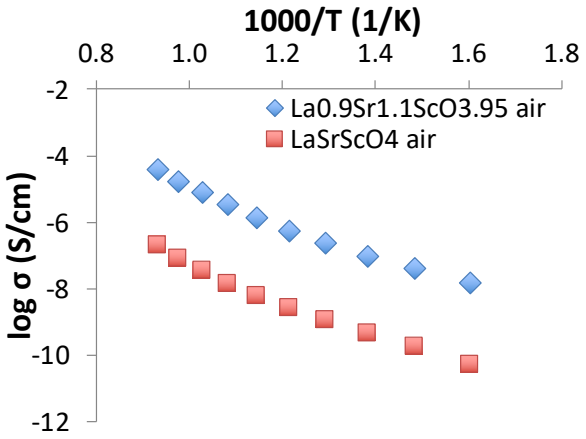

Fig. 6.6 Total conductivity of $La_{1-x}Sr_{1+x}ScO_{4-\delta}$ as a function of inverse temperature, in air (pO_2 = 0.21 atm).

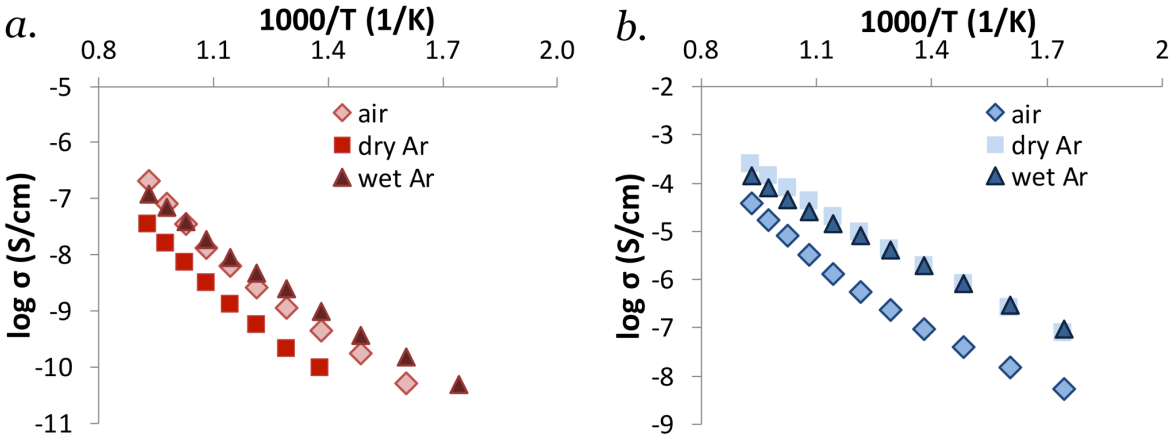

Fig. 6.7 Total conductivity of $La_{1-x}Sr_{1+x}ScO_{4-\delta}$ as a function of inverse temperature, under different conditions. Plot (*a.*) shows data relative to $LaSrScO_4$, while (*b.*) shows data relative to the doped phase, $La_{0.9}Sr_{1.1}ScO_{3.95}$.

For the two samples the total conductivity was measured under different conditions, as shown in *fig. 6.7*. The parent phase responded to low pO_2 (dry Ar) with a decrease in conductivity while air and wet Ar conditions improved the conducting properties. This behaviour indicated that oxide ion conduction is dominant along with *p*-type semiconductivity, where holes are charge carriers. Below 500 °C, and until 650 °C, wet Ar conditions improved the conductivity therefore it could be possible to have mobile protons among the charge carriers. The energies involved in charge transport varied with temperature and it was possible to distinguish two regimes of temperature dependence of the total conductivities, below and above 500 °C. *Table 6.6* summarises the calculated activation energy for the two samples.

Table 6.6 Values of activation energy extracted from conductivity data for $LaSrInO_4$ and $La_{0.9}Sr_{1.1}InO_{3.95}$, expressed in eV. *value obtained from the linear fit of only two data points.

	$LaSrScO_4$			**$La_{0.9}Sr_{1.1}ScO_{3.95}$**		
	air	*dry Ar*	*wet Ar*	*air*	*dry Ar*	*wet Ar*
< 500 °C	0.90	0.80*	0.79	0.78	0.83	0.79
> 500 °C	1.39	1.34	1.09	1.37	1.07	0.95

In $LaSrScO_4$ proton transport seems to be the process that is more energetically favoured, with proton transference numbers above 0.9 until 500 °C. The effect of humidity on the impedance of the material at room temperature was investigated by Kim and co-workers[204] who observed fast response to humidity changes, with a three orders of magnitude drop in the resistivity when increasing humidity from 20% to 95%. That was linked to the formation of physically absorbed water on the sample surface and to intercalated water. Protons as charge carriers can therefore be present. If true, the process is too energetically demanding with respect to the best proton conducting perovskite materials, where values in the range 0.4-0.6 eV are calculated[16,24].

For the doped phase, $La_{0.9}Sr_{1.1}ScO_{3.95}$, low pO_2 was more favourable for charge transport, as Ar atmospheres promoted higher conductivities. Under such conditions electrons contribute to the overall amount of charge carriers and *n*-type semiconductivity is present:

$$O_O^{\times} \rightleftarrows \tfrac{1}{2}\, O_2\ (g) + v_O^{\bullet\bullet} + 2\, e' \qquad (6.2)$$

No clear evidence of proton contributions was found. In these phases the oxygen vacancies created *via* acceptor-doping as a means to introduce protonic defects were not available since they were likely ordered. In the acceptor-doped phase, in fact, total conductivities under air were different when measured during the heating or cooling ramp (*fig. 6.8*). The parent phase is known to undergo a phase transition from orthorhombic to a tetragonal crystal structure at around 900 °C[197]; that is where the jump in conductivity during the heating ramp was registered for the doped phase. An order-disorder transition could provide the explanation. The ordering of oxygen vacancies up

to 900 °C would hinder charge transport and, as vacancies become disordered, transport of charge carriers, in this case oxide ions and holes, would become easier. Activation energies extracted from the conductivity data indicated that charge transport requires 0.3 fewer eV in the range 1000 °C to 800 °C of the cooling ramp. The same behaviour did not manifest under low pO_2 therefore, if indeed crystal symmetry affects the conducting properties, the presence of oxygen vacancies seemed to suppress any structural change at least until 1000 °C. The study of the temperature dependence of the structural parameters will bring more clarity, providing a way to rationalise the conductivity data.

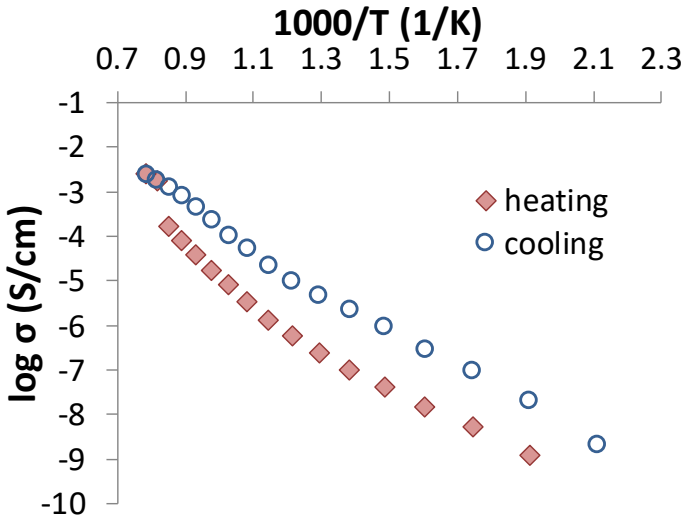

Fig. 6.8 Total conductivity of $La_{0.9}Sr_{1.1}ScO_{3.95}$ as a function of inverse temperature, measured in air, in the temperature range 200 °C to 1000 °C. The two curves show the behaviour during the heating and cooling ramp.

6.3.2 Conclusions

The stability of the investigated Ruddlesden-Popper phases is dependent on a combination of the relative average size of A- and B-site cations and the disorder of BO_6 octahedra. For synthesis, larger differences promoted the formation of n = 2 layered compounds, as seen for $LaBaScO_4$ and $LaBaInO_4$. Structurally, a harder A-site promoted heavier distortions of BO_6 octahedra. During hydration, stability decreased with larger A-site cations. The most stable phases, $LaSrScO_4$ and $LaSrInO_4$, were further investigated. Sc-based compounds were very stable towards hydration, at least until 800 °C under pH_2O of *ca*. 0.2 atm. In-based ones underwent reversible changes at 200 °C under the same pH_2O. That related to the size of the unit cell and to the higher disorder contributed by the irregular InO_6 octahedra, influencing also the amount of intercalated water that can be hosted, lower in the smaller and more regular Sc-based phases.

The dehydration behaviour was complex, with multiple mass loss steps. Until 500 °C intercalated water is lost; above 500 °C mass losses can be associated, in the doped phases, to the evolution of water incorporated in the oxygen vacancies. Vacancies seemed to be more easily filled in the In-based sample showing an inverted tendency with respect to $BaTiO_3$ doped phases.

The electrochemical characterisation was carried out for the Sc-based phases, showing semiconductive behaviour. $LaSrScO_4$ exhibited oxide ion conductivity and *p*-type semiconductivity, with possible proton conductivity contribution until 500 °C at least. The novel acceptor-doped phase, $La_{0.9}Sr_{1.1}InO_{3.95}$, behaved like a *n*-type semiconductor and data suggested the presence of ordered vacancies, detrimental to proton conductivity.

6.4 Double perovskites

In the last decade the double perovskite compound $Sr_2MgMoO_{6-\delta}$ has attracted interest in its potential application as anode material for SOFC. It is due to its high tolerance for sulphur-containing species and its interesting redox chemistry[205], very desirable properties for operating devices with high fuel flexibility. Proton conductivity in complex perovskite systems was first reported by Liang and co-authors in the niobate systems $Ba_3(Ca_{1.18}Nb_{1.82})O_{9-\delta}$ and $Sr_2(Sc_{1+x}Nb_{1-x})O_{6-\delta}$[206], and since then in tantalate-zirconate materials[207], cobalto-cuprates[208], ferrites[209], with niobates being the most successful. For these, it was concluded that a small size difference between the B-site cations and a high degree of B-site disorder were favourable for proton conductivity, although the mobility in niobate phases remained low[210]. Their limited success at conducting protons is mainly explained by the high activation energies of mobility, caused by the strong association of protonic defects with acceptor-dopants in the B site[75]. Another factor seems related to the difficulty of effectively doping the B-site in B-site ordered compounds.

The aim of this study was to synthesise a material that would combine the stability of $Sr_2MgMoO_{6-\delta}$ with the proton conducting properties of Nb-based ordered perovskite systems. Water uptake and protonic conductivity are absent in stoichiometric compounds[210] therefore while creating oxygen vacancies substituting of Nb^{5+} (0.64 Å) for Mo^{6+} (0.59 Å), the size difference between B-site cations would become smaller with increasing Nb content (being the size of Mg^{2+} 0.72 Å in a 6-fold coordination), which would also increase the degree of disorder[211], important factors for proton migration. Additionally, the dynamic redox chemistry contributed by the host phase could potentially mitigate the trapping effect that acceptor-dopants have in pure niobate systems and give a potential candidate for anode materials in PCFC.

6.4.1 Results and discussion

The first attempts at synthesising the phases were carried out in alumina boats and were unsuccessful. Those samples underwent non negligible mass losses, they were pale with green tinges (a likely sign of MoO_3 on the surface, its melting point being 795 °C and the boiling point 1155 °C) and the phase analysis revealed presence of $Sr_4Al_6(MoO_4)O_{12}$, all signs of decomposition and/or reaction with the vessel. It has been suggested that $A_2B'MoO_6$-type double perovskites suffer from Mo deficiency[212] therefore another vessel material was tried. Syntheses carried out in a Pt vessel produced the desired phases, all brown powders. The use of a Pt vessel[213] was determinant here for stabilising phases containing Mo^{6+}.

Table 6.7 shows the results of the Rietveld refinements. A model of the crystal structure of the parent phase Sr_2MgMoO_6 is shown in *fig. 6.9*. Different authors report about the crystal structure of Sr_2MgMoO_6, with either cubic[214], tetragonal[215], monoclinic[205,216], or triclinic[211,212,217] unit cells. The best agreement between experimental data and crystal model was achieved by employing a tetragonal model in the space group *I4/m*, agreeing with the model reported by Sher and co-workers[215]. For the Nb-doped phases, comparably good agreements were achieved also with a triclinic unit cell in the non-standard space group $I\bar{1}$. The $I\bar{1}$ model was first employed by Bernuy-Lopez *et al.*[217] in their structural work on $Sr_2MgMoO_{6-\delta}$ in order to account for systematic absences in electron diffractograms that were consistent with an *I*-centred cell. Later the same model was used by and Vasala and co-authors[211] for W and Nb substitutions at the B-site. In $I\bar{1}$ the O2 site is split into two more oxygen sites and the space group has been used for modelling ordered perovskites when MO_6 octahedra are distorted, imposing cells twice the volume of the primitive ones[218]. For the present study, the space group of higher symmetry was retained in order to reduce the number of variables to refine.

Impurity levels of $SrMoO_4$ and MgO were found in amounts not exceeding 2% in weight. $SrMoO_4$ is an impurity commonly found when such materials are sintered in air[211,212]. The exsolution of MgO was reported by Vasala and co-authors[211] as well in the Nb-doped phases, probably due to the avoidance of coordination numbers lower than 6 for Mg^{2+} in oxides[217] since the number of oxygen vacancies increases with the Nb concentration.

Table 6.7 Summary of the results of the Rietveld analysis of XRD data for the double perovskite phases $Sr_2Mg(Mo_{1-x}Nb_x)O_{6-\delta}$ (with x = 0, 0.3, 0.5) at RT (space group: *I4/m*).

	Sr_2MgMoO_6	***$Sr_2MgMo_{0.7}Nb_{0.3}O_{6-\delta}$***	***$Sr_2MgMo_{0.5}Nb_{0.5}O_{6-\delta}$***
a (Å)	5.57074(14)	5.59243(5)	5.60354(7)
c (Å)	7.92522(23)	7.94735(13)	7.95615(18)
Sr *4d* (0, ½, ¼)			
Mg / ***Mo*** *2a* (0, 0, 0)			
Occ. factor	0.993(4) / 0.007(4)	0.910(4) / 0.090(4)	0.867(4) / 0.133(4)
Mo / ***Mg*** *2b* (0, 0, ½)			
Occ. factor	0.956(4) / 0.044(4)	0.963(5) / 0.037(5)	0.911(6) / 0.089(6)
O1 *4e* (0, 0, *z*)	0.2477(13)	0.2524(14)	0.2498(20)
O2 *8h* (*x*, *y*, 0)	0.2705(21), 0.2239(17)	0.2840(18), 0.2185(14)	0.2814(26), 0.2182(18)
degree of order	0.99	0.82	0.73
R_{wp} (%)	19.57	18.99	19.38
R_F^2 (%)	29.79	14.99	11.55
χ^2	2.09	1.58	1.81
impurity phases (wt%)	$SrMoO_4$, 1.98(1)	MgO, 1.46(1)	$SrMoO_4$, 1.06(1) MgO, 1.65(1)

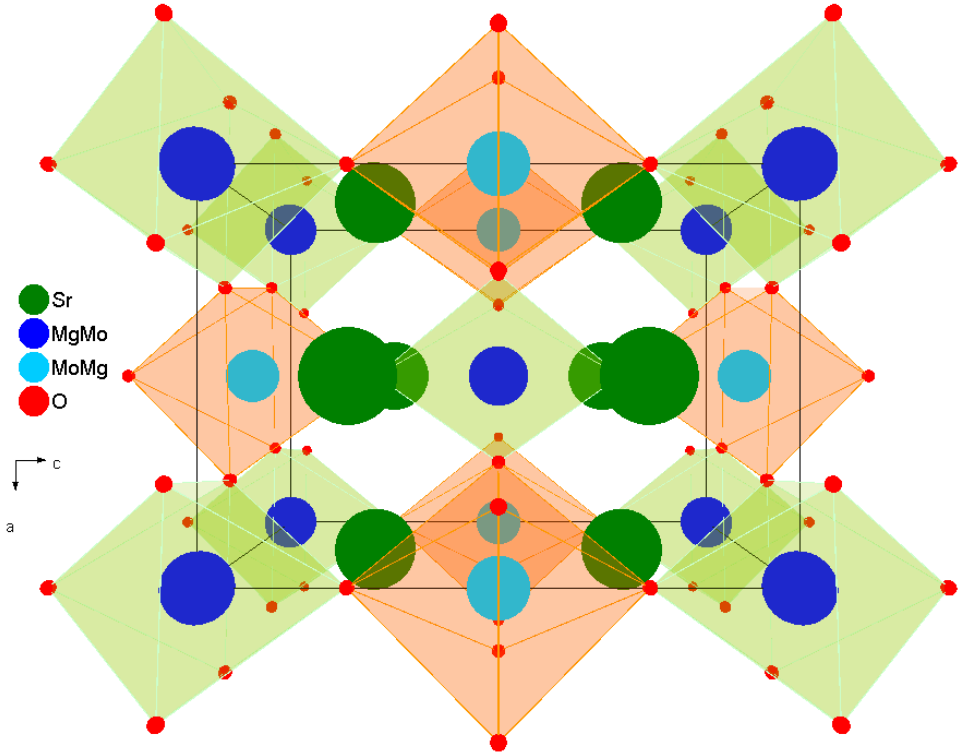

Fig. 6.9 Representation of the crystal structure of Sr_2MgMoO_6, a $A_2BB'O_6$ double perovskite alternating corner-sharing MgO_6 and MoO_6 octahedra.

After the Rietveld analysis, refined compositions were: $Sr_2Mg_{1.04(1)}Mo_{0.96(1)}O_{6-\delta}$ for the parent phase, $Sr_2Mg_{0.95(1)}(Mo, Nb)_{1.05(1)}O_{6-\delta}$ for the 30% Nb-doped phase, and $Sr_2Mg_{0.96(1)}(Mo, Nb)_{1.04(1)}O_{6-\delta}$ for the 50% Nb-doped phase. The XRD experiments prevented refinements of the shared Mo^{6+}/Nb^{5+} site occupancy since the two ions are isoelectronic hence indistinguishable by the X-rays probe. Serial parametric correlations affected the refinements therefore atomic displacement parameters were fixed to 0.001 $Å^2$ and occupancy factors of the oxygen sites were fixed to unitary values as imposing values based on expected stoichiometries produced worse fits. Here a limited 2ϑ range (15-65°) and poorer counting statistics were the likely reasons that affected the refinements. These experiments were performed with a Siemens D5000 diffractometer and represented an example where experiment design can be optimised in order to overcome the instrumental limitations. With a scintillation detector, lower count rates and lower resolutions (hence fewer independent observations, i.e. resolved diffracted intensities) are obtained, in fact, with respect to a solid-state one[219].

Sr_2MgMoO_6 was characterised by an almost perfect ordering of the two cations at the B-site, as Mg^{2+} and Mo^{6+} are different enough in size and charge. The unit cell expanded with increasing Nb concentration given its larger size. The degree of order, defined as $S = 2(frac_{Mg} - 0.5)$, decreased as oxygen vacancies are produced in the structure with the progressive replacement of Nb^{5+} for Mo^{6+}. This agreed with the observations of other investigators[211,217], therefore it is very likely that a relationship between ordering and concentration of oxygen vacancies exists. The difference in size and charge between B and B' ions becomes smaller with increasing Nb levels, therefore disorder at the B-site becomes more likely.

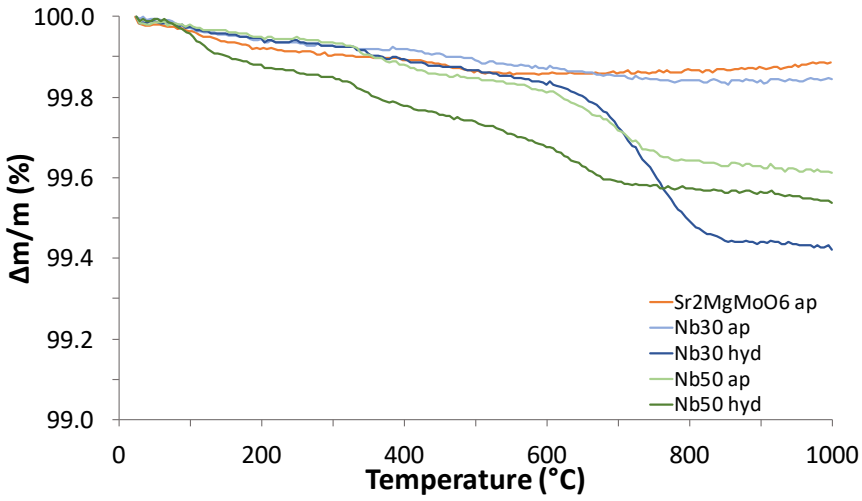

Fig. 6.10 Thermograms of the double perovskite phases. "Nb30" and "Nb50" respectively refer to the 30% and 50% Nb-doped phase. The "ap" label refers to as-prepared samples; "hyd" refers to the samples that underwent the hydration protocol.

Thermograms of the investigated samples are shown in *fig. 6.10*. No evidence of decomposition nor of hydrated products was found from the analysis of the diffraction patterns of the samples after the hydration experiment. All samples lost mass between room temperature and 300 °C and further mass losses were observed in the ranges 300 °C to 520 °C, and up to 1000 °C, especially in the doped samples. The sample of the parent phase exhibited the same behaviour though its mass slightly increased (+0.02%) above 520 °C: the same is reported during re-oxidation of a reduced sample[212]. This occurrence could be explained by an instrumental signal drift or by little O_2 impurities in the carrier gas feed. A two steps mass loss, in a comparable temperature range as the two Nb-doped samples, is observed in hydrated $Ba_2CaNbO_{5.5}$[220]. It is therefore possible for these phases to possess multiple distinct proton sites, each with particular bonding characteristics. Observed mass changes did not reflect the theoretical ones: –0.51% *vs*. –0.26% for Nb30 hyd; –0.31% *vs*. –0.82% for Nb50 hyd. The actual amount of Nb in these phases was unknown and it was only inferred from intended stoichiometries. A determination of the oxygen content of the samples[211] could help making better sense of the TG data, although that wouldn't tell anything about the proton environment nor bring new insight into the ordering of the defects, oxygen vacancies and protons, i. e. their accessibility and mobility. Neutron powder diffraction should be used to complement the structural information obtained with the X-rays.

6.4.2 Conclusions

Double perovskites of the kind $Sr_2Mg(Mo_{1-x}Nb_x)O_{6-\delta}$ (with x = 0, 0.3, 0.5) were studied in order to obtain potential anode materials that would combine the good stability towards sulphur poisoning of the parent phase with the higher proton conducting properties of Nb-based ordered perovskites. Increasing Nb levels disrupted the sharp ordering of the B-site of the parent phase while creating oxygen vacancies. The degree of order decreased, potentially conferring enhanced proton conducting properties. It seemed that vacancies can be filled by interaction of the systems with water vapour and that protonic defects experience multiple different environments. Unfortunately, the study of the water uptake did not provide any quantitative information about the proton content of the phases. Theoretical and experimental values did not overlap and that was due to the limited information about the Nb and O actual content. Further investigation is needed as the structural analysis is incomplete and a thorough characterisation of the B-site ordering can only be carried out by neutron scattering techniques.

6.5 Pyrochlores

In the mid-nineties, Shimura and co-workers reported protonic conductivities comparable to those of perovskite-based systems in the pyrochlore systems $Ln_2Zr_{1.8}Y_{0.2}O_{7-\delta}$, with Ln = La, Nd, Sm, Gd, Er[221]. Even for pyrochlores acceptor-doping seemed a good strategy for increasing the concentration of charge carries but it was later

shown by Omata *et al.* that A-site and B-site doping give different results[69]. In particular, acceptor-doping the A-site gave higher conductivities than B-site doping, because of the intrinsically vacant oxygen sites associated to the A cation. Despite promising results, the solubility of the dopant cation in the A-site is limited to a few percent. The same was found in Sm-based pyrochlores, where substitutional studies on the B-site showed that proton conductivity is favoured by smaller cations, such as Ti and Sn[222–224].

The aim of the study was to test the conclusions of previous studies on pyrochlore phases. A series of pyrochlore systems with Ti, Mo or Hf at the B-site was attempted and structurally characterised when possible. The main compositions were chosen because the respective pyrochlores are known. Further, the reduction of Ti^{4+} and Mo^{4+} to their respective trivalent cations could add electronic contribution to the total conductivity and produce phases with mixed ionic-electronic conduction[225,226], important for electrode materials in PCFC and hydrogen separation membranes. In the case of Hf, such proton conducting phases would represent novelties. The doping strategy considered cations of similar size (Mg^{2+}, Ca^{2+} and Sr^{2+} are common A-site dopants in proton conducting pyrochlore phases) so that the occupation of the same site was probable.

6.5.1 Results and discussion

The only successful syntheses were those relative to the titanium-based pyrochlores, as significant impurities were found in all other samples (*tab. 6.8*). The hafnate $La_2Hf_2O_7$ was considered pure enough to carry out a Rietveld analysis, although very weak impurity peaks were present and later characterised as a silicate.

Table 6.8 Summary of the syntheses attempted for the compositions with pyrochlore structure. Pyrochlore phases are referenced.

Desired phase	***Phase analysis***
$Y_2Ti_2O_7$	$Y_2Ti_2O_7$[227]
$Y_{1.92}Ca_{0.08}Ti_2O_{7-\delta}$	pyrochlore pattern
$Gd_2Ti_2O_7$	$Gd_2Ti_2O_7$[228]
$Gd_{1.92}Ca_{0.08}Ti_2O_{7-\delta}$	pyrochlore pattern
$Yb_2Ti_2O_7$	$Yb_2Ti_2O_7$[229]
$Yb_{1.92}Ca_{0.08}Ti_2O_{7-\delta}$	pyrochlore pattern
$Y_2Mo_2O_7$	$Y_2Mo_2O_7$[230], MoO_2, $Y_5Mo_2O_{12}$, $YMoO_4$
$Y_{1.92}Ca_{0.08}Mo_2O_{7-\delta}$	pyrochlore pattern, MoO_2, Y_2MoO_6
$Gd_2Mo_2O_7$	$Gd_2Mo_2O_7$[231], $Gd_2Mo_3O_9$
$Gd_{1.92}Ca_{0.08}Mo_2O_{7-\delta}$	$Gd_2Mo_2O_7$[231], MoO_2
$Yb_2Mo_2O_7$	$Yb_2Mo_2O_7$[232], MoO_2, unindexed phases
$Yb_{1.92}Ca_{0.08}Mo_2O_{7-\delta}$	$Yb_2Mo_2O_7$[232], MoO_2, $CaMoO_4$, unindexed phases
Y_2TiMoO_7	pyrochlore pattern, $Mo_{0.975}Ti_{0.025}O_2$
Gd_2TiMoO_7	pyrochlore pattern, Gd_2TiO_5
$Y_{1.9}Ti_{2.1}O_{7+\delta}$	$Y_2Ti_2O_7$[227], TiO_2
$La_2Hf_2O_7$	$La_2Hf_2O_7$[233], unindexed phases
$La_{1.95}Mg_{0.05}Hf_2O_{7-\delta}$	$La_2Hf_2O_7$[233], unindexed phases
$La_{1.95}Ca_{0.05}Hf_2O_{7-\delta}$	$La_2Hf_2O_7$[233], unindexed phases
$La_{1.9}Ca_{0.1}Hf_2O_{7-\delta}$	$La_2Hf_2O_7$[233], $CaHfO_3$, unindexed phases
$La_{1.95}Sr_{0.05}Hf_2O_{7-\delta}$	$La_2Hf_2O_7$[233], $SrHfO_3$, unindexed phases
$La_{1.9}Sr_{0.1}Hf_2O_{7-\delta}$	$La_2Hf_2O_7$[233], $SrHfO_3$, $Sr_3Hf_2O_7$, unindexed phases
$La_2Hf_{1.95}La_{0.05}O_{7-\delta}$	$La_2Hf_2O_7$[233], La_2O_3, $La_{10}(SiO_4)_6O_3$
$La_2Hf_{1.95}Sc_{0.05}O_{7-\delta}$	$La_2Hf_2O_7$[233], $LaScO_3$, unindexed phases
$La_2Hf_{1.9}Sc_{0.1}O_{7-\delta}$	$La_2Hf_2O_7$[233], $LaScO_3$, unindexed phases
$La_2Hf_{1.95}Ga_{0.05}O_{7-\delta}$	$La_2Hf_2O_7$[233], La_2O_3, $La_{10}(SiO_4)_6O_3$
$La_2Hf_{1.9}Ga_{0.1}O_{7-\delta}$	$La_2Hf_2O_7$[233], La_2O_3, $La_{10}(SiO_4)_6O_3$
$La_2Hf_{1.9}Zr_{0.05}Mo_{0.05}O_{7-\delta}$	unindexed phases
$La_2Hf_{1.8}Zr_{0.1}Mo_{0.1}O_{7-\delta}$	unindexed phases
$Sm_{1.8}Ca_{0.2}Ti_2O_{7-\delta}$	$Sm_2Ti_2O_7$[233], $Ca_{0.7}Sm_{0.19}TiO_3$

6.5.1.1 *Titanates*

Table 6.9 summarises the results of the Rietveld analysis. For all samples the $Fd\bar{3}m$ space group was retained although refinements that included unitary occupancy of the vacant site converged to produce fits with similar agreement indicators. This result suggested a disordered fluorite structures but refinement attempts using the $Fm\bar{3}m$ space group all produced far worse fits. It is likely that the weak scattering property of oxygen with respect to the heavier elements with XRD was responsible. In the retained model, all materials were characterised by A cations in scalenohedra and B cations in more regular coordination environments, as indicated by the quite large values of the positional parameter of the *48f* oxygens, which agreed with values reported in the literature.

Table 6.9 Summary of the results of the Rietveld analysis of XRD data for the pyrochlore phases $A_{2-x}Ca_xTi_2O_{7-\delta}$ (with A = Y, Gd, Yb and x = 0, 0.08) at RT (space group: $Fd\bar{3}m$).

	$Y_2Ti_2O_7$	***Ca-doped***	***$Gd_2Ti_2O_7$***	***Ca-doped***	***$Yb_2Ti_2O_7$***	***Ca-doped***
a (Å)	10.10060(2)	10.09642(2)	10.19088(3)	10.18457(4)	10.03656(3)	10.03398(3)
x_{48f}	0.4209(5)	0.4210(4)	0.4263(9)	0.4189(10)	0.4233(7)	0.4273(8)
SOF A-site		0.99(2)/0.01(2)		0.94(1)/0.06(1)		0.99(1)/0.01(1)
R_{wp} (%)	15.02	14.38	7.07	7.56	15.95	20.47
R_F^2 (%)	10.96	10.95	20.27	27.36	11.37	11.94
χ^2	3.67	3.33	1.72	2.13	4.30	6.34

Despite the apparent success of the syntheses, the doping did not yield the desired phases. Only in the Gd-based sample the Ca occupancy was large enough not to fall within the standard deviation. The indication is that a solid-state reaction is not the most effective way for Ca^{2+} to enter the structure. Indeed, for Y- and Gd-based titanates the Pechini method was employed by the first investigators in a study of their conducting properties[226]. The authors claimed doping levels up to 10 and 15 mol%, respectively for Y- and Gd-based samples, but provided no evidence regarding the success of the syntheses. Further, the Ca level dependence of the ionic conductivity in $Gd_2Ti_2O_7$ featured a shallow maximum at 10 mol%. In a successive study they detected impurities of $(Ca_{0.7}Gd_{0.3})TiO_3$ in the 10 and 15 mol% doped samples and eventually reported a solubility limit of 7 mol%[234]. Successful solid-state syntheses up to 10 mol% are reported in a solid-state NMR study of the $(Y_{1-x}Ca_x)_2Ti_2O_{7-\delta}$ solid solution. Compositions with x = 0.05, 0.1, 0.15 were attempted but the authors did not provide any conclusive evidence of the actual doping level of their phases. No impurities were detected by XRD but the ^{17}O MAS NMR spectrum of the 15 mol% doped sample did not show any evolution as a function of the Ca content, exception made for an extra resonance peak attributed to an unspecified impurity phase[235]. The same peak is present in all spectra. The recommendation is that a careful pre-characterisation of a phase composition should be made before undertaking further studies.

6.5.1.2 Molybdates

All Mo-based samples decomposed during the syntheses, due to the oxidation of Mo^{4+} to Mo^{6+} and subsequent MoO_3 volatilisation, despite the use of Ar atmosphere. The use of 5% H_2 in Ar reduced the transition metal to its elemental state. Mass losses associated to the volatilisation of MoO_3 increased in the order Gd < Y< Yb, following the decreasing size of the A-site cation, 1.05 Å, 1.02 Å, 0.98 Å, respectively for the trivalent ions in an 8-fold coordination environment. The oxidation of Mo^{4+} was evident from the increasingly oxidised species found in the samples subjected to longer residence time during the syntheses. Most likely the Ar flow, which should ensure a protective atmosphere, was the main source of oxidising species since it contained up to 2 ppm of oxygen, as stated in the analysis report that comes with the bottle. If so, the surface of a pellet would contain Mo species with a higher oxidation number. The hypothesis was tested by analysing the surface of a pellet of $Gd_2Mo_2O_7$, the sample that contained the least amount of impurities, by mean of XPS (X-ray photoelectron spectroscopy). The resulting spectrum was interpreted according to the Perkin-Elmer Handbook of X-ray Photoelectron Spectroscopy[236] and a work on as-prepared and reduced Mo oxides[237]. The surface of the pellet was composed by grains ranging in size from 1 up to 10 μm in diameter (*fig. 6.11*).

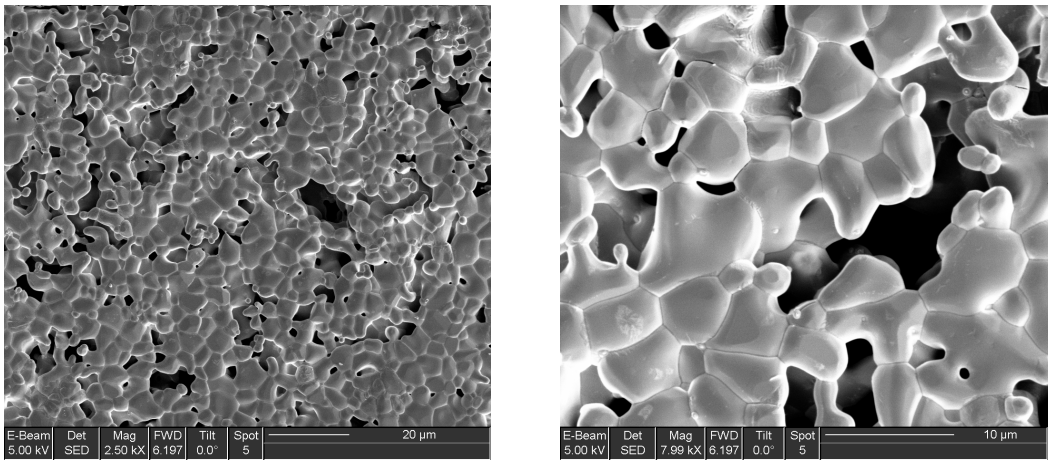

Fig. 6.11 Micrographs of the sample surface.

In order to establish the oxidation state of Mo, several spots on the surface of the pellet were analysed. *Figure 6.12* shows the overall spectrum of one area of the sample. The information relative to Mo lie between 220 and 240 eV, the spectral lines of the *3d* electrons, the most intense ones. The C *1s* line was used as reference for the scale of energies. This lies around 284 eV and is commonly used as a reference because adventitious C is a common pollutant and its 1s spectral line is often unequivocally identifiable. *Figure 6.13* shows the portion of the spectrum related to the *3d* electrons of Mo; the line is split because of the spin-orbit interaction.

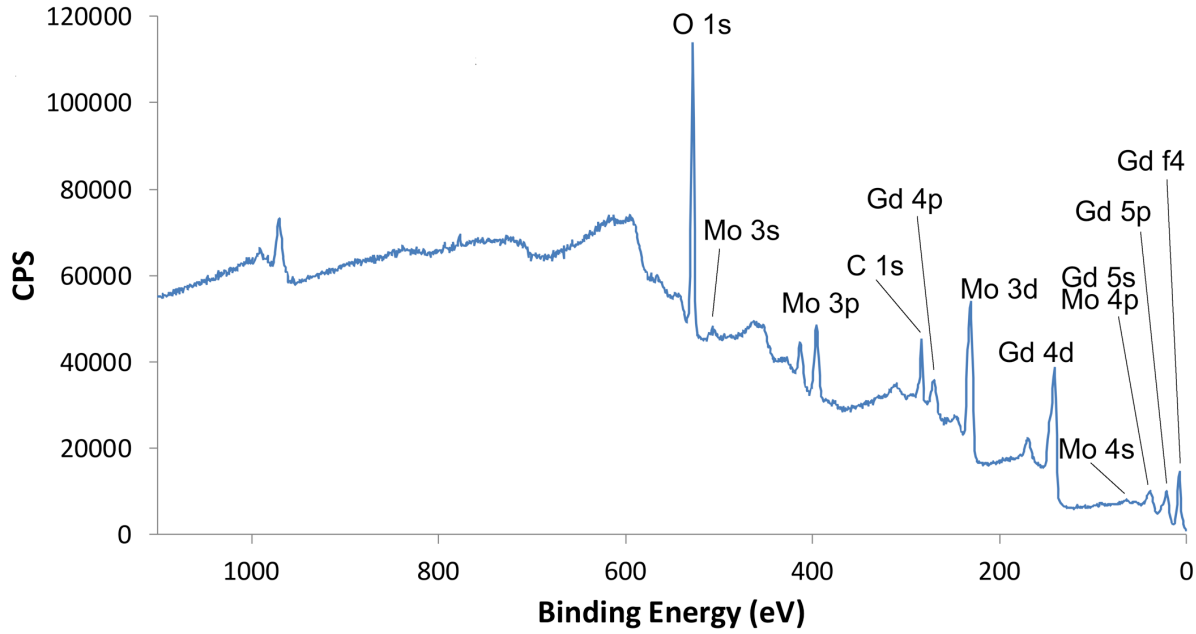

Fig. 6.12 X photoelectrons spectrum of the sample surface. The peaks of the main species are labelled according to the Perkin-Elmer Handbook of X-ray Photoelectron Spectroscopy[236].

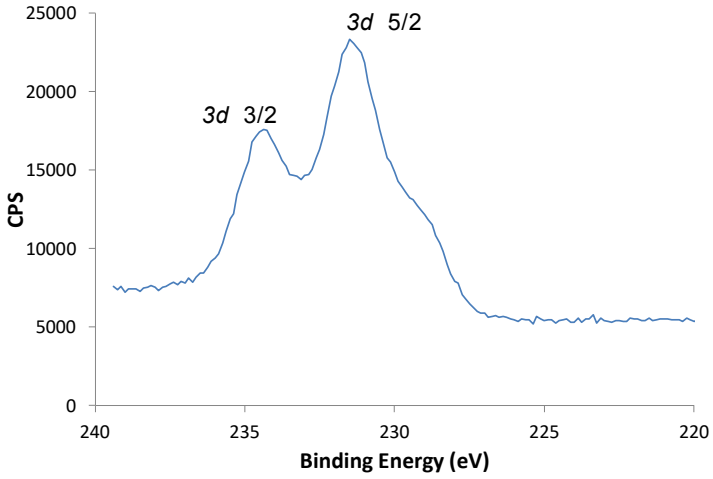

Fig. 6.13 Region of the spectrum showing the spectral lines related to Mo *3d* electrons. Splitting is caused by the spin-orbit interaction. Since the spin momentum *s* can be either +½ or −½, each level with orbital momentum $l > 0$ is split into two sublevels: this energy difference is the spin-orbit splitting. The peaks displaying the highest intensity are related to Mo in an oxidation state higher than 4+; on the right side of this set of peaks a shoulder is visible. That likely belongs to Mo^{IV} peaks that are hidden because of their weaker intensity.

The references used for the identification of the spectral lines do not include information about Mo species experiencing the kind of environment existing in the sample therefore a detailed discussion can't be carried out. What can be said, nonetheless,

concerns the position of the spectral lines related to Mo *3d* electrons and in particular the relative position of the ones in *fig. 6.13* with respect to the shoulder featuring in the same portion of the spectrum. Electrons belonging to a species with a higher oxidation state will be found at higher energies than those belonging to the same species with a lower oxidation state. This depends on the fact that the nucleus' charge binds more strongly the electrons that are less shielded. Accordingly, the surface should contain Mo species with a higher oxidation state than those in the bulk, because of the O_2 in the Ar feed. In order to confirm or discard this hypothesis, a region of the surface of the sample was modified by removing a thin layer with a common file so to expose what was underneath. *Fig. 6.14* shows an overlap of the photoelectron spectra of the surface as-is and of the abraded one. The shoulder had become more visible, while the main peaks had decreased their intensity. The shoulder revealed the presence of Mo^{IV}, the expected oxidation state, whose *3d* electrons have a spectral line in the range 229-230 eV *ca*. in MoO_2. The comparison, instead, revealed a surface richer in a further oxidised Mo species, with Mo^{VI} *3d* electrons in MoO_3 found in the range 232-233 eV *ca*.

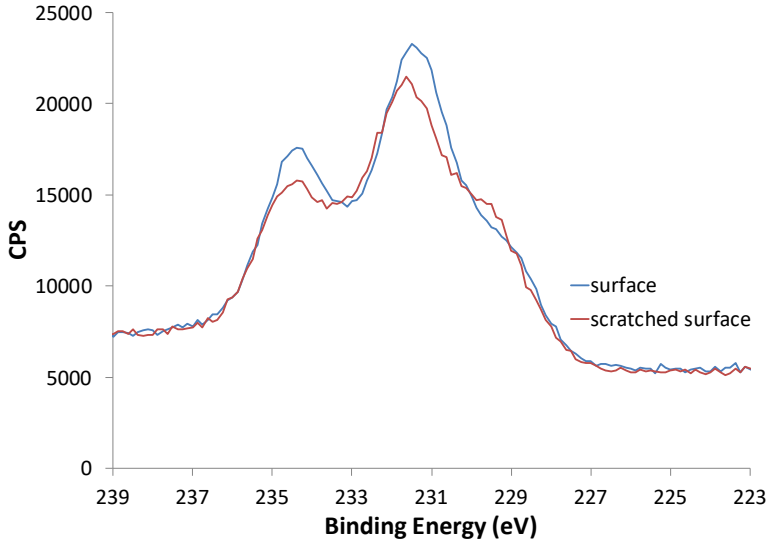

Fig. 6.14 Comparison of the spectral lines of Mo *3d* electrons. Spectrum of the surface as-is in blue and spectrum of the abraded surface in red. While the intensity of the peak related to $3d_{5/2}$ at 231.5 eV decreases, the intensity of the shoulder increases. The observation was related to the increased concentration of Mo^{IV} in the layers immediately under the surface of the synthesised sample.

A Focussed Ion Beam was used to cut small a cavity to allow a closer look at the grain boundaries below the surface. *Figure 6.15* shows an image of the cut performed on the surface. The occurrence of further oxidised Mo species on the surface was hinted at by the vestigial remains of the grain boundaries, where the composition was different than the bulk. The recommendation for the synthesis of Mo-containing pyrochlores is the use of a flow of inert gas which O_2 content has been stripped away, since 5% of H_2 in Ar produced metallic Mo. Alternatively, a sacrificial powder[213], high vacuum conditions or a sealed tube can be as well considered.

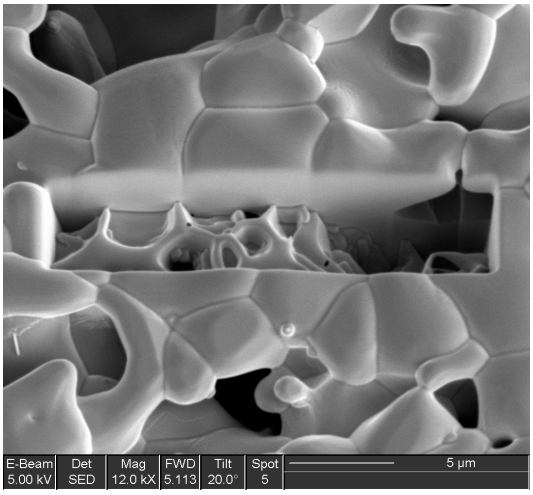

Fig. 6.15 SEM image of a cut performed on the surface of the sample by means of a Focussed Ion Beam.

6.5.1.3 Hafnates

$La_2Hf_2O_7$, a pyrochlore crystallising in the space group $Fd\bar{3}m$, had a cubic lattice parameter a = 10.78374(7) Å and positional parameter x of the *48f* oxygen site of 0.4220(5), in agreement with recent literature[238]. The refinement was lacking the contribution to the scattered intensities of a phase that was only clearly identifiable in the diffractograms of A-site doped and B-site Sc- and Ga-doped attempted samples. The diffraction pattern matched that of $La_{10}(SiO_4)_6O_3$ and the source of the contamination could have only been the material of which mortar and pestle are made: agate, a silicate rock. Indeed, the grinding steps of the syntheses, particularly with these materials, betrayed that the working surface of the pestle was undergoing a fine abrasion as it looked mirror polished. The contamination became visible to the naked eye with the final heating steps at 1600 °C, where the silicate phase segregated to the surface of the pellets (*fig. 6.16*). An EDX analysis on the surface of the crystals matched the atomic percentage composition of the phase $La_{10}(SiO_4)_6O_3$, crystallising in the space group $P6_3/m$.

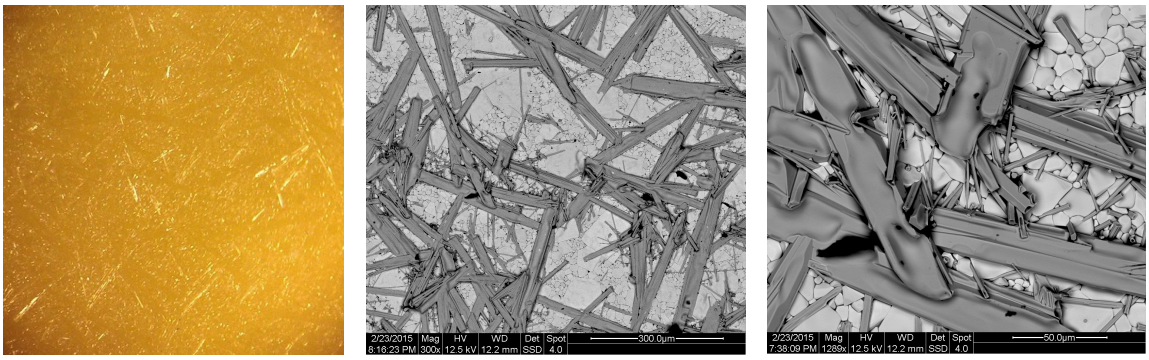

Fig. 6.16 Optical and SEM images of the surface of the Ga-doped attempted sample highlighting the presence of the impurity phase $La_{10}(SiO_4)_6O_3$.

Hafnate pyrochlores did not show any water uptake following the hydration experiments, indicating that the intrinsically vacant oxygen site was unavailable for hosting protonic defects. In fact, although that represents an interstitial site for the formation of a Frenkel defect, the additional vacancies formed by acceptor-doping play the major role for the formation and mobility of protonic defects[221]. Moreover, the rigidity of the lattice, which is reflected in the hardness of the materials that imposes harder grinding tools for solid-state syntheses or wet chemical route approaches, probably yields an inert oxygen sublattice.

6.51.4 Conclusions

The results of all pyrochlore phases attempted revealed the limitations of the employed synthesis protocols. Wet chemical routes are recommended for titanates and hafnates, while a strict control of the atmosphere is crucial for synthesising Mo-based phases and in general every time the valence of a metal ion needs to be tailored between far extremes.

6.6 Summary

A series of compositions within the relevant structural types for which protonic conduction is observed was investigated with respect to the doping strategy, the synthesis and the interaction of the system with water vapour. Because of time constraints these studies did not provide complete results, meaning that further preparative and/or characterisation work is needed in order to answer all research questions. Nonetheless, a series of conclusions useful for follow-up and future studies could be drawn, that relate to the specific systems and to the wider field of ceramic proton conductors.

In barium zirconate materials partial deuteration of the samples prevented the refinement of deuteron (proton) positions suggesting that hydration experiments with D_2O should be planned carefully or avoided altogether when exchange is likely. This was also observed in BTS samples (see paper I). Despite the drawback, the data were collected on a consistent set of samples (all prepared in the same way, a crucial factor for effective comparative studies) that allowed to verify structural observations in the literature. The results of the Rietveld analysis indicated that larger dopants do not necessarily produce larger cells but increase the local disorder of the oxygen sublattice. A doping strategy should therefore consider other factors instead of relying solely on ionic radii, such as the size difference between A- and B-site cations, their coordination environment, the hardness of a dopant relative to the host species and the degree of ionicity/covalency of a M–O bond.

The investigation of layered perovskite materials offered significative information in that regard. It was found that harder A-site cations promote disorder in the BO_6 octahedra. Along with larger size differences between cations, a similar trend is also observed for B-site host cations in In-doped cerate, zirconate and titanate ABO_3-type

materials. Disorder in the oxygen sublattice is beneficial to proton migration therefore the Pearson hardness of the cationic species can be included among the factors that will determine the choice of a dopant. The study of their interaction with water vapour highlighted the excellent stability of Sc-containing phases. On the other hand, while doping the A site produces vacancies that seems available for water incorporation, conductivity data suggest that only in the parent phase protons may be mobile. The likely ordering of vacancies in the doped phase suggested by conductivity data could be a reason. With respect to the parent phase, the increased average size of the A-site, therefore the increased size difference between A- and B-site, may offer an explanation for the ordering.

Ordering effects related to size of the cations are noticeable in the double perovskite system where they influence the oxygen sublattice. The degree of order at the B-site diminishes as the relative size of the two cations B and B' decreases. That seems to relate to the concentration of oxygen vacancies, increasing with the concentration of acceptor-dopant and the degree of disorder. Disorder in the structure is desirable for hosting mobile oxygen vacancies, the prerequisite of every ceramic proton conducting phase.

Oxygen vacancies should be accessible too. Rigid structures, as in the case of $La_2Hf_2O_7$ related phases, produce stable but also very hard materials for which the cost-effective solid-state synthesis is not suited. Rigidity is also detrimental to water incorporation as the dynamics of the oxygen sublattice would be negatively impacted and vacancy migration would become energetically demanding.

Chapter 7
Conclusions and outlook

To conclude, this thesis provided new insight into the crystal structure and the nature of the proton site in perovskite-structured Sc-substituted $BaTiO_3$ ceramic proton conductors. Previous studies could not fully explain the effect of the Sc substitution on the structure nor the difference in proton conductivities measured in hexagonal and cubic types. With a combination of thermogravimetric, scattering, spectroscopic and computational methods, new information was gathered, linking structural features to proton conducting properties and proton migration mechanisms.

It was found that increasing Sc levels drive the phase transformation from hexagonal to cubic structures. The former is characterised by long-range ordering of B-site cations, oxygen vacancies and protons. Sc and Ti share the *2a* metal site but Ti only can be found in the *4f*, characterised by a dimeric, face-sharing arrangement of TiO_6 octahedra. Three different proton sites were found. It was argued that the localised nature of the most stable one, the crystal site *12j*, is responsible for the poorer proton conductivity of these phases, where protons migrate *via* an energetically disfavoured 3-steps pathway.

Only one proton site was found in cubic types, the *24k*, characterised by high symmetry and multiplicity. Their extended environment is disordered, with Sc and Ti statistically distributed over the same crystal site, the octahedral interstice of the perovskite structure. At the local level, though, Ti orders and that determines the properties of these materials, the most interesting for proton conductivity. In particular, Sc substitution promotes off-centring of Ti away from its expected crystal site so that its local environment becomes similar to that found in the ferroelectric phase of $BaTiO_3$. Higher Sc levels in the cubic regime yield more severe off-centring of Ti, consequently, more distorted and tilted octahedra. The distribution of Ti–O bond lengths and the dynamic nature of the distortions are such that lower Sc levels are associated with stronger vacancy-vacancy interactions and a smaller size difference between oxygen vacancy and protonic defect. These effects translate into anomalously small volume changes upon hydration and are attenuated by higher Sc levels. It was proposed that lower Sc levels are also linked to features typical of the hexagonal structure, where the proton is localised, that are present in the cubic types and that tend to disappear with higher Sc content. Further, higher Sc concentrations weaken hydrogen bonds across the entire substitution range. All this would explain the superior proton conductivity measured in BTS70 with respect to BTS50.

Finally, the investigation of the BTS system and of other systems within the structural types relevant for proton conduction offered additional information that complements the guidelines for the choice of proton conducting perovskite systems. It is known that the best proton-conducting ceramic requires a combination of:

– a chemical composition that yields a regular structure and consequently a regular oxide ion framework, through which proton transport is allowed with the lowest possible energy barrier;
– high dynamics of the oxygen network, so that instantaneous distortions allow the formation of OH···O hydrogen bonds, some of them leading to a proton jump;
– a right level of basicity of the oxygen site, that is its affinity for protons: a too basic oxygen sublattice makes the phases reactive towards acidic gases, like $BaCeO_3$-based materials, while lower basicity hinders the formation of protonic defects;
– a small difference in electronegativity between cations that favours hydration thermodynamics;
– a microstructure that provides a homogeneous composition, facilitating proton transport across the grain boundary.

Aa a result of the present studies, it is proposed that a good ceramic perovskite-structured proton conductor should feature as well:

– a proton site of high symmetry and multiplicity, characteristic of $BaZrO_3$-based proton conductors and of the cubic types in the BTS system;
– a good combination of size mismatch, Pearson hardness and coordination chemistry of the B-site cations. Larger size and hardness differences combined with a wide range of CN, like in 50% In-doped $BaTiO_3$, produce a more static disorder of the BO_6 octahedra that are distorted but do not tilt. Smaller differences and a narrower range of CN, as seen in the BTS system, produce a dynamic disorder that in the case of BTS50 translates into its surprising small chemical expansion and in BTS70 yields superior proton conducting properties;
– accessible and mobile oxygen vacancies: when vacancies pin and order in the structure their migration becomes energetically demanding, hindering also proton transport.

The outlook for the BTS system is promising, at least for research. New information will be gathered with the RMC method currently being applied to the scattering data of the hydrated materials. Additional information can also be extracted from the study of the ferroelectric behaviour of the cubic phases. The ordering of Ti can so be linked to the polarisation in the material and add new insight into its proton transport properties. From the point of view of the technical importance, further research is crucial. Sintering and densification behaviours need to be studied as well in order to produce more realistic predictions for the applicability of these materials. Indeed, BTS70 is expensive but the high Sc content is associated to the superior stability of the phase and to its remarkable proton conducting properties. Co-doping is a route that should be explored in order to lower its content and study how the structural features are reflected in the materials properties.

Acknowledgements

I would like to express my gratitude to my supervisors, current and past, Sten G. Eriksson, Christopher S. Knee, Paul F. Henry and Maths Karlsson without whom I would have never made it this far.

Many thanks go to S. M. H. "Habib" Rahman for his support and his work, that laid the foundations for mine.

Many more thanks to Wojciech A. Sławiński and Erik Jedvik Granhed.

Special thanks go to Vratislav Langer and Stefan T. Norberg for the useful discussions about X-ray diffraction and the diffractometers.

I also want to thank Jan-Erik Svensson and the whole OOMK division for it has been a great group for finding stimulant discussions, support and friendship through these years.

Acknowledgements go to our administrators and technicians as well, for working out even the most unusual matters: Charlotte Bouveng, Sandra Gustafson, Susanne Bågenfelt, Anna Oskarsson, Esa Väänänen, Erik Brunius, Törbjorn Jönsson and research engineer Lynga Huang Normann.

Finally, I thank my family and friends for their unconditional love and support during this journey.

Bibliography

1. Walsh, J. H., Chipman, J., King, T. B. & Grant, N. J., "Hydrogen in Steelmaking Slags", *J. Met.* 1568–1576 (1956).

2. Stotz, S. & Wagner, C., "Die Löslichkeit von Wasserdampf und Wasserstoff in festen Oxiden", *Berichte der Bunsengesellschaft für Phys. Chemie* **70**, 781–788 (1966).

3. Hill, G. J., "The effect of hydrogen on the electrical properties of rutile", *British J. Appl. Phys. (Journal Phys. D)* **1**, 1151–1162 (1968).

4. Shores, D. A. & Rapp, R. A., "Hydrogen Ion (Proton) Conduction in Thoria-Base Solid Electrolytes", *J. Electrochem. Soc.* **119**, 300–305 (1972).

5. Pope, J. M., "The use of $BaTiO_3$ as a solid-electrolyte to determine water vapor effects upon electrical transport mechanisms", *Mater. Res. Bull.* **9**, 1111–1118 (1974).

6. *The limits to growth,* Meadows, D. H., Meadows, D. L., Randers, J. & Behrens, W. W. III, Universe Books, New York, 1972. ISBN 0-87663-165-0

7. Bruinink, J., "Proton migration in solids", *J. Appl. Electrochem.* **2**, 239–249 (1972).

8. Glasser, L., "Proton Conduction and Injection in Solids", *Chem. Rev.* **75**, 21–65 (1975).

9. Iwahara, H., Uchida, H., Ono, K. & Ogaki, K., "Proton Conduction in Sintered Oxides Based on $BaCeO_3$", *J. Electrochem. Soc.* **135**, 529 (1988).

10. Iwahara, H., "High temperature proton conducting oxides and their applications to solid electrolyte fuel cells and steam electrolyzer for hydrogen production", *Solid State Ionics* **28–30**, 573–578 (1988).

11. Iwahara, H., Esaka, T., Uchida, H. & Maeda, N., "Proton conduction in sintered oxides and its application to steam electrolysis for hydrogen production", *Solid State Ionics* **3/4**, 359–363 (1981).

12. Münch, W., Seifert, G., Kreuer, K. D. & Maier, J., "A quantum molecular dynamics study of proton conduction phenomena in $BaCeO_3$", *Solid State Ionics* **86–88**, 647–652 (1996).

13. Babilo, P. & Haile, S. M., "Enhanced sintering of yttrium-doped barium zirconate by addition of ZnO", *J. Am. Ceram. Soc.* **88**, 2362–2368 (2005).

14. Rahman, S. M. H., Ahmed, I., Haugsrud, R., Eriksson, S. G. & Knee, C. S., "Characterisation of structure and conductivity of $BaTi_{0.5}Sc_{0.5}O_{3-\delta}$", *Solid State Ionics* **255**, 140–146 (2014).

15. Rahman, S. M. H. *et al*., "Proton conductivity of hexagonal and cubic $BaTi_{1-x}Sc_xO_{3-\delta}$ ($0.1 \leq x \leq 0.8$)", *Dalton Trans.* **43**, 15055–15064 (2014).

16. Kochetova, N., Animitsa, I., Medvedev, D., Demin, A. & Tsiakaras, P., "Recent activity in the development of proton-conducting oxides for high-temperature applications", *RSC Adv.* **6**, 73222–73268 (2016).

17. Yajima, T., Koide, K., Fukatsu, N., Ohashi, T. & Iwahara, H., "A new hydrogen sensor for molten aluminum", *Sensors and Actuators B* **14**, 697–699 (1993).

18. Yajima, T., Koide, K., Takai, H., Fukatsu, N. & Iwahara, H., "Application of hydrogen sensor using proton conductive ceramics as a solid electrolyte to aluminum casting industries", *Solid State Ionics* **79**, 333–337 (1995).

19. *Proton-Conducting Ceramics*, ed. Marrony, M., Taylor & Francis Group, LLC, 2016, ISBN: 978-981-4613-85-9.

20. Kurita, N. *et al.,* "The measurement of hydrogen activities in molten copper using an oxide protonic conductor", *Metall. Mater. Trans. B: Process Metall. Mater. Process. Sci.* **27**, 929–935 (1996).

21. Kondo, M., Muroga, T., Katahira, K. & Oshima, T., "Application of Proton Conductors To Hydrogen Monitoring for Liquid Metal and Molten Salt Systems", *J. Power Energy Syst.* **2**, 590–597 (2008).

22. S*olid Oxide Fuel Cells: Facts and Figures*, ed. Irvine, J. T. S. & Connor, P., Springer-Verlag, London, 2013. DOI: 10.1007/978-1-4471-4456-4.

23. *Hydrogen and Fuel Cell*, ed. Töpler, J. & Lehmann, J., Springer-Verlag, Berlin Heidelberg, 2016. DOI: 10.1007/978-3-662-44972-1.

24. Kreuer, K. D., "Aspects of the formation and mobility of protonic charge carriers and the stability of perovskite-type oxides", *Solid State Ionics* **125**, 285–302 (1999).

25. Ahamer, C., Opitz, A. K., Rupp, G. M. & Fleig, J., "Revisiting the temperature dependent ionic conductivity of yttria stabilized zirconia (YSZ)", *J. Electrochem. Soc.* **164**, F790–F803 (2017).

26. An, H. *et al.,* "A 5×5 cm^2 protonic ceramic fuel cell with a power density of 1.3 W cm^{-2} at 600 °C", *Nat. Energy* **3**, 870–875 (2018).

27. Deibert, W., Ivanova, M. E., Baumann, S. & Guillon, O., "Ion-conducting ceramic membrane reactors for high-temperature applications", *J. Memb. Sci.* **543**, 79–97 (2017).

28. Karagiannakis, G., Kokkofitis, C., Zisekas, S. & Stoukides, M., "Catalytic and electrocatalytic production of H_2 from propane decomposition over Pt and Pd in a proton-conducting membrane-reactor", *Catal. Today* **104**, 219–224 (2005).

29. Kyriakou, V., Athanasiou, C., Garagounis, I. & Skodra, A., "Production of H_2 and C_2 hydrocarbons from methane in a proton conducting solid electrolyte cell using a Au–5Ce–5Na_2WO_4/SiO_2 anode", *Int. J. Hydrogen Energy* **37**, 16636–16641 (2012).

30. Kokkofitis, C., Ouzounidou, M., Skodra, A. & Stoukides, M., "Catalytic and electrocatalytic production of H_2 from the water gas shift reaction over Pd in a high temperature proton-conducting cell-reactor", *Solid State Ionics* **178**, 475–480 (2007).

31. Amar, I. A., Lan, R. & Petit, C. T. G., "Solid-state electrochemical synthesis of ammonia: a review", *J. Solid State Electrochem.* **15**, 1845–1860 (2011).

32. Morejudo, S. H. et al., "Direct conversion of methane to aromatics in a catalytic co-ionic membrane reactor", *Science* **353**, 563–567 (2016).

33. Malerød-Fjeld, H. *et al*., "Thermo-electrochemical production of compressed hydrogen from methane with near-zero energy loss", *Nat. Energy* (2017).

34. Kreuer, K. D., "Fast proton transport in solids", *J. Mol. Struct.* **177**, 265–276 (1988).

35. Colomban, P. & Novak, A., "Proton transfer and superionic conductivity in solids and gels", *J. Mol. Struct.* **177**, 277–308 (1988).

36. Kreuer, K. D., Dippel, T., Hainovsky, N. G. & Maier, J., "Proton Conductivity: Compounds and their Structural and Chemical Peculiarities", *Berichte der Bunsengesellschaft für Phys. Chemie* **96**, 1736–1742 (1992).

37. Münch, W., Seifert, G., Kreuer, K. D. & Maier, J., "A quantum molecular dynamics study of the cubic phase of $BaTiO_3$ and $BaZrO_3$", *Solid State Ionics* **97**, 39–44 (1997).

38. Kreuer, K. D., Schönherr, E. & Maier, J., "Proton and oxygen diffusion in $BaCeO_3$ based compounds: A combined thermal gravimetric analysis and conductivity study", *Solid State Ionics* **70–71**, 278–284 (1994).

39. Kreuer, K. D., Dippel, T., Baikov, Y. M. & Maier, J., "Water solubility, proton and oxygen diffusion in acceptor doped $BaCeO_3$: A single crystal analysis", *Solid State Ionics* **86–88**, 613–620 (1996).

40. Hempelmann, R. *et al*., "Quasielastic neutron scattering study of proton diffusion in $SrCe_{0.95}Yb_{0.05}H_{0.02}O_{2.985}$", *Solid State Ionics* **77**, 152–156 (1995).

41. Matzke, T. *et al*., "Quasielastic thermal neutron scattering experiment on the proton conductor $SrCe_{0.95}Yb_{0.05}H_{0.02}O_{2.985}$", *Solid State Ionics* **86–88**, 621–628 (1996).

42. Norby, T. & Larring, Y., "Concentration and transport of protons in oxides", *Curr. Opin. Solid State Mater. Sci.* **2**, 593–599 (1997).

43. Shimijo, F., Hoshino, K. & Okazaki, H., "First-Principle Molecular-Dynamics Simulation of Proton Diffusion in Sc-doped $SrTiO_3$", *J. Phys. Soc. Japan* **66**, 8–10 (1997).

44. Kreuer, K. D, "Proton-Conducting Oxides", *Ann. Rev. Mater. Res.* **33**, 333–359 (2003).

45. Kreuer, K. D., Münch, W., Traub, U. & Maier, J., "On Proton Transport in Perovskite-Type Oxides and Plastic Hydroxides", *Berichte der Bunsengesellschaft für Phys. Chemie* **102**, 552–559 (1998).

46. Kreuer, K. D., "On the complexity of proton conduction phenomena", *Solid State Ionics* **136–137**, 149–160 (2000).

47. Münch, W., Kreuer, K. D., Seifert, G. & Maier, J., "Proton diffusion in perovskites: Comparison between $BaCeO_3$, $BaZrO_3$, $SrTiO_3$, and $CaTiO_3$ using quantum molecular dynamics", *Solid State Ionics* **136–137**, 183–189 (2000).

48. Norby, T., "Solid-state protonic conductors: principles, properties, progress and prospects", *Solid State Ionics* **125**, 1–11 (1999).

49. Ahmed, I. *et al.*, "Location of deuteron sites in the proton conducting perovskite $BaZr_{0.50}In_{0.50}O_{3-y}$", *J. Alloys Compd.* **450**, 103–110 (2008).

50. Karlsson, M. *et al.*, "Short-Range Structure of Proton-Conducting Perovskite $BaIn_xZr_{1-x}O_{3-x/2}$ (x = 0–0.75)", *Chem. Mater.* **20**, 3480–3486 (2008).

51. Giannici, F., Longo, A., Kreuer, K. D., Balerna, A. & Martorana, A., "Dopants and defects : Local structure and dynamics in barium cerates and zirconates", *Solid State Ionics* **181**, 122–125 (2010).

52. Giannici, F. *et al.*, "Long-Range and Short-Range Structure of Proton-Conducting Y:$BaZrO_3$", *Chem. Mater.* **23**, 2994–3002 (2011).

53. Norberg, S. T., Rahman, S. M. H., Hull, S., Knee, C. S. & Eriksson, S. G., "The proton conducting electrolyte $BaTi_{0.5}In_{0.5}O_{2.75}$: determination of the deuteron site and its local environment", *J. Phys. Condens. Matter* **25**, 454214 (2013).

54. Zeudmi Sahraoui, D. & Mineva, T., "Effect of dopant nature on structures and lattice dynamics of proton-conducting $BaZrO_3$", *Solid State Ionics* **253**, 195–200 (2013).

55. Karlsson, M. *et al.*, "Vibrational properties of protons in hydrated $BaIn_xZr_{1-x}O_{3-x/2}$", *Phys. Rev. B* **72**, 094303 (2005).

56. Karlsson, M. *et al.*, "O–H wag vibrations in hydrated $BaIn_xZr_{1-x}O_{3-x/2}$ investigated with inelastic neutron scattering", *Phys. Rev. B* **77**, 104302 (2008).

57. Mazzei, L. *et al*., "Local structure and vibrational dynamics in indium-doped barium zirconate", *J. Mater. Chem. A* **7**, 7360-7372 (2019).

58. Chatzichristodoulou, C., Norby, P., Hendriksen, P. V. & Mogensen, M. B., "Size of oxide vacancies in fluorite and perovskite structured oxides", *J. Electroceramics* **34**, 100–107 (2015).

59. Jedvik, E., Lindman, A., Benediktsson, M. Þ. & Wahnström, G., "Size and shape of oxygen vacancies and protons in acceptor-doped barium zirconate", *Solid State Ionics* **275**, 2–8 (2015).

60. Larring, Y. & Norby, T., "The equilibrium between water vapour, protons, and oxygen vacancies in rare earth oxides", *Solid State Ionics* **97**, 523–528 (1997).

61. Woodward, D. I., Reaney, I. M., Yang, G. Y., Dickey, E. C. & Randall, C. A., "Vacancy ordering in reduced barium titanate", *Appl. Phys. Lett.* **84**, 4650–4652 (2004).

62. Nyman, B. J., Björketun, M. E. & Wahnström, G., "Substitutional doping and oxygen vacancies in $La_2Zr_2O_7$ pyrochlore oxide", *Solid State Ionics* **189**, 19–28 (2011).

63. Knight, K. S., "Structural phase transitions, oxygen vacancy ordering and protonation in doped $BaCeO_3$: results from time-of-flight neutron powder diffraction investigations", *Solid State Ionics* **145**, 275–294 (2001).

64. Kalland, L.-E. *et al*., "C-type related order in the defective fluorites $La_2Ce_2O_7$ and $Nd_2Ce_2O_7$ studied by neutron scattering and ab initio MD simulations", *Phys. Chem. Chem. Phys.* **18**, 24070–24080 (2016).

65. Norberg, S. T. *et al*., "Pyrochlore to Fluorite Transition: The $Y_2(Ti_{1-x}Zr_x)_2O_7$ ($0.0 \leq x \leq 1.0$) System", *Chem. Mater.* **24**, 4294–4300 (2012).

66. Marrocchelli, D., Perry, N. H. & Bishop, S. R., "Understanding chemical expansion in perovskite-structured oxides", *Phys. Chem. Chem. Phys.* **17**, 10028–10039 (2015).

67. Eriksson Andersson, A. K., Selbach, S. M., Knee, C. S. & Grande, T., "Chemical expansion due to hydration of proton-conducting perovskite oxide ceramics", *J. Am. Ceram. Soc.* **97**, 2654–2661 (2014).

68. Han, D., Hatada, N. & Uda, T., "Chemical Expansion of Yttrium-Doped Barium Zirconate and Correlation with Proton Concentration and Conductivity", *J. Am. Ceram. Soc.* **99**, 3745–3753 (2016).

69. Omata, T., Ikeda, K., Tokashiki, R. & Otsuka-Yao-Matsuo, S., "Proton solubility for $La_2Zr_2O_7$ with a pyrochlore structure doped with a series of alkaline-earth ions", *Solid State Ionics* **167**, 389–397 (2004).

70. Omata, T., Kita, M., Goto, Y., Okura, T. & Otsuka-Yao-Matsuo, S., "Formation and Thermal Stability of Hydrate-Like Compounds of $Ba_2(In_{1-x}M^{III}_x)_2O_5 \cdot nH_2O$ (M^{III} = Ga, Sc, Lu, and Y)", *J. Electrochem. Soc.* **152**, A1068–A1072 (2005).

71. Haugsrud, R. & Norby, T., "Proton conduction in rare-earth ortho-niobates and ortho-tantalates", *Nat. Mater.* **5**, 193–196 (2006).

72. Haugsrud, R. & Norby, T., "High-temperature proton conductivity in acceptor-doped $LaNbO_4$", *Solid State Ionics* **177**, 1129–1135 (2006).

73. Haugsrud, R., "Defects and transport properties in Ln_6WO_{12} (Ln = La, Nd, Gd, Er)", *Solid State Ionics* **178**, 555–560 (2007).

74. Haugsrud, R. & Kjølseth, C., "Effects of protons and acceptor substitution on the electrical conductivity of La_6WO_{12}", *J. Phys. Chem. Solids* **69**, 1758–1765 (2008).

75. Vigen, C. K., Bjørheim Svendsen, T. & Haugsrud, R., "The role of B-site cations on proton conductivity in double perovskite oxides La_2MgTiO_6 and La_2MgZrO_6", *Int. J. Hydrogen Energy* **37**, 7983–7994 (2012).

76. Besikiotis, V., Knee, C. S., Ahmed, I., Haugsrud, R. & Norby, T., "Crystal structure, hydration and ionic conductivity of the inherently oxygen-deficient $La_2Ce_2O_7$", *Solid State Ionics* **228**, 1–7 (2012).

77. Bielecki, J. *et al*., "Short-range structure of the brownmillerite-type oxide $Ba_2In_2O_5$ and its hydrated proton-conducting form $BaInO_3H$", *J. Mater. Chem. A* **2**, 16915–16924 (2014).

78. Goldschmidt, V. M., "Die Gesetze der Krystallochemie", *Naturwissenschaften* **14**, 477–485 (1926).

79. Megaw, H. D., "Crystal Structure of Barium Titanate", *Nature* **155**, 484–485 (1945).

80. Tilley, R. J. D., *Perovskites: Structure-Property Relationships*, John Wiley & Sons, 2016. DOI: 10.1002/9781118935651.

81. Weller, M. T., Weber, O. J., Henry, P. F., Di Pumpo, A. M. & Hansen, T. C., "Complete structure and cation orientation in the perovskite photovoltaic methylammonium lead iodide between 100 and 352 K", *Chem. Commun.* **51**, 4180–4183 (2015).

82. Stranks, S. D. & Snaith, H. J., "Metal-halide perovskites for photovoltaic and light-emitting devices", *Nat. Nanotechnol.* **10**, 391–402 (2015).

83. Lehtimäki, M., Yamauchi, H. & Karppinen, M., "Stability of Ruddlesden-Popper-structured oxides in humid conditions", *J. Solid State Chem.* **204**, 95–101 (2013).

84. Kudo, T. & Fueki, K., *Solid State Ionics*, Kodansha Ltd., Tokio, 1990. ISBN 3-527-28166-5

85. Kröger, F. A. & Vink, H. J., "Relations between the Concentrations of Imperfections in Crystalline Solids", *Solid State Phys.* **3**, 307–435 (1956).

86. Norby, T., Widerøe, M., Glöckner, R. & Larring, Y., "Hydrogen in oxides", *Dalt. Trans.* 3012–3018 (2004).

87. Bjørheim, T. S. *et al.*, "A combined conductivity and DFT study of protons in $PbZrO_3$ and alkaline earth zirconate perovskites", *Solid State Ionics* **181**, 130–137 (2010).

88. Münch, W., Kreuer, K. D., Seifert, G. & Maier, J., "The relation between crystal structure and the formation and mobility of protonic charge carriers in perovskite-type oxides: A case study of Y-doped $BaCeO_3$ and $SrCeO_3$", *Phase Transitions* **68**, 567–586 (1999).

89. Takeuchi, K. et al., "The crystal structures and phase transitions in Y-doped $BaCeO_3$: their dependence on Y concentration and hydrogen doping", *Solid State Ionics* **138**, 63–77 (2000).

90. Malavasi, L., Ritter, C. & Chiodelli, G., "Correlation between thermal properties, electrical conductivity, and crystal structure in the $BaCe_{0.80}Y_{0.20}O_{2.9}$ proton conductor", Chem. Mater. **20**, 2343–2351 (2008).

91. Eriksson Andersson, A. K., Selbach, S. M., Grande, T. & Knee, C. S., "Thermal evolution of the crystal structure of proton conducting $BaCe_{0.8}Y_{0.2}O_{3-\delta}$ from high-resolution neutron diffraction in dry and humid atmosphere", *Dalt. Trans.* **44**, 10834–10846 (2015).

92. Sammes, N., Phillips, R. & Smirnova, A., "Proton conductivity in stoichiometric and sub-stoichiometric yittrium doped $SrCeO_3$ ceramic electrolytes", *J. Power Sources* **134**, 153–159 (2004).

93. Matsumoto, H., Kawasaki, Y., Ito, N., Enoki, M. & Ishihara, T., "Relation Between Electrical Conductivity and Chemical Stability of $BaCeO_3$-Based Proton Conductors with Different Trivalent Dopants", *Electrochem. Solid-State Lett.* **10**, B77–B80 (2007).

94. Oikawa, I. & Takamura, H., "Correlation among Oxygen Vacancies, Protonic Defects, and the Acceptor Dopant in Sc-Doped $BaZrO_3$ Studied by ^{45}Sc Nuclear Magnetic Resonance", *Chem. Mater.* **27**, 6660–6667 (2015).

95. Ahmed, I. *et al.*, "Synthesis and structural characterization of perovskite type proton conducting $BaZr_{1-x}In_xO_{3-\delta}$ ($0.0 \leq x \leq 0.75$)", *Solid State Ionics* **177**, 1395–1403 (2006).

96. Duan, C. *et al.*, "Readily processed protonic ceramic fuel cells with high performance at low temperatures", *Science* **349**, 1321–1326 (2015).

97. Hakim, M., Yoo, C., Joo, J. H. & Yu, J. H., "Enhanced durability of a proton conducting oxide fuel cell with a purified yttrium-doped barium zirconate-cerate electrolyte", *J. Power Sources* **278**, 320–324 (2015).

98. Bae, K. et al., "Demonstrating the potential of yttrium-doped barium zirconate electrolyte for high-performance fuel cells", *Nat. Commun.* **8**, 1–9 (2017).

99. Tsur, Y., Dunbar, T. D. & Randall, C. A., "Crystal and Defect Chemistry of Rare Earth Cations in $BaTiO_3$", *J. Electroceramics* **7**, 25–34 (2001).

100. Jayaraman, V. *et al*., "Characterization of perovskite systems derived from $Ba_2In_2O_5\square$ – Part I: the oxygen-deficient $Ba_2In_{2(1-x)}Ti_{2x}O_{5+x}\square_{1-x}$ ($0 \le x \le 1$) compounds", *Solid State Ionics* **170**, 17–24 (2004).

101. Jayaraman, V. *et al*., "Characterization of perovskite systems derived from $Ba_2In_2O_5\square$ – Part II: The proton compounds $Ba_2In_{2(1-x)}Ti_{2x}O_{4+2x}(OH)_y$ [$0 \le x \le 1$; $y \le 2(1-x)$]", *Solid State Ionics* **170**, 25–32 (2004).

102. Quarez, E., Noirault, S., Caldes, M. T. & Joubert, O., "Water incorporation and proton conductivity in titanium substituted barium indate", *J. Power Sources* **195**, 1136–1141 (2010).

103. Rahman, S. M. H., Knee, C. S., Ahmed, I., Eriksson, S. G. & Haugsrud, R., "50 mol% indium substituted $BaTiO_3$: characterization of structure and conductivity", *Int. J. Hydrogen Energy* **37**, 7975–7982 (2012).

104. Speakman, S. A., Richardson, J. W., Mitchell, B. J. & Misture, S. T., "*In-situ* diffraction study of $Ba_2In_2O_5$", *Solid State Ionics* **149**, 247–259 (2002).

105. Hashimoto, T., Inagaki, Y., Kishi, A. & Dokiya, M., "Absorption and secession of H_2O and CO_2 on $Ba_2In_2O_5$ and their effects on crystal structure", *Solid State Ionics* **128**, 227–231 (2000).

106. Schober, T., Friedrich, J. & Krug, F., "Phase transition in the oxygen and proton conductor $Ba_2In_2O_5$ in humid atmospheres below 300 °C", *Solid State Ionics* **99**, 9–13 (1997).

107. Zhang, G. B. & Smyth, D. M., "Proton conduction in $Ba_2In_2O_5$", *Solid State Ionics* **82**, 153–160 (1995).

108. Norby, T. & Christiansen, N., "Proton conduction in Ca- and Sr-substituted $LaPO_4$", *Solid State Ionics* **77**, 240–243 (1995).

109. Ferrara, C., Mancini, A., Ritter, C., Malavasi, L. & Tealdi, C., "Interstitial oxide ion migration in scheelite-type electrolytes: a combined neutron diffraction and computational study", *J. Mater. Chem. A* **3**, 22258–22265 (2015).

110. Aleshin, E. & Roy, R., "Crystal Chemistry of Pyrochlore", *J. Am. Ceram. Soc.* **45**, 18–25 (1962).

111. Chang, L. L. Y. & Phillips, B., "Samarium and Lanthanum Tungstates of the $3R_2O_3{\cdot}WO_3$ Type", *Inorg. Chem.* **3**, 1792–1794 (1964).

112. Magrasó, A. *et al*. "Complete structural model for lanthanum tungstate: A chemically stable high temperature proton conductor by means of intrinsic defects", *J. Mater. Chem.* **22**, 1762–1764 (2012).

113. Nigara, Y., Yashiro, K., Kawada, T. & Mizusaki, J., "Hydrogen permeability in $(CeO_2)_{0.9}(GdO_{1.5})_{0.1}$ at high temperatures", *Solid State Ionics* **159**, 135–141 (2003).

114. Larring, Y. & Norby, T., "Protons in rare earth oxides", *Solid State Ionics* **77**, 147–151 (1995).

115. Subramanian, M. A., Aravamudan, G. & Subba Rao, G. V., "Oxide Pyrochlores - A Review", *Prog. Solid State Chem.* **15**, 55–143 (1983).

116. Omata, T. & Otsuka-Yao-Matsuo, S., "Electrical Properties of Proton-Conducting Ca-Doped $La_2Zr_2O_7$ with a Pyrochlore-Type Structure", *J. Electrochem. Soc.* **148**, E252-E261 (2001).

117. Kobayashi, Y. *et al*., "An oxyhydride of $BaTiO_3$ exhibiting hydride exchange and electronic conductivity", *Nat. Mater.* **11**, 507–511 (2012).

118. Tang, Y. *et al*., "On Hydride Diffusion in Transition Metal Perovskite Oxyhydrides Investigated via Deuterium Exchange", *Chem. Mater.* **29**, 8187–8194 (2017).

119. Verbraeken, M. C., Cheung, C., Suard, E. & Irvine, J. T. S., "High H^- ionic conductivity in barium hydride", *Nat. Mater.* **14**, 95–100 (2015).

120. Poulsen, F. W., "Speculations on the existence of hydride ions in proton conducting oxides", *Solid State Ionics* **145**, 387–397 (2001).

121. Poeppelmeier, K., "A Mixed Oxide-Hydride Perovskite", *Science* **295**, 1849 (2002).

122. Kobayashi, G. *et al*., "Pure H^- conduction in oxyhydrides", *Science* **351**, 1314–1317 (2016).

123. Torino, N. *et al*., "The influence of cation ordering, oxygen vacancy distribution and proton siting on observed properties in ceramic electrolytes: the case of scandium substituted barium titanate", *Dalt. Trans.* **46**, 8387–8398 (2017).

124. Torino, N. *et al*., "Insight into the dehydration behaviour of scandium-substituted barium titanate perovskites via simultaneous in situ neutron powder thermodiffractometry and thermogravimetric analysis", *Solid State Ionics* **324**, 233–240 (2018).

125. Pechini, M. P., "Method of preparing lead and alkaline earth titanates and niobates and coating method using the same to form a capacitor", US Patent no. US3330697 A (1967).

126. Hernandez, T. & Bautista, M. C., "The role of the synthesis route to obtain densified TiO_2-doped alumina ceramics", *J. Eur. Ceram. Soc.* **25**, 663–672 (2005).

127. Galceran, M., Pujol, M. C., Aguiló, M. & Díaz, F., "Sol-gel modified Pechini method for obtaining nanocrystalline $KRE(WO_4)_2$ (RE = Gd and Yb)", *J. Sol-Gel Sci. Technol.* **42**, 79–88 (2007).

128. Rietveld, H. M., "A profile refinement method for nuclear and magnetic structures", *J. Appl. Crystallogr.* **2**, 65–71 (1969).

129. *Experimental Methods in the Physical Sciences vol. 44 - Neutron Scattering – Fundamentals*, ed. Lucatorto, T., Parr, A. C., Baldwin, K., Elsevier Inc., 2013. ISBN: 978-0-12-398374-9

130. Playford, H. Y., Owen, L. R., Levin, I. & Tucker, M. G., "New Insights into Complex Materials Using Reverse Monte Carlo Modeling", *Annu. Rev. Mater. Res.* **44**, 429–449 (2014).

131. *Underneath the Bragg peaks*, Egami, T. & Billinge, S. J. L., Pergamon, 2012. ISBN: 9780080971414

132. Larson, A. C. & Von Dreele, R. B., "General Structure Analysis System (GSAS)", *Los Alamos National Laboratory*, Report LAUR 86–748 (2000).

133. Toby, B. H., "EXPGUI, a graphical user interface for GSAS", *J. Appl. Crystallogr.* **34**, 210–213 (2001).

134. Coelho, A., *Topas Academic Version 5*, Topas Academic, Coelho Software, Brisbane, 2012.

135. Le Bail, A., Duroy, H. & Fourquet, J. L., "Ab-initio structure determination of $LiSbWO_6$ by X-ray powder fiffraction", *Mater. Res. Bull.* **23**, 447–452 (1988).

136. Quarez, E., Noirault, S., Salle, A. L. G. La, Stevens, P. & Joubert, O., "Evaluation of $Ba_2(In_{0.8}Ti_{0.2})_2O_{5.2-n}(OH)_{2n}$ as a potential electrolyte material for proton-conducting solid oxide fuel cell", *J. Power Sources* **195**, 4923–4927 (2010).

137. Shannon, R. D., "Revised Effective Ionic Radii and Systematic Studies of Interatomic Distances in Halides and Chalcogenides", *Acta Crystallogr.* **A32**, 751–767 (1976).

138. Bjørheim, T. S., Rahman, S. M. H., Eriksson, S. G., Knee, C. S. & Haugsrud, R., "Hydration thermodynamics of the proton conducting oxygen-deficient perovskite series $BaTi_{1-x}M_xO_{3-x/2}$ with M = In or Sc", *Inorg. Chem.* **54**, 2858–2865 (2015).

139. Ahmed, I., Eriksson, S. G., Ahlberg, E. & Knee, C. S., "Influence of microstructure on electrical properties in $BaZr_{0.5}In_{0.5}O_{3-\delta}$ proton conductor", *Solid State Ionics* **179**, 1155–1160 (2008).

140. Ahmed, I. *et al*., "Proton Conduction in Perovskite Oxide $BaZr_{0.5}Yb_{0.5}O_{3-\delta}$ Prepared by Wet Chemical Synthesis Route", *J. Electrochem. Soc.* **155**, P97–P102 (2008).

141. Xin, C. R. *et al*., "Polymorphism and dielectric properties of Sc-doped $BaTiO_3$ nanopowders synthesized by sol-gel method", *Mater. Res. Bull.* **48**, 2220–2226 (2013).

142. Agafonov, V., Kahn, A. & Michel, D., "Crystal structure of $BaSc_2O_4$; its relation with perovskite", *Mater. Res. Bull.* **18**, 975–981 (1983).

143. Shima, D. & Haile, S. M., "The influence of cation non-stoichiometry on the properties of undoped and gadolinia-doped barium cerate", *Solid State Ionics* **97**, 443–455 (1997).

144. Ma, G., Shimura, T. & Iwahara, H., "Ionic conduction and nonstoichiometry in $Ba_xCa_{0.90}Y_{0.10}O_{3-\alpha}$", *Solid State Ionics* **110**, 103–110 (1998).

145. Snijkers, F. M. M., Buekenhoudt, A., Cooymans, J. & Luyten, J. J., "Proton conductivity and phase composition in $BaZr_{0.9}Y_{0.1}O_{3-\delta}$", *Scr. Mater.* **50**, 655–659 (2004).

146. Babilo, P., Uda, T. & Haile, S. M., "Processing of yttrium-doped barium zirconate for high proton conductivity", *J. Mater. Res.* **22**, 1322–1330 (2007).

147. Yamazaki, Y., Hernandez-Sanchez, R. & Haile, S. M., "High Total Proton Conductivity in Large-Grained Yttrium-Doped Barium Zirconate", *Chem. Mater.* **51**, 2755–2762 (2009).

148. Ahmed, I. *et al*., "Crystal Structure and Proton Conductivity of $BaZr_{0.9}Sc_{0.1}O_{3-\delta}$", *J. Am. Ceram. Soc.* **91**, 3039–3044 (2008).

149. Suyama, Y. & Kato, A., "Reactivity of ultrafine-TiO_2 (anatase) powders with $BaCO_3$", *Ceramurg. Int.* **1**, 5–9 (1975).

150. Schleid, T. & Meyer, G., "Single Crystals Of Rare Earth Oxides From Reducing Halide Melts", *J. Less-Common Met.* **149**, 73–80 (1989).

151. Lein, H. L., Wiik, K. & Grande, T., "Thermal and chemical expansion of mixed conducting $La_{0.1}Sr_{0.9}Co_{0.8}Fe_{0.2}O_{3-\delta}$", *Solid State Ionics* **177**, 1795–1798 (2006).

152. Norberg, S. T. *et al*., "Structural Disorder in Doped Zirconias, Part I: The $Zr_{0.8}$ $Sc_{0.2-x}Y_xO_{1.9}$ ($0.0 \le x \le 0.2$) System", *Chem. Mater.* **23**, 1356–1364 (2011).

153. Marrocchelli, D., Madden, P. A., Norberg, S. T. & Hull, S., "Structural disorder in doped zirconias, part II: Vacancy ordering effects and the conductivity maximum", *Chem. Mater.* **23**, 1365–1373 (2011).

154. Fabbri, E., Pergolesi, D. & Traversa, E., "Materials challenges toward proton-conducting oxide fuel cells: a critical review", *Chem. Soc. Rev.* **39**, 4355–4369 (2010).

155. Bohn, H. G. & Schober, T., "Electrical Conductivity of the High-Temperature Proton Conductor $BaZr_{0.9}Y_{0.1}O_{2.95}$", *J. Am. Ceram. Soc.* **83**, 768–772 (2000).

156. Shim, J. H., Gür, T. M. & Prinz, F. B., "Proton conduction in thin film yttrium-doped barium zirconate", *Appl. Phys. Lett.* **92**, 253115 (2008).

157. Pergolesi, D. *et al*., "High proton conduction in grain-boundary-free yttrium-doped barium zirconate films grown by pulsed laser deposition", *Nat. Mater.* **9**, 846–852 (2010).

158. Schober, T. & Bohn, H. G., "Water vapor solubility and electrochemical characterization of the high temperature proton conductor $BaZr_{0.9}Y_{0.1}O_{2.95}$", *Solid State Ionics* **127**, 351–360 (2000).

159. Nikodemski, S., Tong, J. & O'Hayre, R., "Solid-state reactive sintering mechanism for proton conducting ceramics", *Solid State Ionics* **253**, 201–210 (2013).

160. Kreuer, K. D. *et al*., "Proton conducting alkaline earth zirconates and titanates for high drain electrochemical applications", *Solid State Ionics* **145**, 295–306 (2001).

161. Imashuku, S. *et al*., "Dependence of Dopant Cations on Microstructure and Proton Conductivity of Barium Zirconate", *J. Electrochem. Soc.* **156**, B1–B8 (2009).

162. Kreuer, K. D., "On the development of proton conducting materials for technological applications", *Solid State Ionics* **97**, 1–15 (1997).

163. Giannici, F., Longo, A., Balerna, A., Kreuer, K.-D. & Martorana, A., "Indium Doping in Barium Cerate: the Relation between Local Symmetry and the Formation and Mobility of Protonic Defects", *Chem. Mater.* **19**, 5714–5720 (2007).

164. Jarry, A., Joubert, O., Suard, E., Zanotti, J.-M. & Quarez, E., "Location of Deuterium sites at operating temperature from neutron diffraction of $BaIn_{0.6}Ti_{0.2}Yb_{0.2}O_{2.6-n}(OH)_{2n}$, an electrolyte for Proton-Solid Oxide Fuel Cells", *Phys. Chem. Chem. Phys.* **18**, 15751-15759 (2016).

165. Nagasaki, T. *et al*., "Neutron powder diffraction and difference maximum entropy method analysis of protium- and deuterium-dissolved $BaSn_{0.5}In_{0.5}O_{2.75+\alpha}$", *J. Solid State Chem.* **182**, 2632–2639 (2009).

166. Kendrick, E., Knight, K. S., Islam, M. S. & Slater, P. R., "Structural studies of the proton conducting perovskite '$La_{0.6}Ba_{0.4}ScO_{2.8}$'", *Solid State Ionics* **178**, 943–949 (2007).

167. Ito, T. *et al*., "Location of deuterium atoms in $BaSn_{0.5}In_{0.5}O_{2.75+\alpha}$ by neutron powder diffraction at 10 K", *Solid State Ionics* **178**, 13–17 (2007).

168. Knight, K. S., "Powder neutron diffraction studies of $BaCe_{0.9}Y_{0.1}O_{2.95}$ and $BaCeO_3$ at 4.2 K: A possible structural site for the proton", *Solid State Ionics* **127**, 43–48 (2000).

169. Fabbri, E., Pergolesi, D., Licoccia, S. & Traversa, E., "Does the increase in Y-dopant concentration improve the proton conductivity of $BaZr_{1-x}Y_xO_{3-\delta}$ fuel cell electrolytes?", *Solid State Ionics* **181**, 1043–1051 (2010).

170. Kuz'min, A. V., Balakireva, V. B., Plaksin, S. V. & Gorelov, V. P., "Total and hole conductivity in the $BaZr_{1-x}Y_xO_{3-\alpha}$ system (x = 0.02-0.20) in oxidizing atmosphere", *Russ. J. Electrochem.* **45**, 1351–1357 (2009).

171. Han, D., Shinoda, K. & Uda, T., "Dopant site occupancy and chemical expansion in rare earth-doped barium Zirconate", *J. Am. Ceram. Soc.* **97**, 643–650 (2014).

172. Ahmed, I. *et al*., "Structural study and proton conductivity in Yb-doped $BaZrO_3$", *Solid State Ionics* **178**, 515–520 (2007).

173. Omata, T., Noguchi, Y. & Otsuka-Yao-Matsuo, S., "Infrared Study of High-Temperature Proton-Conducting Aliovalently Doped $SrZrO_3$ and $BaZrO_3$", *J. Electrochem. Soc.* **152**, E200–E205 (2005).

174. Shirpour, M. *et al*., "Dopant segregation and space charge effects in proton-conducting $BaZrO_3$ perovskites", *J. Phys. Chem. C* **116**, 2453–2461 (2012).

175. Wang, J. J., Meng, F. Y., Ma, X. Q., Xu, M. X. & Chen, L. Q., "Lattice, elastic, polarization, and electrostrictive properties of $BaTiO_3$ from first-principles", *J. Appl. Phys.* **108**, (2010).

176. *Ferrolectrics and Related Substances*, Hellwege, K. H. & Hellwege, A. M., Landolt-Börnstein, Vol. 3, Spriger-Verlag, Berlin, 1969. ISBN: 9783540098805

177. Park, I. J. & Han, Y. H., "Relaxation behavior of oxygen vacancies in Sc-doped $BaTiO_3$", *J. Korean Phys. Soc.* **66**, 1416–1421 (2015).

178. Giannici, F., Longo, A., Balerna, A., Kreuer, K. D. & Martorana, A., "Proton Dynamics in In:$BaZrO_3$: Insights on the atomic and electronic structure from X-ray absorption spectroscopy", *Chem. Mater.* **21**, 2641–2649 (2009).

179. Das, A., Xhafa, E. & Nikolla, E., "Electro- and thermal-catalysis by layered, first series Ruddlesden-Popper oxides", *Catal. Today* **277**, 214–226 (2016).

180. Wang, H., Gou, G. & Li, J., "Ruddlesden-Popper perovskite sulfides $A_3B_2S_7$: A new family of ferroelectric photovoltaic materials for the visible spectrum", *Nano Energy* **22**, 507–513 (2016).

181. Battle, P. D. *et al*., "Crystal and magnetic structures of the colossal magnetoresistance manganates $Sr_{2-x}Nd_{1+x}Mn_2O_7$ (x = 0.0, 0.1)", *Phys. Rev. B* **54**, 15967–15977 (1996).

182. Yan, Y. J. *et al*., "Electron-Doped Sr_2IrO_4: An Analogue of Hole-Doped Cuprate Superconductors Demonstrated by Scanning Tunneling Microscopy", *Phys. Rev. X* **5**, 041018 (2015).

183. Hu, L. L. *et al*., "Strong pseudospin-lattice coupling in $Sr_3Ir_2O_7$: Coherent phonon anomaly and negative thermal expansion", *Phys. Rev. B* **99**, 094307 (2019).

184. Tsipis, E. V & Kharton, V. V., "Electrode materials and reaction mechanisms in solid oxide fuel cells: a brief review. III. Recent trends and selected methodological aspects", *J. Solid State Electrochem.* **15**, 1007–1040 (2011).

185. Tsipis, E. V & Kharton, V. V., "Electrode materials and reaction mechanisms in solid oxide fuel cells: a brief review I. Performance-deteremining factors", *J. Solid State Electrochem.* **12**, 1039–1060 (2008).

186. Carter, S. *et al*., "Oxygen transport in selected nonstoichiometric perovskit-structure oxides", *Solid State Ionics* **53–56**, 597–605 (1992).

187. Minh, N. Q., "Ceramic Fuel Cells", *J. Am. Ceram. Soc.* **76**, 563–588 (1993).

188. Maguire, E., Gharbage, B., Marques, F. M. B. & Labrincha, J. A., "Cathode materials for intermediate temperature SOFCs", *Solid State Ionics* **127**, 329–335 (2000).

189. Matvejeff, M. *et al*., "New Water-Containing Phase Derived from the $Sr_3Fe_2O_{7-\delta}$ Phase of the Ruddlesden-Popper Structure", *Chem. Mater.* **17**, 2775–2779 (2005).

190. Lehtimäki, M., Hirasa, A., Matvejeff, M., Yamauchi, H. & Karppinen, M., "Water-containing derivative phases of the $Sr_{n+1}Fe_nO_{3n+1}$ series", *J. Solid State Chem.* **180**, 3247–3252 (2007).

191. Ishihara, T., Matsuda, H. & Takita, Y., "Doped $LaGaO_3$ Perovskite Type Oxide as a New Oxide Ionic Conductor", *J. Am. Chem. Soc.* **116**, 3801–3803 (1994).

192. Li, X., Shimada, H. & Ihara, M., "Conductivity of new electrolyte material $Pr_{1-x}M_{1+x}InO_4$ (M=Ba, Sr) with related perovskite structure for solid oxide fuel cells", *ECS Trans.* **50**, 3–14 (2013).

193. Oh-Ishi, K. & Syono, Y., "Dependence of lattice parameters and T_C on the hole concentration determined by precise measurement of the oxygen content of $M_xLa_{2-x}CuO_{4-y}$ (M = Ba, Sr, Ca)", *J. Solid State Chem.* **95**, 136–144 (1991).

194. Rial, C. *et al*., "Effects of extra oxygen on the structure and superconductivity of $La_{2-x}CuO_{4+y}$ prepared by chemical oxidation", *Physica C* **297**, 277–293 (1998).

195. Shi, C. Y., Hu, Z. B. & Hao, Y. M., "Structural, magnetic and dielectric properties of $La_{2-x}Ca_xNiO_{4+\delta}$ (x = 0, 0.1, 0.2, 0.3)", *J. Alloys Compd.* **509**, 1333–1337 (2011).

196. Kim, I. S., Kawaji, H., Itoh, M. & Nakamura, T., "Structural and dielectric studies on the new series of layered compounds, strontium lanthanum scandium oxides", *Mater. Res. Bull.* **27**, 1193–1203 (1992).

197. Patel, R., Simon, C. & Weller, M. T., "$LnSrScO_4$ (Ln = La, Ce, Pr, Nd and Sm) systems and structure correlations for A_2BO_4 (K_2NiF_4) structure types", *J. Solid State Chem.* **180**, 349–359 (2007).

198. Titov, Y. O. *et al.*, "Synthesis and determination of the crystal structure of layer scandates $SrLn_2Sc_2O_7$", *Dopovidi Natsional'noï Akad. Nauk Ukr.* **3**, 155–161 (2009).

199. TItov, Y. A. *et al.*, "Synthesis and crystal structure of $BaLn_2Sc_2O_7$", *Dopovidi Natsional'noï Akad. Nauk Ukr.* **5**, 172–178 (2009).

200. TItov, Y. A., Belyavina, N. M., Markiv, V. Y., Slobodyanik, M. S. & Krayevska, Y. A., "Synthesis and crystal structure of $BaLaInO_4$ and $SrLnInO_4$ (Ln = La, Pr)", *Dopovidi Natsional'noï Akad. Nauk Ukr.* **10**, 160–166 (2009).

201. Kato, S., Ogasawara, M., Sugai, M. & Nakata, S., "Synthesis and oxide ion conductivity of new layered perovskite $La_{1-x}Sr_{1+x}InO_{4-d}$", *Solid State Ionics* **149**, 53–57 (2002).

202. Caldes, M., Michel, C., Rouillon, T., Hervieu, M. & Raveau, B., "Novel indates $Ln_2BaIn_2O_7$, n = 2 members of the Ruddlesden-Popper family (Ln = La, Nd)", *J. Mater. Chem.* **12**, 473–476 (2002).

203. Titov, Y. A. *et al.*, "Synthesis and crystal structure of $BaLn_2In_2O_7$", *Dopovidi Natsional'noï Akad. Nauk Ukr.* **1**, 148–154 (2010).

204. Kim, I.-S., Nakamura, T. & Itoh, M., "Humidity Sensing Effects of the Layered Oxides $SrO(LaScO_3)_n$ (n = 1, 2, ∞)", *J. Ceram. Soc. Japan* **101**, 800–803 (1993).

205. Huang, Y.-H., Dass, R. I., Denyszyn, J. C. & Goodenough, J. B., "Synthesis and Characterization of $Sr_2MgMoO_{6-\delta}$ — An anode material for the Solid Oxide Fuel Cell", *J. Electrochem. Soc.* **153**, A1266 (2006).

206. Liang, K. C., Du, Y. & Nowick, A. S., "Fast high-temperature proton transport in nonstoichiometric mixed perovskites", *Solid State Ionics* **69**, 117–120 (1994).

207. Corcoran, D. J. D. & Irvine, J. T. S., "Investigations into $Sr_3CaZr_{0.5}Ta_{1.5}O_{8.75}$, a novel proton conducting perovskite oxide", *Solid State Ionics* **145**, 307–313 (2001).

208. Zhu, Z., Tao, Z., Bi, L. & Liu, W., "Investigation of $SmBaCuCoO_{5+\delta}$ double-perovskite as cathode for proton-conducting solid oxide fuel cells", *Mater. Res. Bull.* **45**, 1771–1774 (2010).

209. Mao, X., Yu, T. & Ma, G., "Performance of cobalt-free double-perovskite $NdBaFe_{2-x}Mn_xO_{5+\delta}$ cathode materials for proton-conducting IT-SOFC", *J. Alloys Compd.* **637**, 286–290 (2015).

210. Nowick, A. S., Du, Y. & Liang, K. C., "Some factors that determine proton conductivity in nonstoichiometric complex perovskites", *Solid State Ionics* **125**, 303–311 (1999).

211. Vasala, S. *et al.*, "Isovalent and aliovalent substitution effects on redox chemistry of $Sr_2MgMoO_{6-\delta}$ SOFC-anode material", *Solid State Ionics* **181**, 754–759 (2010).

212. Marrero-López, D. *et al.*, "Synthesis, phase stability and electrical conductivity of $Sr_2MgMoO_{6-\delta}$ anode", *Mater. Res. Bull.* **43**, 2441–2450 (2008).

213. Zakharchuk, K., Kravchenko, E., Fagg, D. P., Frade, J. R. & Yaremchenko, A. A., "Mixed ionic-electronic conductivity and thermochemical expansion of Ca and Mo co-substituted pyrochlore-type $Gd_2Ti_2O_7$" *RSC Adv.* **6**, 70186–70196 (2016).

214. Besse, J.-P., Wathle, M. & Baud, G., "Pérovskites lacunaires du type A_2MgMoO_{6-x}", *Comptes rendus Hebd. des séances l'Académie des Sci. Série C* **272**, 545–548 (1971).

215. Sher, F. *et al*., "Structural, magnetic and transport properties of $Sr_2Fe_{1-x}Mg_xMoO_6$ ($0 \leq x \leq 1$) double perovskites", *Solid State Sci.* **7**, 912–919 (2005).

216. Huang, Y.-H., Dass, R. I., Xing, Z.-L. & Goodenough, J. B., "Double Perovskites as Anode Materials for Solid-Oxide Fuel Cells", *Science* **312**, 254–257 (2006).

217. Bernuy-Lopez, C., Allix, M., Bridges, C. A., Claridge, J. B. & Rosseinsky, M. J., "$Sr_2MgMoO_{6-\delta}$: Structure, phase stability, and cation site order control of reduction", *Chem. Mater.* **19**, 1035–1043 (2007).

218. Battle, P. D., Goodenough, J. B. & Price, R., "The crystal structures and magnetic properties of Ba_2LaRuO_6 and Ca_2LaRuO_6", *J. Solid State Chem.* **46**, 234–244 (1983).

219. Bish, D. L. & Chipera, S. J., "Comparison of a solid-state Si detector to a conventional scintillation detector-monochromator system in X-ray powder diffraction analysis", *Powder Diffr.* **4**, 137–143 (1989).

220. Tarasova, N. & Animitsa, I., "Anionic doping (F^-, Cl^-) as the method for improving transport properties of proton-conducting perovskites based on $Ba_2CaNbO_{5.5}$", *Solid State Ionics* **317**, 21–25 (2018).

221. Shimura, T., Komori, M. & Iwahara, H., "Ionic conduction in pyrochlore-type oxides containing rare earth elements at high temperature", *Solid State Ionics* **86–88**, 685–689 (1996).

222. Eurenius, K. E. J., Ahlberg, E. & Knee, C. S., "Proton conductivity in $Sm_2Sn_2O_7$ pyrochlores", *Solid State Ionics* **181**, 1577–1585 (2010).

223. Eurenius, K. E. J., Ahlberg, E. & Knee, C. S., "Proton conductivity in $Ln_{1.96}Ca_{0.04}Sn_2O_{7-\delta}$ (Ln = La, Sm, Yb) pyrochlores as a function of the lanthanide size", *Solid State Ionics* **181**, 1258–1263 (2010).

224. Eurenius, K. E. J., Ahlberg, E. & Knee, C. S., "Role of B-site ion on proton conduction in acceptor-doped $Sm_2B_2O_{7-\delta}$ (B = Ti, Sn, Zr and Ce) pyrochlores and C-type compounds", *Dalt. Trans.* **40**, 3946–3954 (2011).

225. Eurenius, K. E. J., Ahlberg, E., Ahmed, I., Eriksson, S. G. & Knee, C. S., "Investigation of proton conductivity in $Sm_{1.92}Ca_{0.08}Ti_2O_{7-\delta}$ and $Sm_2Ti_{1.92}Y_{0.08}O_{7-\delta}$ pyrochlores", *Solid State Ionics* **181**, 148–153 (2010).

226. Kramer, S. A., Spears, M. & Tuller, H. L., "Conduction in titanate pyrochlores: role of dopants", *Solid State Ionics* **72**, 59–66 (1994).

227. Matteucci, F., Cruciani, G., Dondi, M., Baldi, G. & Barzanti, A., "Crystal structural and optical properties of Cr-doped $Y_2Ti_2O_7$ and $Y_2Sn_2O_7$ pyrochlores", *Acta Mater.* **55**, 2229–2238 (2007).

228. Knop, O., Brisse, F. & Castelliz, L., "Pyrochlores. V. Thermoanalytic, X-ray, neutron, infrared, and dielectric studies of $A_2Ti_2O_7$ titanates", *Can. J. Chem.* **47**, 971–990 (1969).

229. Shlyakhtina, A. V., Abrantes, J. C. C., Larina, L. L. & Shcherbakova, L. G., "Synthesis and conductivity of $Yb_2Ti_2O_7$ nanoceramics", *Solid State Ionics* **176**, 1653–1656 (2005).

230. Reimers, J. N., Greedan, J. E. & Sato, M., "The Crystal Structure of the Spin-Glass Pyrochlore, $Y_2Mo_2O_7$", *J. Solid State Chem.* **72**, 390–394 (1988).

231. Mirebeau, I. *et al.*, "Pressure-induced ferromagnet to spin-glass transition in $Gd_2Mo_2O_7$", *Phys. Rev. B* **74**, 174414 (2006).

232. Bazuev, G. V., Zubkov, V. G. & G.P., S., "An X-ray and Neutron Diffraction Study of Solid Solutions $Ln_2(V_{1-x}Mo_x)_2O_7$ with the Pyrochlore Structure", *Russ. J. Inorg. Chem. (Eng. Transl.)* **32**, 1377 (1987).

233. Sleight, A. W., "New Ternary Oxides of Mercury with the Pyrochlore Structure", *Inorg. Chem.* **7**, 1704–1708 (1968).

234. Kramer, S. A. & Tuller, H. L., "A novel titanate-based oxygen ion conductor: $Gd_2Ti_2O_7$", *Solid State Ionics* **82**, 15–23 (1995).

235. Kim, N. & Grey, C. P., "Solid-state NMR study of the anionic conductor Ca-doped $Y_2Ti_2O_7$", *Dalt. Trans.* 3048–3052 (2004).

236. *Handbook of X-ray photoelectron spectroscopy: a reference book of standard spectra for identification and interpretation of XPS data*, Moulder, J. F., Stickle, W. F., Sobol, P. E. & Bomben, K. D., ed. Chastain, J., Physical Electronics Division, Perkin-Elmer Corporation, Eden Prairie, Minnesota (USA), 1992.

237. Choi, J. G. & Thompson, L. T., "XPS study of as-prepared and reduced molybdenum oxides", *Appl. Surf. Sci.* **93**, 143–149 (1996).

238. Whittle, K. R., Cranswick, L. M. D., Redfern, S. a. T., Swainson, I. P. & Lumpkin, G. R., "Lanthanum pyrochlores and the effect of yttrium addition in the systems $La_{2-x}Y_xZr_2O_7$ and $La_{2-x}Y_xHf_2O_7$", *J. Solid State Chem.* **182**, 442–450 (2009).